Modeling and optimization of energy system components equipped with phase change materials

zur Erlangung des akademischen Grades

DOKTOR DER INGENIEURWISSENSCHAFTEN (Dr.-Ing.) der

Fakultät für Maschinenbau

der Universität Paderborn

genehmigte

DISSERTATION

von

Matti Grabo, M.Sc.

aus Lutherstadt Wittenberg

Tag des Kolloquiums:	22.01.2025
Referent:	Prof. Dr.-Ing. habil. Eugeny Kenig
Korreferent:	Prof. Dr.-Ing. Henning Meschede

Acknowledgement

The content of this dissertation is based on the results of my research at the Fluid Process Engineering group at Paderborn University from 2017 to 2024. I would like to express my sincere gratitude to everyone who has accompanied me on this journey and contributed in various ways to the successful completion of this thesis.

First and foremost, I am deeply grateful to my doctoral supervisor, Prof. Eugeny Kenig, for his invaluable support. Through his guidance and by striving to internalize his approach to scientific research, I was able to acquire the skills and knowledge necessary to achieve the results presented in the following chapters.

I would like to thank my second supervisor, Prof. Henning Meschede, for reviewing my thesis and for accepting me as a postdoc at the Competence Center for Sustainable Energy Technology. I would also like to thank Prof. Iris Gräßler and Prof. Julia Riese for their participation as members on the examination board.

A big “thank you” to all my colleagues at the Fluid Process Engineering group, with whom I had the pleasure of working over the past eight years. Special mention goes to my office mates throughout this time, Andreas Schulz, Emre Acar, Alexander Salten and Bilal Hafeez, who were always up for a chat or a coffee. I would also like to thank our secretary, Astrid Bongard, for her support with all the bureaucratic matters that can arise in everyday university life.

Additionally, I would like to acknowledge my project partners and colleagues outside of the Fluid Process Engineering group, Andreas Paul and Daniel Weber, for their collaboration on the first case study involving PCM-integrated PV modules. I would also like to thank Gerrit Sonnenrein for valuable exchanges on all things PCM and Patrick Richter for granting me excess to his experimental data, which was invaluable in the second case study on packed bed latent heat storages.

Research cannot thrive without financial support, so I would like to express my appreciation to the German Federal Ministry for Economic Affairs and Climate and the Project Management Jülich for funding the two projects that form the foundation of this thesis. In this context, I would also like to extend my thanks to Felix Klinker and Helmut

Weinläder from the Center for Applied Energy Research e.V. for their excellent project management.

My parents have supported me and my education throughout my whole life – without their encouragement, I would not have been able to pursue this doctorate. I am deeply grateful to them. I would also like to thank my friends for the occasional distraction needed to keep me sane and engaged during the research and the writing process. Speaking of distractions, I should also mention our two cats, Wilma and Mogli, who often reminded me that it is time to feed them, which also meant it was probably time for me to take a short break from writing.

Finally, my deepest gratitude goes to my wife Kirby, who left her home country and moved to Bielefeld to be with me, and who has supported me through all the ups and downs of my doctoral studies. I am so very grateful for everything you have done for me.

Matti Grabo

Paderborn, March 5th 2025

Abstract

This thesis explores the modeling and optimization of energy system components incorporating phase change materials (PCM) through two different case studies. PCM are materials whose phase change characteristics during melting and solidification are utilized for heating and cooling purposes.

The theoretical foundations of heat transfer problems involving phase change, along with the relevant numerical solution methods, are discussed. A phase change model is presented, which was validated against analytical solutions and applied in the case studies.

For both case studies, a review of the state of the art is provided, followed by the formulation of specific research problems. The first case study investigated PCM-enhanced photovoltaic modules, while the second focused on packed bed latent heat storages (PBLHS) utilizing non-spherical PCM capsules. Thermal models were developed for both systems and validated with good accuracy against experimental data. These models were employed in parameter studies to identify optimized system configurations.

The presented results demonstrate that a PCM heat sink with sufficient thickness and thermal conductivity can significantly improve the efficiency and lifespan of photovoltaic modules. Furthermore, PCM capsules with both high packing density and surface area increase the volume-specific storage capacity and thermal power output of PBLHS.

Kurzfassung

Diese Arbeit behandelt die Modellierung und Optimierung von mit Phasenwechselmaterialien (PCM) ausgestatteten, energietechnischen Komponenten anhand zweier Fallstudien. PCM sind Materialien, deren Phasenwechseleigenschaften während des Schmelzens und Erstarrens für Heiz- und Kühlzwecke genutzt werden.

Zunächst werden die theoretischen Grundlagen zu Wärmeübertragungsproblemen mit Phasenwechsel erörtert und entsprechende numerische Lösungsmethoden diskutiert. Ein Modell für Phasenwechselvorgänge wird vorgestellt, welches anhand analytischer Lösungen validiert wurde und in den Fallstudien zum Einsatz kam.

Für beide Fallstudien wird der Stand der Technik erörtert und die entsprechenden Forschungsfragen werden formuliert. Die erste Fallstudie behandelt PCM-integrierte Photovoltaikmodule und die zweite Festbett-Latentwärmespeicher, welche nicht-kugelförmiger PCM-Kapseln verwenden. Für beide Systeme wurden thermische Modelle entwickelt und anhand experimenteller Daten mit guter Genauigkeit validiert. Diese Modelle wurden in Parameterstudien eingesetzt, um optimierte Systemkonfigurationen zu identifizieren.

Die vorgestellten Ergebnisse zeigen, dass ein PCM-Kühlkörper mit ausreichender Dicke und Wärmeleitfähigkeit den Wirkungsgrad und die Lebensdauer von Photovoltaikmodulen erheblich erhöht. Darüber hinaus verbessern PCM-Kapseln mit hoher Packungsdichte und Oberfläche sowohl die volumenspezifische Speicherkapazität als auch die thermische Leistung von Festbett-Latentwärmespeichern.

List of publications

Some of the contents presented in this thesis have been previously published in journal articles and conference proceedings, as listed below:

Journal articles

M. Grabo, E. Acar, E.Y. Kenig, Modeling and improvement of a packed bed latent heat storage filled with non-spherical encapsulated PCM-elements, Renewable Energy 173 (2021) 1087–1097. doi:10.1016/j.renene.2021.04.022

M. Grabo, C. Staggenborg, K.A. Philippi, E.Y. Kenig, Modeling and optimization of rectangular latent heat storage elements in an air-guided heat storage system, Front. Energy Res. 8 (2020) 571787. doi:10.3389/fenrg.2020.571787

M. Grabo, D. Weber, A. Paul, T. Klaus, W. Bermpohl, S. Krauter, E.Y. Kenig, Numerical investigation of the temperature distribution in PCM-integrated solar modules, Chemical Engineering Transactions 76 (2019) 895–900. doi:10.3303/CET1976150

Conference proceedings

M. Grabo, L. Kuckuck, E.Y. Kenig, Optimization of packed bed latent heat storages filled with PCM-capsules based on super-ellipsoids, in: M. Ban et al. (Eds.), Digital Proceedings of the 16th Conference on Sustainable Development of Energy, Water and Environment Systems (SDEWES), Faculty of Mechanical Engineering and Naval Architecture, Zagreb, Croatia, 2021, 0244-1-0244-18.

M. Grabo, E. Acar, E.Y. Kenig, Modeling of a latent heat storage system consisting of encapsulated PCM-elements, in: M. Ban et al. (Eds.), Digital Proceedings of the 15th Conference on Sustainable Development of Energy, Water and Environment Systems (SDEWES), Faculty of Mechanical Engineering and Naval Architecture, Zagreb, Croatia, 2020, 0045-1-0045-14.

M. Grabo, D. Weber, A. Paul, T. Klaus, W. Bermpohl, S. Krauter, E.Y. Kenig, Entwicklung eines thermischen 1D-Simulationsmodells zur Bestimmung der Temperaturverteilung in Solarmodulen, in: V. Wesselak (Ed.), RET.Con 2019: Tagungsband: 2.

Regenerative Energietechnik-Konferenz in Nordhausen, Hochschule Nordhausen, Nordhausen, Germany, 2019, 116–129. doi:10.22032/dbt.46054

D. Weber, M.I. Rafsan Jani, M. Grabo, O. Wallscheid, T. Klaus, S. Krauter, J. Böcker, Lifetime extension of photovoltaic modules by influencing the module temperature using phase change material, in: 2018 IEEE 7th World Conference on Photovoltaic Energy Conversion (WCPEC) (A Joint Conference of 45th IEEE PVSC, 28th PVSEC & 34th EU PVSEC), IEEE, 2018, 784–789. doi:10.1109/PVSC.2018.8548115

Oral presentations

M. Grabo, L. Kuckuck, E.Y. Kenig, Optimization of packed bed latent heat storages filled with PCM-capsules based on super-ellipsoids, 16th Conference on Sustainable Development of Energy, Water and Environment Systems (SDEWES), 10-15 October, Dubrovnik, Croatia, 2021.

M. Grabo, Forschen für ein nachhaltiges Bauen: Vorstellung des Projektes „RENBuild“, 4. Forum Bielefelder EnergieWerte2020, 08 December, Bielefeld, Germany, 2020.

M. Grabo, E. Acar, E.Y. Kenig, Modeling of a latent heat storage system consisting of encapsulated PCM-elements, 15th Conference on Sustainable Development of Energy, Water and Environment Systems (SDEWES), 01-04 September, Cologne, Germany, 2020.

M. Grabo, C. Staggenborg, E.Y. Kenig, Modellierung und Optimierung makroverkapselter Latentwärmespeicherelemente für ein luftgeführtes Wärmespeichersystem, Jahrestreffen der ProcessNet-Fachgruppe Energieverfahrenstechnik, 04-05 March, Frankfurt am Main, Germany, 2020.

M. Grabo, D. Weber, A. Paul, T. Klaus, W. Bermpohl, S. Krauter, E.Y. Kenig, Numerical investigation of the temperature distribution in PCM-integrated solar modules, 22nd Conference on Process Integration, Modelling and Optimisation for Energy Saving and Pollution Reduction (PRES‘19), 20-23 October, Agios Nicolaos, Greece, 2019.

M. Grabo, C. Staggenborg, E.Y. Kenig, Modellierung und Optimierung von makroverkapselten Latentwärmespeicherelementen, Wärmeübertragung mit Phasenwechsel in fluiden Systemen: Ein Update, 19-20 September, Paderborn, Germany, 2019.

M. Grabo, D. Weber, A. Paul, T. Klaus, W. Bermpohl, S. Krauter, E.Y. Kenig, Entwicklung eines thermischen 1D-Simulationsmodells zur Bestimmung der Temperaturverteilung in Solarmodulen, 2. Regenerative Energietechnik-Konferenz in Nordhausen (RET.Con 2019), 07-08 Februar, Nordhausen, Germany, 2019.

Posters

M. Grabo, E.Y. Kenig, Modellierung eines Latentwärmespeichersystems in Form einer ungeordneten Schüttung makro-verkapselter PCM-Elemente, Jahrestreffen der ProcessNet-Fachgruppen Fluidverfahrenstechnik und Wärme- und Stoffübertragung, 24-26 Feb, Leipzig, Germany, 2021.

M. Grabo, C. Staggenborg, E.Y. Kenig, Modellierung und Optimierung von makroverkapselten Latentwärmespeicherelementen, Wärmeübertragung mit Phasenwechsel in fluiden Systemen: Ein Update, 19-20 Sep, Paderborn, Germany, 2019.

M. Grabo, D. Weber, A. Paul, T. Klaus, W. Bermpohl, E.Y. Kenig, Numerische Untersuchung der Temperaturverteilung in PCM-integrierten Solarmodulen, Jahrestreffen der ProcessNet-Fachgruppe Energieverfahrenstechnik und des Arbeitsausschusses Thermische Energiespeicherung, 06-07 Mar, Frankfurt am Main, Germany, 2019.

Contents

List of figures

List of tables

Nomenclature

Latin symbols

Symbol	Description	Unit
A	Area	m²
a	Thermal diffusivity	m²/s
	Discretization coefficient	J/(m³K)
	Specific surface area	m²/m³
	Semi-axis length of superellipsoid	m
b	Discretization coefficient	J/(m³K)
	Semi axis length of superellipsoid	m
c	Specific heat capacity	J/(kgK)
	Volumetric heat capacity	J/(m³K)
	Semi-axis length of superellipsoid	m
CFL	Courant-Friedrichs-Lewy number	-
D	Characteristic length	m
	Damage	-
	Diameter	m
$\vec{d}$	Column vector	J/m³
E	Solar irradiance	W/m²
	Energy	J
e	Shape factor for superellipsoids	-
F	View factor	-
f	Correction factor, shape factor	-
Fo	(Numerical) Fourier number	-

g	Gravitational acceleration	m^2/s
Gr	Grashof number	-
H	Volumetric enthalpy Height	J/m^3 m
h	Heat transfer coefficient	$W/(m^2K)$
i	Counting variable	-
j	Time step	-
k	Thermal conductivity Boltzmann constant Coffin-Manson factor	W/(mK) J/K $s^{1/3}K^2$
L	Latent heat	J/kg
l	Length	m
$\boldsymbol{M}$	Coefficient matrix	$J/(m^3K)$
ME	Maximum error	K, W
MAE	Mean absolute error	K, m, W
N	Number of nodes Number of cycles till failure	- -
n	Spatial node Number of temperature cycles Shape factor for superellipsoids	- - -
Nu	Nusselt number	-
P	Power	W
p	Number of value pairs	-
Pr	Prandtl number	-
Q	Energy, heat	J
$\dot{Q}$	Heat flow rate	W
q	Specific heat	J/kg
$\dot{q}$	Heat flux	W/m^2
R	Radius	m
r	Spatial coordinate in spherical coordinate system	m
Ra	Rayleigh number	-

Re	Reynolds number	-
Ri	Richardson number	-
RME	Relative maximum error	%
$RMAE$	Relative mean absolute error	%
$RMSE$	Root mean square error	W, K
$RRMSE$	Relative root mean square error	%
S	Source term	W/m³
s	Thickness Location of solid-liquid interface Wall distance	m m m
St	Stefan number	-
T	Temperature	°C, K
t	Time Duration	s s
u	Velocity	m/s
V	Volume	m³
v	Surface parameter of superellipsoids	-
W	Width	m
w	Surface parameter of superellipsoids	-
X	Length of domain	m
x, y, z	Spatial coordinates in Cartesian coordinate system	m
$Y, \hat{Y}$	Predicted and actual value in error analysis	K, m, W

Greek symbols

Symbol	**Description**	**Unit**
α	Absorptivity Factor in approximate solution for Stefan problems	- -
B	Beta function	-
β	Coefficient of thermal expansion Aspect ratio	1/K -

γ	Liquid fraction	-
	Angle	°
	Aspect ratio	-
δ	Reflectance	-
ε	Emissivity	-
	Packing density	-
ζ	Generic spatial coordinate	m
η	Efficiency	-
λ	Mixture conductivity	W/(mK)
	Constant in Neumann solution	-
ν	Kinematic viscosity	m^2/s
	Ratio of thermal diffusivities	-
ρ	Density	kg/m^3
σ	Stefan-Boltzmann constant	$W/(m^2K^4)$
τ	Transmittance	-
ϕ	Porosity	-
Ψ	Correction	-
ω	Relaxation factor	-

Subscripts

Symbol	Description
0	Initial
a	Activation
ab	Absorbing
av	Average
acc	Accumulated
amb	Ambient
app	Apparent
B	Boltzmann
bot	Bottom side
bub	Bubble wrap foil

C	Capsule
c	Convective, cycle
CM	Coffin-Manson
ch	Characteristic
cr	Critical
el	Electrical
em	Emitting
exp	Experimental
$EVA1$	EVA1 layer in PV module
f	Fluid, fusion, free, failure
fc	Forced convection
G	Glass layer in PV modules
GB	Ground - bottom
GT	Ground - top
gro	Ground
HTF	Heat transfer fluid
I	Inclination
Int	Interface
l	Liquid
ls	Left side
lam	Laminar
lee	Leeward
luv	Windward
$lower$	Lower temperature sensor
max	Maximum
$melt$	Melting
N	Total number of spatial nodes
n	Spatial index

nb	Neighboring
nc	Natural convection
num	Numerical
P	Power
p	Isobaric
PB	Packed bed
PV	Photovoltaic
PCM	Phase change material
PVM	Photovoltaic module
r	Radiative, radius
rs	Right side
ref	Reference
S	Superellipsoid
s	Solid, interface
SB	Sky - bottom
SC	Solar cell
ST	Sky - top
sim	Simulation
sky	Sky
smo	Smooth foil
sph	Sphere
T	Temperature, tank
t	Total
top	Top side
$turb$	Turbulent
$upper$	Upper temperature sensor
v	Void
vol	Volumetric

w	Wall

Superscripts

Symbol	Description
j	Time step index
m	Iteration index
old	Old time step
$+$	Dimensionless
$*$	Normalized, modified

Abbreviations

Abbreviation	Description
CAD	Computer aided design
CFD	Computational fluid dynamics
CO_2	Carbon dioxide
DEM	Discrete element method
FDM	Finite difference method
HDPE	High-density polyethylene
HTF	Heat transfer fluid
PBLHS	Packed bed latent heat storage
PCM	Phase change material
PP	Polypropylene
PV	Photovoltaics
RFCA	Rainflow-counting algorithm
STC	Standard test conditions (for PV module testing)
STL	Stereolithography
SVR	Surface-area-to-volume ratio
TES	Thermal energy storage
TRL	Technology readiness level

1 Introduction

This doctoral thesis is based on the results of two publicly funded research projects that both involved the use of phase change materials (PCM) in energy system components. The term "phase change material" refers to pure substances or mixtures with phase change characteristics, that are utilized for thermal processes (heating or cooling). Usually, PCM are associated with the transition from solid to liquid and vice versa. The first of the aforementioned research projects focused on using PCM to enhance the performance of photovoltaic (PV) modules, which formed the basis for the first case study presented in this thesis. The second project aimed at improving packed bed latent heat storages (PBLHS) by optimizing macroencapsulated PCM objects. The details and findings of this project are presented as the second case study.

1.1 Motivation

According to the European Environment Agency, renewable energy sources covered only 23 % of the energy demand in the European Union (EU) in the year 2022. Given that the EU has set a binding target to reach a share of 42.5 % renewable energy consumption by 2030 [1], further efforts in research and development are needed to create new and improve existing renewable energy generation technologies. Since the nature of the two largest renewable energy sources – solar and wind – is volatile, efficient storage technologies are required to cover periods of time when these sources are not available in order to establish them as a more attractive alternative to conventional, fossil-based energy sources. The two research projects mentioned above aimed at the improvement of an existing generation technology – solar PV – and the further establishment of renewable energy generation through thermal storages, both via the use of PCM. In the first project, PCM was utilized as a heat sink to stabilize the operating temperature of PV modules, increasing their efficiency and lifetime. In the second project, PCM was used to increase the storage density of conventional sensible liquid heat storages through the addition of PCM-filled capsules.

PCM are well suited for heating and cooling purposes due to their ability to store and release large amounts of energy within a certain temperature interval. Within this interval,

the energy that can be accessed is far greater than that of purely sensible heat storages, which makes PCM attractive for applications where energy density is of importance. Such applications include, for example, the cooling of electrical components such as PV modules through PCM heat sinks, thermally active clothes, building materials such as plaster, and thermal storages like PBLHS.

The design, optimization and operation of technical systems depend on the accurate prediction of the system behavior, which can be achieved using proper models. The main aspect that was affected by the integration of PCM in the two systems investigated in the aforementioned research projects was their thermal behavior. The driving mechanisms that determine the thermal behavior in general – thermal conduction, convection and radiation – are, in general, well understood and appropriate mathematical descriptions exist for a variety of problems. However, the integration of PCM introduces an additional element – the phase transition from solid to liquid and vice versa – which makes the modeling challenging due to complex heat transfer and fluid dynamics.

In both research projects, the goal was to develop a modeling approach that describes the thermal behavior of energy system components equipped with PCM in order to accelerate the uptake of renewable energy generation technologies. The proper capturing of the phase change process itself was one of the main aspects, around which the mathematical models of the respective investigated systems were built. These models were then implemented as numerical algorithms in MATLAB R2021b and used to simulate the thermal behavior of the systems. The simulation results were validated against experimental data and used for sensitivity analyses aiming at optimizing the system design.

1.2 Structure of the thesis

This thesis is structured into six chapters. Each chapter following this introduction starts with a short overview of its contents and ends with a summary of the most important findings.

The theoretical background of the heat transfer mechanisms relevant to this work is presented in Chapter 2. Specifically, thermal conduction, radiation and convection are discussed and the general advection-conduction equation for heat transfer along with the relevant boundary conditions are given. Next, an overview of phase change materials and common encapsulation technologies is presented. Thereafter, heat transfer problems that involve melting and solidification are discussed. The class of such problems, also referred to as Stefan problems, is described and the analytical solution proposed by Neumann is given. Also, approximate analytical solutions for spherical geometries are provided. Further, an overview of numerical techniques that are commonly used to solve solid-liquid phase change problems is given. Finite difference methods are discussed, followed by fixed grid approaches that were specifically developed for melting and solidification problems.

In Chapter 3, a phase change model along with a corresponding solution algorithm that was applied in the two case studies is introduced. The algorithm was tested and validated against the analytical solutions discussed in Chapter 2.

The next two chapters describe the case studies, following a similar structure: first, the state of the art is given, and the scope of the case study is defined. It follows a description of the system considered, along with the corresponding experimental setup used to obtain data for the validation of the simulation results. These simulation results were generated by applying the corresponding model presented in the subsequent section. Next, the validation procedure is detailed, and the accuracy of the model is demonstrated. Thereafter follows the description of parameter studies and geometry optimizations performed using the validated models. Each case study closes with a summary of the key findings and an evaluation of whether the respective research goals were achieved.

The thesis concludes with a summary of the case studies and a brief outlook.

2 Theoretical background

In this chapter, the theoretical background of heat transfer for the case studies presented in Chapters 4 and 5 is provided. First, the basic heat transfer mechanisms – heat conduction, radiation and convection – are discussed followed by the general heat transport equations for incompressible media and packed beds. An overview of boundary conditions relevant for heat transfer problems is given as well.

Next, technical phase change materials and encapsulation technologies are reviewed.

In the following section, the focus is laid on heat transfer problems involving phase change from solid to liquid and vice versa. A mathematical problem including moving boundaries, the so-called Stefan problem, is described and solutions proposed by Neumann are given. Additionally, approximate analytical solutions for spherical geometries are provided.

In the last section, numerical solution approaches to Stefan type heat transfer problems are addressed. The discretization through finite differences is discussed and fixed grid methods specifically developed for melting and solidification problems are presented.

2.1 Basic heat transfer mechanisms

Heat is a form of energy that crosses the boundary of a system due to a temperature difference between the system and its surroundings [2]. Temperature reflects the thermal state of a system and serves as a measure of molecular motion. According to the second law of thermodynamics, heat flows from regions of higher temperature to regions of lower temperature.

Heat is transported by two mechanisms: heat conduction and thermal radiation [3]. Heat conduction is the transfer of thermal energy through molecular motion due to a temperature difference. Thermal radiation describes the heat transfer by electromagnetic waves. Often, thermal convection is considered to be an individual mode of heat transfer, although it is a combination of heat conduction and advective energy transport caused by a moving fluid.

2.1.1 Heat conduction

The area specific heat transfer rate resulting from thermal conduction, referred to as heat flux $\dot{q}$, is defined by Fourier's law as:

$$\dot{q} = -k\nabla T \tag{2.1}$$

The thermal conductivity k is a material property, while T is the temperature. The negative sign in Eq. (2.1) accounts for the second law of thermodynamics. Conduction as the sole heat transport mechanism is only encountered in solids. In gases and liquids, heat conduction usually occurs together with thermal convection.

2.1.2 Thermal radiation

All objects with temperatures above absolute zero emit thermal radiation due to the movement of their constituting atoms and molecules. Thermal radiation can be reflected at the surface of an object, it can be transmitted through a transparent material, and it can be absorbed. When radiation is absorbed, energy is directly converted into heat. The maximum heat flux by a radiating surface $\dot{q}_r$ is governed by the Stefan-Boltzmann law:

$$\dot{q}_r = \sigma T^4 \tag{2.2}$$

Here, σ denotes the Stefan-Boltzmann constant. Eq. (2.2) was formulated by Boltzmann assuming radiation by a black body – an object which is both an ideal absorber and an ideal emitter of thermal radiation. Since ideal emitters do not exist in nature, a correction factor, the emissivity ε, is applied:

$$\dot{q}_r = \varepsilon\sigma T^4 \tag{2.3}$$

The emissivity depends on the material, the structure of the emitting surface and the temperature of the emitting object. On the other hand, the absorptivity α, transmittance τ and reflectivity δ are the fractions of the incoming radiation being absorbed, transmitted and reflected by an object that receives thermal radiation:

$$\alpha + \tau + \delta = 1 \tag{2.4}$$

To more accurately describe the heat radiation from real objects, the concept of a gray body was introduced. The absorptivity of a gray body does not depend on the characteristics of the incoming radiation (e.g., its wavelength) but is equal to its emissivity, $\alpha = \varepsilon$ [4]. Almost all objects are treated as gray bodies in technical calculations involving radiative heat transfer.

For the design of energy equipment, the radiative heat exchange between two or more bodies is of interest. As an example, a gray body can be considered, which is surrounded by a black body environment, as shown in Figure 2-1. Since all objects emit radiation, not only the hotter one transmits energy to the cooler one but also vice versa. Therefore, the net radiative heat flow $\dot{Q}_r$ across the surface of the gray object is given by:

$$\dot{Q}_r = \dot{Q}_{em} - \dot{Q}_{ab} = \varepsilon A \sigma T_{em}^4 - \alpha A \sigma T_{ab}^4 \tag{2.5}$$

with $\dot{Q}_{em}$ and $\dot{Q}_{ab}$ as emitted and absorbed heat flows from the object surface, which has a surface area A. As mentioned above, the emissivity of a gray body is equal to its absorptivity, i.e., $\alpha = \varepsilon$. Therefore, Eq. (2.5) becomes:

$$\dot{Q}_r = \varepsilon A \sigma (T_{em}^4 - T_{ab}^4) \tag{2.6}$$

If Eq. (2.6) is applied to, for example, a PV module that is thermally insulated on its back side and facing toward the sky, T_{em} would be the module temperature at its front surface and T_{ab} would be the temperature of the sky.

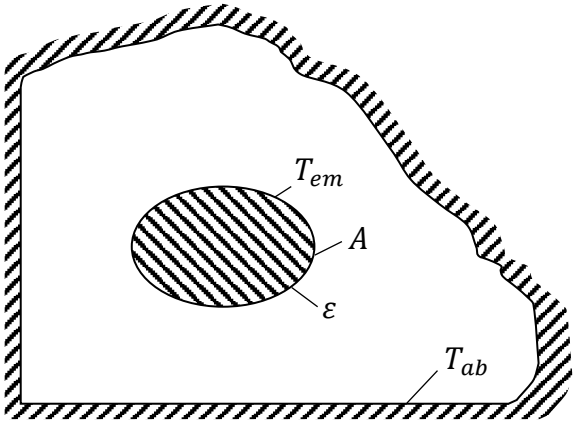

Figure 2-1: Radiative heat exchange of a gray body with a temperature T_{em} and its black environment with a temperature T_{ab}

2.1.3 Convective heat transfer

Convective heat transfer involves the combined mechanisms of advection and thermal conduction [3]. Advection refers to the transport of energy or other quantities (e.g., mass or momentum) through the bulk motion of a fluid.

Convective heat transport can be categorized by the cause of the fluid motion. In case the motion is driven by a pump or a fan, i.e., an externally generated pressure gradient, the type of convection is referred to as forced convection. In case the fluid motion is caused by a temperature difference and a resulting change in density, the process is called free or natural convection. Both mechanisms may also occur at the same time. This case is referred to as combined or mixed convection.

In technical applications, the heat exchange between a fixed wall and a moving fluid is often of interest. For such a case, Newton's law of cooling can be applied. It states that the convective heat transfer rate $\dot{Q}_c$ across a boundary is proportional to the temperature difference between a fixed wall and a moving fluid:

$$\dot{Q}_c = hA\left(T_w - T_f\right) \tag{2.7}$$

The proportionality constant h is the heat transfer coefficient and is a subject of numerous investigations as it depends on various factors, such as flow velocity, material properties,

geometric features, etc. For this reason, it is a case-specific value and has to be determined by experiments or numerical simulations, which can be quite challenging and resource consuming. Therefore, correlations are often used to determine h for reoccurring heat transfer problems, as, e.g., a hot fluid entering an externally cooled pipe. To ensure the similarity between different heat transfer problems and the validity of the correlations used, dimensionless numbers were introduced. For convective heat transfer problems, the Nusselt number Nu is often used, which describes the ratio of convective and conductive heat transfer:

$$Nu = \frac{hD_{ch}}{k} \tag{2.8}$$

Here, thermal conductivity is that of the fluid, while the parameter D_{ch} is a length that is characteristic for the specific heat transfer problem. For example, in case of a fluid flowing through a pipe, D_{ch} is the pipe diameter. Nu-correlations were developed by various authors and can be found for different applications in, e.g., [4–7].

Other dimensionless numbers often encountered in heat transfer problems involving fluid flow include the Reynolds number Re and the Prandtl number Pr. The Reynolds number is defined as the ratio between inertial and viscous forces within a moving fluid [4]:

$$Re = \frac{uL_{ch}}{\nu} \tag{2.9}$$

with u as the flow velocity and ν as the kinematic viscosity. The Prandtl number Pr is a material property and defined as the ratio between momentum diffusivity and thermal diffusivity [3]:

$$Pr = \frac{\nu}{a} = \frac{\nu \rho c_p}{k} \tag{2.10}$$

with a as the thermal diffusivity, ρ as the density and c_p as the specific heat capacity.

2.2 Governing equations and boundary conditions

The governing equations relevant to the problems investigated in the case studies are based on the heat transfer mechanisms discussed in the previous section. Due to the specific nature of the systems and processes considered in this work, it was sufficient to formulate the model equations in only one spatial dimension – a simplification that is further elaborated in the chapters covering the case studies. Consequently, the equations presented in this section and onwards are exclusively formulated for one dimension.

2.2.1 Heat transport equations

In technical applications, knowledge of the temperature field of the considered system is often crucial. In case of steady-state problems, such as heat conduction through the wall

of a building with constant indoor and outdoor temperatures, Fourier's law is directly applicable:

$$\dot{Q} = \dot{q}A = -k\frac{dT}{dx}A \tag{2.11}$$

with x as the spatial coordinate.

In most engineering problems, the temperature distribution within a system varies over time. This is the case for situations with varying boundary conditions or intermittent internal heat generation [2]. Examples include the cooling of a piece of metal by an airstream, the periodic heat generation due to exothermic chemical reactions inside a combustion engine, and – especially relevant for this thesis – the melting and solidification of PCM.

The corresponding governing equation for transient conduction accounts for temperature changes with respect to both time and space. It reads [2]:

$$\rho c_p \frac{\partial T}{\partial t} = \frac{\partial}{\partial x}\left(k\frac{\partial T}{\partial x}\right) \tag{2.12}$$

The left hand-side term describes the accumulation of energy over time t, while the right-hand side term describes the change of heat flux.

In the case of heat transfer by a fluid, energy is also transported by advection. In this work, the only fluid for which the advective heat transport was considered, is water – a liquid that can be treated as incompressible [3,4,7,8]. The corresponding energy transport equation for incompressible fluids is [7]:

$$\rho c_p \left(\frac{\partial T}{\partial t} + u\frac{\partial T}{\partial x}\right) = \frac{\partial}{\partial x}\left(k\frac{\partial T}{\partial x}\right) \tag{2.13}$$

The second term on the left-hand side describes the transport of energy by the fluid in motion, which moves with the velocity u.

Additionally, a source term S for the internal generation of heat may be added to Eq. (2.13):

$$\rho c_p \left(\frac{\partial T}{\partial t} + u\frac{\partial T}{\partial x}\right) = \frac{\partial}{\partial x}\left(k\frac{\partial T}{\partial x}\right) + S \tag{2.14}$$

Heat sources within the system could be chemical reactions, electrical heating or mechanical work.

The above transport equations can also be formulated in spherical and cylindrical coordinates. Particularly the heat conduction equation in spherical coordinates is relevant to this work, since the second case study investigates the conduction-driven phase change inside spherical geometries. However, for the sake of consistency, the fundamental concepts and equations in the following chapters are presented in Cartesian coordinates, while the corresponding equations in spherical coordinates are provided in Appendix A1.

2.2.2 Initial, boundary and interfacial conditions

The solution of the equations discussed in the previous section depends on the physical conditions at the boundary of the considered system. If the problem is transient, the solution also depends on the system conditions at an initial point in time [3]. The initial condition prescribes a temperature distribution $T_0(x)$ across the considered system domain at $t = 0$ [2]:

$$T(x, t = 0) = T_0(x) \tag{2.15}$$

Besides the initial condition, four different types of boundary conditions are commonly encountered in heat transfer, which are illustrated for a one-dimensional plane wall in Figure 2-2 [2].

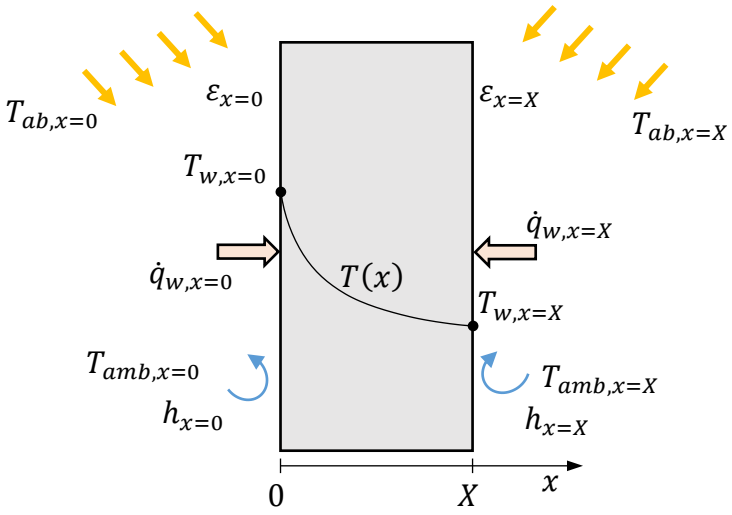

Figure 2-2: Boundary conditions for heat transfer at a one-dimensional plane wall with a total thickness X

The first type, the Dirichlet boundary condition, imposes a temperature profile at the boundary. It is used to model a heated or cooled wall at a prescribed wall temperature T_w:

$$T(x = 0, t > 0) = T_{w,x=0} \tag{2.16}$$

for the point of origin, $x = 0$, of the considered domain, and

$$T(x = X, t > 0) = T_{w,x=X} \tag{2.17}$$

for the end of the domain at $x = X$.

A Neumann boundary condition relates the heat flux at the wall to the temperature gradient by Fourier's law (see section 2.1.1) [3]. It imposes a specific heat flux distribution $\dot{q}_w$ at the boundary, and could be applied at, e.g., an electrically heated wall. It is given as:

$$-k \left.\frac{\partial T}{\partial x}\right|_{x=0} = \dot{q}_{w,x=0} \tag{2.18}$$

$$k\frac{\partial T}{\partial x}\Big|_{x=X} = \dot{q}_{w,x=X} \tag{2.19}$$

The difference in sign between the two equations arises from the directionality of the heat flux, which in this work is defined as positive when it enters the domain. Following Fourier's law, heat entering the domain at $x = 0$ thus leads to a negative temperature gradient, while heat entering the domain at $x = X$ corresponds to a positive temperature gradient (given a uniform initial temperature). In a special case of the Neumann boundary condition, the wall heat flux is zero, corresponding to a perfectly insulated (i.e., adiabatic) boundary or a thermal symmetry condition [2].

The third type is the Robin boundary condition, which specifies a convective heat flux at the boundary. This type of boundary condition is based on Newton's law of cooling (see section 2.1.3) and defines the heat flux at the boundary by a temperature difference between the surface of the domain and the ambient at a temperature T_{amb} [3]:

$$-k\frac{\partial T}{\partial x}\Big|_{x=0} = \dot{q}_{c,x=0} = h\left(T_{amb,x=0} - T(x=0, t>0)\right) \tag{2.20}$$

$$k\frac{\partial T}{\partial x}\Big|_{x=X} = \dot{q}_{c,x=X} = h\left(T_{amb,x=X} - T(x=X, t>0)\right) \tag{2.21}$$

Again, the convective heat flux is considered positive, if the ambient temperature is higher than the surface temperature meaning that heat is transferred into the system. The Robin boundary condition requires knowledge of the problem-specific heat transfer coefficient h, which can be determined by experiments, simulations or correlations.

The fourth type is the radiative heat flux boundary condition, which imposes a heat flux caused by radiation corresponding to the Stefan-Boltzmann law (see section 2.1.2):

$$-k\frac{\partial T}{\partial x}\Big|_{x=0} = \dot{q}_{r,x=0} = \sigma\varepsilon\left(T_{ab,x=0}^4 - T(x=0, t>0)^4\right) \tag{2.22}$$

$$k\frac{\partial T}{\partial x}\Big|_{x=X} = \dot{q}_{r,x=X} = \sigma\varepsilon\left(T_{ab,x=X}^4 - T(x=X, t>0)^4\right) \tag{2.23}$$

with T_{ab} as the effective incoming black body temperature absorbed by the considered object and ε as the emissivity of the object surface (i.e., the boundary).

Additionally, an interfacial condition can be encountered when two regions with different physical properties are in contact. This condition is sometimes considered a boundary condition of the fifth type. If a solid A and a solid B are in contact, without imposing a contact resistance, the condition at the interface position $x = x_{Int}$ is given by:

$$k_A\frac{\partial T_A}{\partial x}\Big|_{x=x_{Int}} = k_B\frac{\partial T_B}{\partial x}\Big|_{x=x_{Int}} \tag{2.24}$$

Other types of boundary conditions can be encountered, e.g., at the interface between two solids in contact moving at different velocities causing friction or at a solid-liquid interface changing its position with time due to a phase transition [2].

The boundary conditions discussed above can be formulated for spherical coordinates simply by replacing x with the radial coordinate r and X with the outer radius of the spherical geometry R. They are given in Appendix A1.

2.3 Phase change materials

PCM refers a group of substances, whose phase change characteristics are utilized for heating or cooling purposes [9]. Usually, PCM are associated with melting and solidification processes (other than boiling and condensation).

The main criteria for the selection of a PCM for a certain application are its phase change temperature and enthalpy [10]. An overview of different classes of PCM, along with their respective phase change temperatures and enthalpies, is given in Figure 2-3.

Other criteria include thermal conductivity, subcooling characteristics, cycle stability, corrosivity, volume change, flammability, toxicity, production cost, etc. [9]

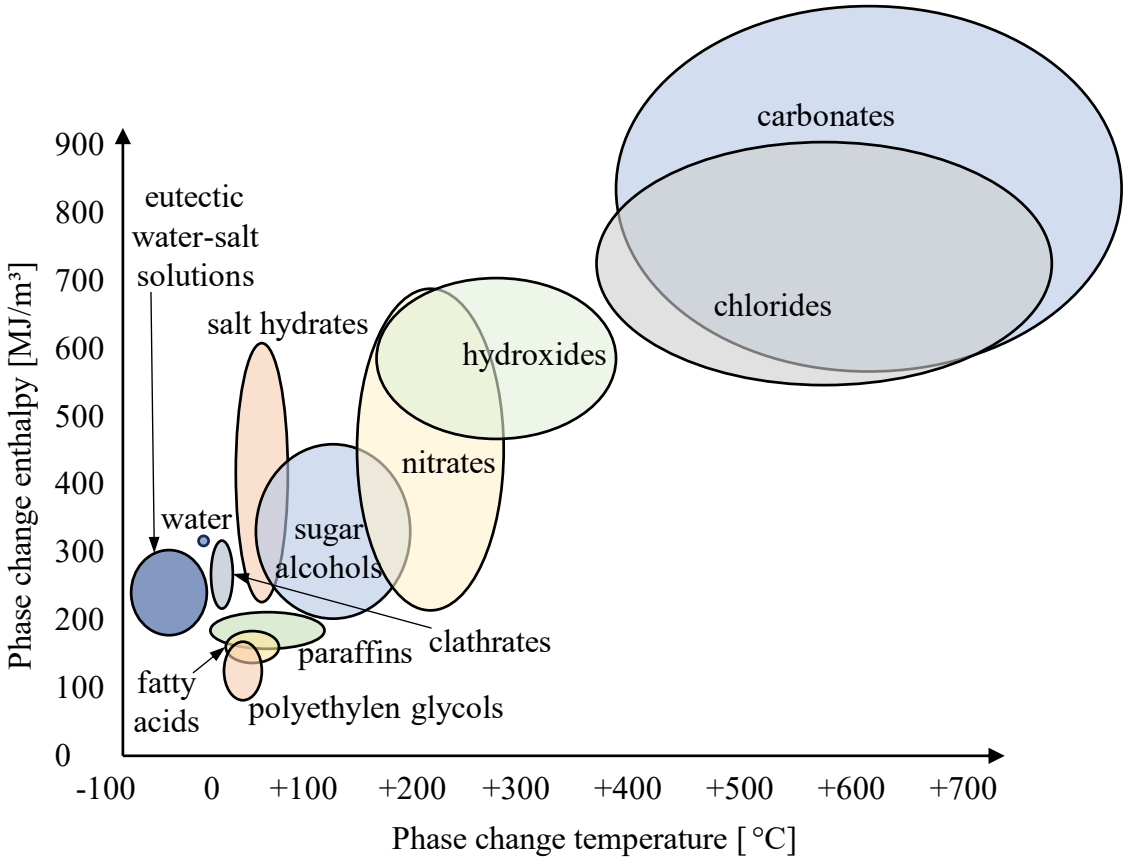

Figure 2-3: Different PCM classes and their phase change temperature and enthalpy (adapted from [10])

The most common PCM is probably water with its ice being used for cooling or, in combination with a heat pump, for heating (ice storage). Due to its large sensible and relatively high latent heat capacity of 333 kJ/kg it is an excellent storage material [10]. However, its use is limited to a narrow temperature range around 0 °C at ambient pressure. Lower phase change temperatures can be achieved by adding salts creating a eutectic water-salt solution, however, at the cost of a lower phase change enthalpy.

For the temperature range of 0 °C to 150 °C, various PCM are available. These can be categorized into organic and inorganic materials based on their chemical composition. Organic PCM, such as paraffins, fatty acids, and sugar alcohols, are non-corrosive, making them compatible with metal components like pipes or storage tanks [10]. In contrast, inorganic materials typically have higher phase change enthalpies and are non-flammable. The corrosiveness of some salt-based PCM can be mitigated by proper encapsulation using organic polymers such as polyethylene [11].

In fact, PCM is often encapsulated to separate the surrounding medium from the PCM and to prevent changes in its chemical composition [10]. However, the encapsulation material adds a thermal resistance that hinders the heat transfer between PCM and its environment. On the other hand, the shape of the capsule can also be used to influence its heat transfer capability [11].

The encapsulation of PCM can be categorized into macroencapsulation and microencapsulation. Macroencapsulation refers to containers that are filled with several milliliters up to several liters of PCM [12]. Such capsules are typically made of plastics, metals, or composite materials. In most cases, a small air volume is encapsulated alongside the PCM to counteract volume changes during phase change. Macroencapsulated PCM elements are mostly used in PBLHS systems. Further applications include stacks of rectangular PCM elements, which can be applied in air conditioning systems [10]. Some examples of PCM macrocapsules are shown in Figure 2-4, left.

Figure 2-4: Three different macroencapsulated PCM elements (left) and microencapsulated PCM (right) [13]

Microencapsulation refers to capsules, with sizes ranging between 1 - 1000 µm [11]. Such small-scale capsules have a very high surface-area-to-volume ratio, which enhances their heat transfer capability. Microcapsules can be easily incorporated into various construction materials, including gypsum boards, plaster, wood products, or polymer binders,

which makes them an option for passive cooling solutions in the construction sector [12]. However, their mechanical stability is rather low due to their thin capsule thickness, and, once they are mixed together with a construction material, it is difficult to replace them. Microencapsulated PCM particles are shown in Figure 2-4, right.

The PCM used in this work were based on paraffins and salt hydrates, encapsulated in high-density polyethylene (HDPE) and polypropylene (PP). Their phase change temperatures typically can range between 0 °C and 120 °C, with some salt-based PCM reaching phase change temperatures as low as -63 °C [14]. Especially salt hydrates offer great potential as heat storage materials due to their comparatively high density. They are composed of a mixture of water and salt in a defined ratio, forming a crystalline structure. However, common issues with salt hydrate PCM include a tendency to undergo subcooling and phase separation [11]. Paraffin PCM are linear alkanes. They have a low subcooling tendency and are nearly non-flammable. Since they are not corrosive, they are compatible with metals. However, their volumetric storage capacity is lower compared to salt hydrates due to their lower density. Also, they exhibit a relatively low thermal conductivity [11].

2.4 Heat transfer involving solid-liquid phase change

The phase change from solid to liquid and vice versa plays an important role in various engineering problems, from metal smelting to the industrial production of ice cubes. Phase change processes of pure substances occur at a constant temperature called melting point, phase change temperature or fusion temperature. For example, for water at standard conditions, this temperature is 0 °C. During the phase change, some energy, called latent heat of fusion or phase change enthalpy, is removed from or added to the system while the temperature remains constant. On a molecular level, latent enthalpy is the energy needed to overcome the binding forces of the lattice structure of the solid. A phase change process is illustrated in Figure 2-5, left, in which the energy-temperature relationship for a pure substance undergoing phase change is shown. During phase change the temperature remains constant, but the material continues to absorb energy. Since this energy increase cannot be detected by temperature sensors it is called “latent”, as opposed to the gradual, sensible temperature increase taking place below or above the melting point. The same phenomenon can be observed during evaporation and condensation.

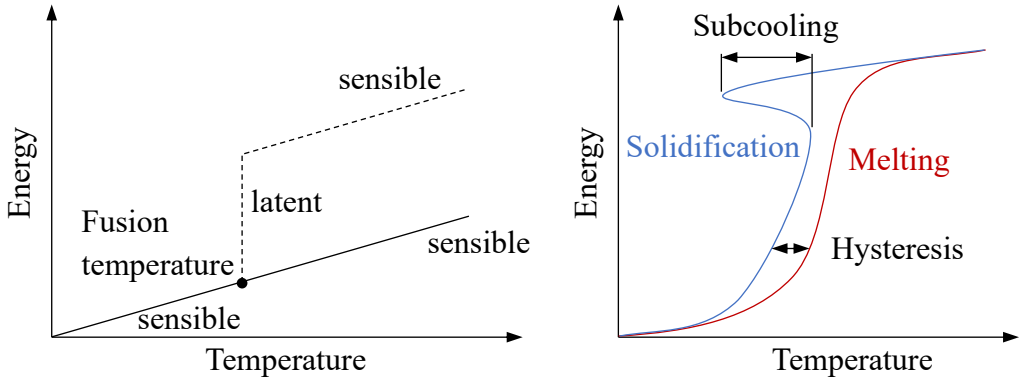

Figure 2-5: Energy-temperature relationship for a pure substance undergoing phase change (dashed line) and a substance without phase change (solid line) (left) and the phase change of a real PCM with subcooling and hysteresis (right)

Along with the effect of the latent heat, other physical phenomena may play a significant role during the phase change. Among others, the thermo-physical properties of a substance can change rapidly, density changes may cause natural convection increasing the heat transport within the liquid phase, or the shape of the solid-liquid phase front may vary from being a sharp, infinitesimally thin interface to more complex dendritic structures or a mushy, slush-like transition region. Further, PCM are usually mixtures and therefore exhibit a non-isothermal phase change. Also, they often show a tendency to subcooling and hysteresis. Subcooling can lead to the initiation of solidification at temperatures lower than the fusion temperature, while hysteresis refers to the phenomenon where the shape of the energy-temperature curve depends on whether the PCM is currently melting or solidifying. The phase change process of a typical PCM including subcooling and hysteresis is shown in Figure 2-5, right. Other challenges arising during phase change are extensively discussed in the literature [10,15,16].

Some of the effects outlined above were not considered in this work. Natural convection in the liquid PCM phase was neglected due to its relatively high viscosity and the small scale of the PCM geometries used. Subcooling effects were also not considered, since the PCM that were used showed a low subcooling tendency in the scale of less than 2 K.

2.4.1 The Stefan problem

In melting and solidification problems, often the position of the interface between the liquid and solid region is of interest. Since the interface position changes with time, such problems are also referred to as moving boundary problems. An example is the melting of a pure substance, during which the solid-liquid interface and the temperature distribution evolve with time, as illustrated in Figure 2-6. Josef Stefan introduced this class of problems in his publication on oceanic ice formation in 1891, which is why this type of problem is also called “Stefan problem” [2]. In a mathematical sense, a Stefan problem constitutes a boundary value problem, for which the position of the boundary itself is a function of time.

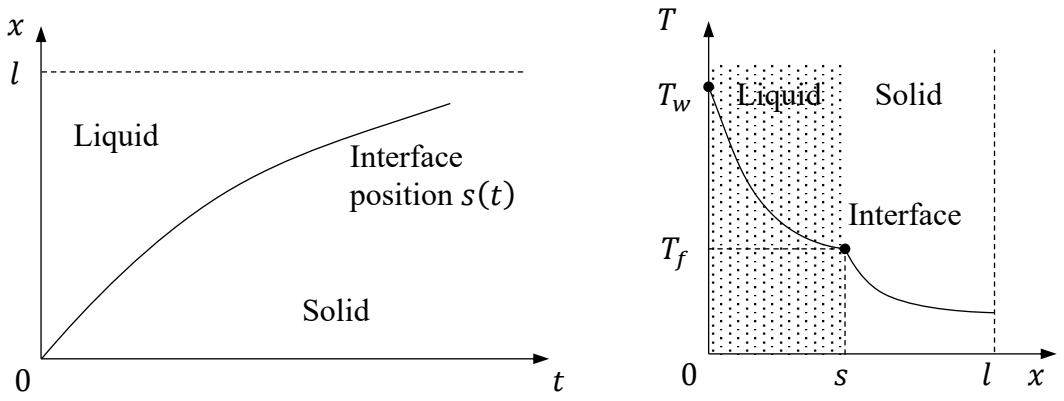

Figure 2-6: Position of the phase front (left) and temperature curve for a specific point in time $t > 0$ (right) for a melting problem of a one-dimensional slab ($0 < x < l$)

The classical Stefan problem was formulated using several assumptions and simplifications. For a melting process, it can be stated as follows [15]: a semi-infinite, one-dimensional slab, $0 \leq x \leq \infty$, consisting of a pure solid is subjected at $x = 0$ to a constant temperature T_w, which is higher than the fusion temperature T_f. Initially, the slab has a uniform temperature equal to T_f. Density, specific heat capacity and thermal conductivity remain constant. The goal is to find the time-dependent position of the solid-liquid interface $s(t)$ and the transient temperature distribution across the slab.

The governing equation for the active phase is given as:

$$\rho c_p \frac{\partial T}{\partial t} = k \frac{\partial^2 T}{\partial x^2} \tag{2.25}$$

The term “active phase” refers to the phase that is building up due to the movement of the solid-liquid interface, i.e., the solid phase during solidification and the liquid phase during melting. The thermal properties in Eq. (2.25) are those of the active phase.

At the beginning of the melting process considered here, the slab is at fusion temperature and the phase front has not formed yet:

$$T(x, t = 0) = T_f \tag{2.26}$$

$$s(t = 0) = 0 \tag{2.27}$$

The boundary condition at the heated wall is:

$$T(x = 0, t > 0) = T_w > T_f \tag{2.28}$$

The temperature at the solid-liquid interface takes the value of the fusion temperature:

$$T(x = s(t), t > 0) = T_f \tag{2.29}$$

Further, energy conservation must be maintained at the interface:

$$k_l \left.\frac{\partial T}{\partial x}\right|_{x=s(t)} + \rho_s L \frac{ds}{dt} = 0 \tag{2.30}$$

with L as the latent heat of fusion. Eq. (2.30) is also referred to as Stefan condition and states that the difference in heat flux across the solid-liquid interface is proportional to the velocity of the interface [2].

For a corresponding problem involving the solidification of a slab due to a cooled wall having a temperature of $T_w < T_f$, the latent heat term in Eq. (2.30) becomes negative.

2.4.2 Neumann's solution to the Stefan problem

Already in 1865, Franz Neumann proposed a solution to the class of problems that was later named after Stefan [17]. By making use of the similarity method, Neumann found a solution that yields the position of the solid-liquid interface as a function of time [15]:

$$s(t) = 2\lambda\sqrt{at} \tag{2.31}$$

with $a = \frac{k}{\rho c_p}$ as the thermal diffusivity and λ as a constant.

Additionally, the temperature in the active phase is given as:

$$T(x, t > 0) = T_w + \left(T_f - T_w\right) \frac{\mathrm{erf}\left(x/\sqrt{4at}\right)}{\mathrm{erf}(\lambda)} \tag{2.32}$$

The constant λ can be determined by solving the following transcendental equation:

$$\frac{St}{e^{\lambda^2}\,\mathrm{erf}(\lambda)} = \lambda\sqrt{\pi} \tag{2.33}$$

The Stefan St number describes the ratio of the sensible heat difference resulting from the temperature change within the active region to the phase change enthalpy. It is defined as:

$$St = \frac{c_p \left|T_w - T_f\right|}{L} \tag{2.34}$$

The Stefan problem described in the previous section and the Neumann solution discussed here were used for the validation of the numerical method for phase change problems that is outlined in Chapter 3.

2.4.3 Solutions for spherical geometries

Neumann's solution of the Stefan problem described in the previous section was derived for geometries that can be well described in Cartesian coordinates. For spheres and cylinders, explicit analytical solutions exist only in rare cases, such as phase change due to a line or point heat sink/source in a large medium [2]. Approximate analytical solutions

that can be applied to cylinders and spheres are available for small Stefan numbers (i.e., $St \approx 0$), which means that the sensible heat is negligible in comparison to the latent heat. In [4], the upper limit for the Stefan number is given as $1/St > 7$ for such problems.

Since the one-dimensional inward melting of a sphere via a convective heat flux on its surface was used as a benchmark for the model developed in the second case study, the approximate solution for such a problem is given here. A sphere of solid PCM at fusion temperature T_f and with a radius R is considered, see Figure 2-7, left. At its surface, a fluid that has an ambient temperature of $T_{amb} > T_0$ causes a convective heat flux characterized by the heat transfer coefficient h. This heat flux transfers energy into the sphere, which leads to the melting of the PCM.

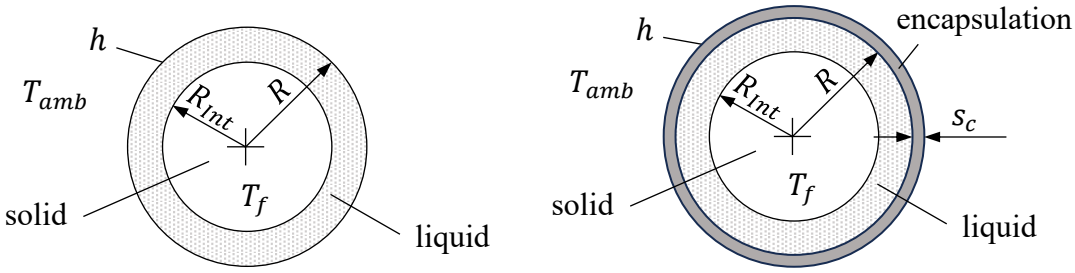

Figure 2-7: Solid and liquid phases inside a PCM sphere, without (left) and with (right) encapsulation, during melting caused by a convective heat flux

The approximate solution for such a problem is given in [15] in terms of the temperature profile along the radius:

$$T(r,t) = T_f + \left(T_{amb} - T_f\right) \frac{1 - \frac{R_{Int}(t)}{r}}{1 - \left(1 - \frac{k}{hR}\right)\frac{R_{Int}(t)}{R}} \tag{2.35}$$

The time-dependent radius of the phase front R_{Int} is given by the following cubic equation:

$$2\left(1 - \frac{k}{hR}\right)\left(\frac{R_{Int}(t)}{R}\right)^3 - 3\left(\frac{R_{Int}(t)}{R}\right)^2 + 1 + \frac{2k}{hR} = \frac{6kt}{\rho L R^2}\left(T_{amb} - T_f\right) \tag{2.36}$$

In [18], Baehr & Stephan present a solution for an encapsulated PCM sphere, such as the one illustrated in Figure 2-7, right, in terms of the melting time t_{melt}, which is the time needed for the whole PCM domain to liquify:

$$t_{melt} = \frac{L\rho(R - R_{Int})^2}{2k(T_0 - T_{amb})} f_{sph} \tag{2.37}$$

with the spherical correction factor f_{sph} as:

$$f_{sph} = 1 - \frac{2}{3}s^+ + \frac{2\alpha}{s^+}\left(1 - s^+ + \frac{{s^+}^2}{3}\right) \tag{2.38}$$

where $s^+ = (R - R_{Int})/R$ is the dimensionless wall distance, and α is given as:

$$\alpha = \frac{k}{k_C}\frac{s_C}{R + s_C} + \frac{k}{h(R + s_C)}\frac{R}{R + s_C} \tag{2.39}$$

Here, s_C is the thickness of the encapsulation, which has the inner radius R and a thermal conductivity of k_C. Solutions for problems involving cylinders and spheres with boundary conditions other than the convective heat flux condition discussed in this section can be found in, e.g., [2,15,18].

2.5 Numerical solution techniques for phase change problems

In this section, the finite difference method – an approach to solve unsteady heat transfer problems – is introduced. The focus is laid on the discretization of the advection-conduction equation, Eq. (2.14), as it governs the thermal processes that are relevant for this thesis. Additionally, numerical techniques addressing heat transfer problems involving melting and solidification are discussed. Special attention is given to fixed grid methods, particularly the enthalpy and the source term method.

2.5.1 The finite difference method

The partial differential equations governing the processes investigated in this work were solved numerically. The use of numerical methods was necessary due to the complex nature of these processes, which involve phase changes, varying boundary conditions, and changing material properties. Obtaining exact analytical solutions in such cases is often very challenging or impossible [4]. For this reason, the finite difference method (FDM) was employed – a numerical technique that divides the continuous spatial and temporal domains into a finite number of discrete points, usually called “node” for space and “step” for time, forming a grid [19]. As an example, Figure 2-8 shows the discretization of a function $f(x)$ into a finite number of points forming a grid with equal spacing Δx. At the grid points, the time and space derivatives of the equation to be solved can be approximated by finite differences resulting in difference quotients for each grid point. This procedure results in a set of linear, algebraic equations which can be solved directly or by various matrix operations.

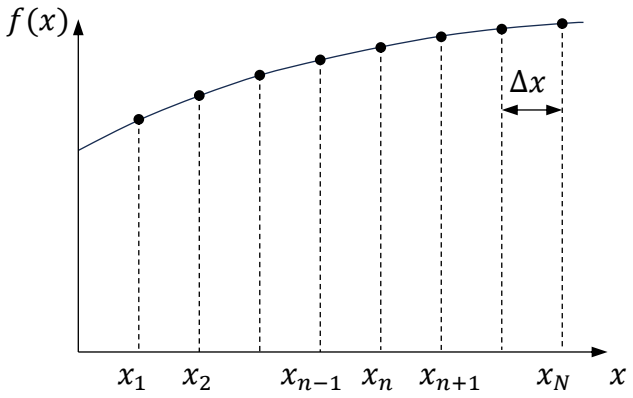

Figure 2-8: Discretization nodes (subscript n) for a function $f(x)$ on a grid with equal spacing Δx

Considering the advection-conduction equation, Eq. (2.14), with its three characteristic terms accounting for accumulation (time derivative), advection (first order spatial derivative), and conduction (second order spatial derivative), the finite difference approach allows different ways of discretization. First derivatives can be approximated by applying backward differences using the neighboring, previous (left) point or forward differences by using the next (right) point [2]:

$$\left.\frac{\partial f(x)}{\partial x}\right|_{x_n} \approx \frac{f(x_n) - f(x_{n-1})}{\Delta x} \tag{2.40}$$

or

$$\left.\frac{\partial f(x)}{\partial x}\right|_{x_n} \approx \frac{f(x_{n+1}) - f(x_n)}{\Delta x} \tag{2.41}$$

Also, central differences may be applied by using both the previous and the next point with $2\Delta x$ as the quotient:

$$\left.\frac{\partial f(x)}{\partial x}\right|_{x_n} \approx \frac{f(x_{n+1}) - f(x_{n-1})}{2\Delta x} \tag{2.42}$$

Central differences are usually also applied to second derivatives resulting in:

$$\left.\frac{\partial^2 f(x)}{\partial x^2}\right|_{x_n} \approx \frac{f(x_{n+1}) - 2f(x_n) + f(x_{n-1})}{\Delta x^2} \tag{2.43}$$

More advanced schemes exist, which use three or more additional grid points to approximate a derivative (see [19,20]).

The choice of the appropriate finite difference scheme depends on the specific problem, the desired accuracy of the solution and the computational resources available. Generally, finer grid spacing reduces the approximation error, however, it also leads to a higher number of algebraic equations to be solved and, therefore, requires higher computational

power. The quality of the finite difference approximation, usually expressed as truncation error, can be determined by Taylor series expansion, which shows that central differences are second-order accurate, while backward and forward differences are only first-order accurate [20]. However, it is not always possible to use central differences. For example, applying central differences to the advection term in Eq. (2.14) for an advection-dominated heat transfer problem can lead to unrealistic results due to the asymmetrical and direction-based nature of advection. In such a case, backward, or "upwind", differences can be used, as they account for the flow direction by considering the neighboring node upstream [8].

2.5.1.1 Discretization of the advection-conduction equation

The previously discussed FDM can now be used to discretize the individual terms in Eq. (2.14). Applying the first order upwind approach, the convection term becomes:

$$u\frac{\partial T}{\partial x}\bigg|_n \approx u\,\frac{T_n - T_{n-1}}{\Delta x} \tag{2.44}$$

The spatial term can be discretized using central differences:

$$\begin{aligned}\frac{\partial}{\partial x}\left(k\frac{\partial T}{\partial x}\right)\bigg|_n &\approx \frac{\left[k_{n+\frac{1}{2}}\frac{\partial T}{\partial x}\Big|_{n+\frac{1}{2}} - k_{n-\frac{1}{2}}\frac{\partial T}{\partial x}\Big|_{n-\frac{1}{2}}\right]}{\Delta x}\\ &\approx \frac{(k_{n+1}+k_n)}{2\Delta x^2}T_{n+1} - \frac{(k_{n+1}+2k_n+k_{n-1})T_n}{2\Delta x^2}\\ &\quad + \frac{(k_n+k_{n-1})}{2\Delta x^2}T_{n-1}\end{aligned} \tag{2.45}$$

where $k_{n+\frac{1}{2}} = (k_{n+1}+k_n)/2$ and $k_{n-\frac{1}{2}} = (k_{n-1}+k_n)/2$ are the mean conductivities between two adjacent spatial nodes. Here, the thermal conductivity k is considered to be a function of space. If that was not the case, the first three terms on the right hand-side would become $\frac{k}{\Delta x^2}\left(T_{n+1}^j - 2T_n^j + T_{n-1}^j\right)$, an expression often found in literature [2,4,20].

Applying forward differences at time step j, the transient term becomes:

$$\rho c_p \frac{\partial T}{\partial t}\bigg|^j \approx \rho c_p \frac{T^{j+1} - T^j}{\Delta t} \tag{2.46}$$

Alternatively, the transient term can also be approximated by backward differencing at $j+1$, which results in the same discretized equation:

$$\rho c_p \frac{\partial T}{\partial t}\bigg|^{j+1} \approx \rho c_p \frac{T^{j+1} - T^j}{\Delta t} \tag{2.47}$$

While in both cases the temperature T^{j+1} is the unknown quantity, the difference between these two approaches lies in the time step at which the spatial derivatives are evaluated.

In case forward differencing is applied at time step j, the discretized form of the advection-diffusion equation results from inserting equations (2.44) - (2.46) into Eq. (2.14):

$$\rho c_p \frac{T_n^{j+1} - T_n^j}{\Delta t} + u \frac{T_n^j - T_{n-1}^j}{\Delta x} = \frac{(k_{n+1} + k_n)}{2\Delta x^2} T_{n+1}^j - \frac{(k_{n+1} + 2k_n + k_{n-1}) T_n^j}{2\Delta x^2} + \frac{(k_n + k_{n-1})}{2\Delta x^2} T_{n-1}^j + S^j \tag{2.48}$$

Eq. (2.48) can relatively easily be rearranged for T_n^{j+1}, the sought temperature at location x_n and time step $j+1$. It can be seen that T_n^{j+1} only depends on known values from the current time step j. Therefore, this approach is referred to as explicit FDM, because it is possible to determine T_n^{j+1} exclusively from preceding temperature values [2].

Alternatively, backward differencing at time step $j+1$ yields an implicit expression for T_n^{j+1}:

$$\rho c_p \frac{T_n^{j+1} - T_n^j}{\Delta t} + u \frac{T_n^{j+1} - T_{n-1}^{j+1}}{\Delta x} = \frac{(k_{n+1} + k_n)}{2\Delta x^2} T_{n+1}^{j+1} - \frac{(k_{n+1} + 2k_n + k_{n-1})}{2\Delta x^2} T_n^{j+1} + \frac{(k_n + k_{n-1})}{2\Delta x^2} T_{n-1}^{j+1} + S^{j+1} \tag{2.49}$$

Additionally, the implicit finite differences discretization of the heat conduction equation in spherical coordinates is given in Appendix A1.

The unknown temperature T_n^{j+1} in Eq. (2.49) can only be determined by solving a system of linear equations, which requires a more complex solution method compared to the explicit approach. However, the implicit FDM offers the significant advantage of unconditional stability, while the explicit method requires one or more stability criteria [8]. To assess whether a discretization scheme is stable, the numerical Fourier number Fo_{num} and the Courant number CFL can be evaluated. For the one-dimensional explicit FDM, they need to fulfil the following conditions [19]:

$$Fo_{num} = a \frac{\Delta t}{\Delta x^2} \leq 0.5 \tag{2.50}$$

$$CFL = u \frac{\Delta t}{\Delta x} \leq 1 \tag{2.51}$$

Note that the CFL-criterion is a necessary but not sufficient condition for stability, as more restrictive conditions may arise depending on the nature of the problem being investigated. Further discussion regarding the stability of explicit and implicit finite difference methods can be found in [4,8,19].

A consequence resulting from the stability criteria for the explicit scheme is that the grid sizes for time and space, Δt and Δx, are not independent from each other. For a given spatial increment Δx, the chosen time step size Δt must fulfil the conditions resulting from equations (2.50) and (2.51), i.e., $\Delta t \leq \frac{1}{2}\frac{\Delta x^2}{a}$ and $\Delta t \leq \frac{\Delta x}{u}$, which impose a strict upper limit on Δt. This represents a significant limitation for the explicit scheme, since a reduction of Δx requires a consequent reduction of Δt [8]. Particularly for cases when high spatial resolution is required, such grid refinements quickly lead to a significant computational effort, since not only the number of spatial nodes increases, but also the number of time steps. The same issue can arise for problems that involve high flow velocities u or materials with a high thermal diffusivity (e.g., silicon with a = 88 mm²/s or copper with a = 111 mm²/s).

In contrast, the implicit formulation does not require the fulfilment of such stability criteria and therefore allows larger time steps, significantly reducing computation time. For this reason, the implicit method is recommended for most transient problems [8].

Other finite difference schemes exist, such as the Crank-Nicolson method, which represents a combination of explicit and implicit FDM. This method is second order accurate in time but also requires adherence to a Fo_{num} stability criterion (though less restrictive than that of the explicit scheme). The Crank-Nicolson scheme and other higher order methods are extensively discussed in [8,19,20].

2.5.1.2 Discretization of boundary conditions

Besides the governing advection-conduction equation, the corresponding boundary conditions need to be discretized as well. The boundary conditions at the first node, $n = 1$, of a spatially discretized computational domain are shown in Figure 2-9.

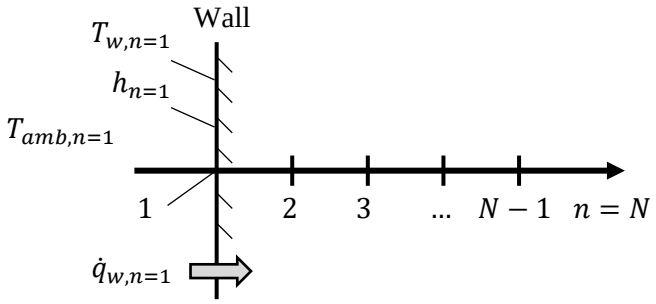

Figure 2-9: Illustration of boundary the conditions at the first node of a discretized one-dimensional domain

For Dirichlet boundary conditions (Eq. (2.16)), the first node $n = 1$ is considered the heated/cooled wall, from which it follows that:

$$T_{n=1} = T_{w,n=1} \quad \& \quad k_{n=1} = k_{w,n=1} \tag{2.52}$$

For Neumann boundary conditions (Eq. (2.18)), the temperature at the wall is not explicitly prescribed. Instead, the heat flux at node $n = 1$ is specified. Here, the spatial derivative $\frac{\partial}{\partial x}\left(k\frac{\partial T}{\partial x}\right)\Big|_{n=1}$ can conveniently be approximated over half a spatial increment:

$$\frac{\partial}{x}\left(k\frac{\partial T}{\partial x}\right)\Big|_{n=1} \approx \frac{2}{\Delta x}\left(k_{n=1^1/_2}\frac{\partial T}{\partial x}\Big|_{n=1^1/_2} - k_{n=1}\frac{\partial T}{\partial x}\Big|_{n=1}\right) \tag{2.53}$$

Inserting Eq. (2.18) into Eq. (2.53) replaces the term for node n = 1 with $\dot{q}_{w,n=1}$:

$$\begin{aligned}\frac{\partial}{\partial x}\left(k\frac{\partial T}{\partial x}\right)\Big|_{n=1} &\approx \frac{2}{\Delta x}k_{n=1^1/_2}\frac{\partial T}{\partial x}\Big|_{n=1^1/_2} + \frac{2}{\Delta x}\dot{q}_{w,n=1} \\ &\approx \frac{(k_2+k_1)}{\Delta x^2}(T_2 - T_1) + \frac{2}{\Delta x}\dot{q}_{w,n=1}\end{aligned} \tag{2.54}$$

For Robin boundary conditions, the term $-k\frac{\partial T}{\partial x}\Big|_{n=1}$ in Eq. (2.53) is replaced by a convective heat flux (Eq. (2.20)):

$$\frac{\partial}{\partial x}\left(k\frac{\partial T}{\partial x}\right)\Big|_{n=1} \approx \frac{(k_2+k_1)}{\Delta x^2}(T_2 - T_1) + \frac{2}{\Delta x}h_{n=1}\left(T_{amb,n=1} - T_1\right) \tag{2.55}$$

The radiative boundary condition introduces a non-linearity into the linear equation system due to temperatures raised to the fourth power, which significantly increases the complexity of the solution procedure. Therefore, the following linearization is often used in literature [2,4]:

$$-k\frac{\partial T}{\partial x}\Big|_{n=1} = \sigma\varepsilon\left(T_{ab,n=1}^4 - T_1^4\right) \approx h_{r,n=1}\left(T_{ab,n=1} - T_1\right) \tag{2.56}$$

where $h_{r,n=1}$ is a radiative heat transfer coefficient defined as:

$$h_{r,n=1} = \sigma\varepsilon F\left[\left(T_1^2 + T_{ab,n=1}^2\right)\left(T_1 + T_{ab,n=1}\right)\right] \tag{2.57}$$

Here, F represents a factor which accounts for the orientation of the surfaces involved in the radiative heat exchange. The linearized radiation boundary condition is formally identical to the convective boundary condition and can therefore be implemented similarly.

The discretized boundary conditions at the end of the domain at node $n = N$ can be derived in a similar manner, resulting in:

$$T_{n=N} = T_{w,n=N} \quad \& \quad k_{n=N} = k_{w,n=N} \tag{2.58}$$

for Dirichlet boundary conditions,

$$\frac{\partial}{\partial x}\left(k\frac{\partial T}{\partial x}\right)\Big|_{n=N} \approx \frac{(k_N + k_{N-1})}{\Delta x^2}(T_N - T_{N-1}) + \frac{2}{\Delta x}\dot{q}_{w,n=N} \tag{2.59}$$

for Neumann boundary conditions, and

$$\frac{\partial}{\partial x}\left(k\frac{\partial T}{\partial x}\right)\Big|_{n=N} \approx \frac{(k_N + k_{N-1})}{\Delta x^2}(T_N - T_{N-1}) + \frac{2}{\Delta x}h_{n=N}\left(T_{amb,n=N} - T_N\right) \qquad (2.60)$$

for Robin and linearized radiative boundary conditions.

The discretization procedure for boundary conditions formulated in spherical coordinates is given in Appendix A1.

2.5.2 Fixed grid methods for melting and solidification problems

After introducing the FDM for general heat transfer problems in the previous section, the following part focuses on the application of this method to heat transfer problems involving melting and solidification processes. Finite difference approaches for phase change problems can be divided into variable and fixed grid methods, as shown in Figure 2-10 [21]. Using the variable grid approach, the exact location of the phase change interface can directly be determined. This can be achieved by establishing one computational domain for the solid and one for the liquid part and using either an interface fitting method or a dynamic spatial grid. The interface fitting method is based on the adjustment of the time step size (see [22]), while the dynamic grid method is based on an adaptive spatial grid size (see [23,24]). Both methods aim to align the interface with the spatial grid points, making them suitable for problems with sharp, infinitesimally thin interfaces, typically encountered in phase change processes of pure substances [25]. However, they are computationally expensive and challenging to implement, as they require continuous grid adaptation [26].

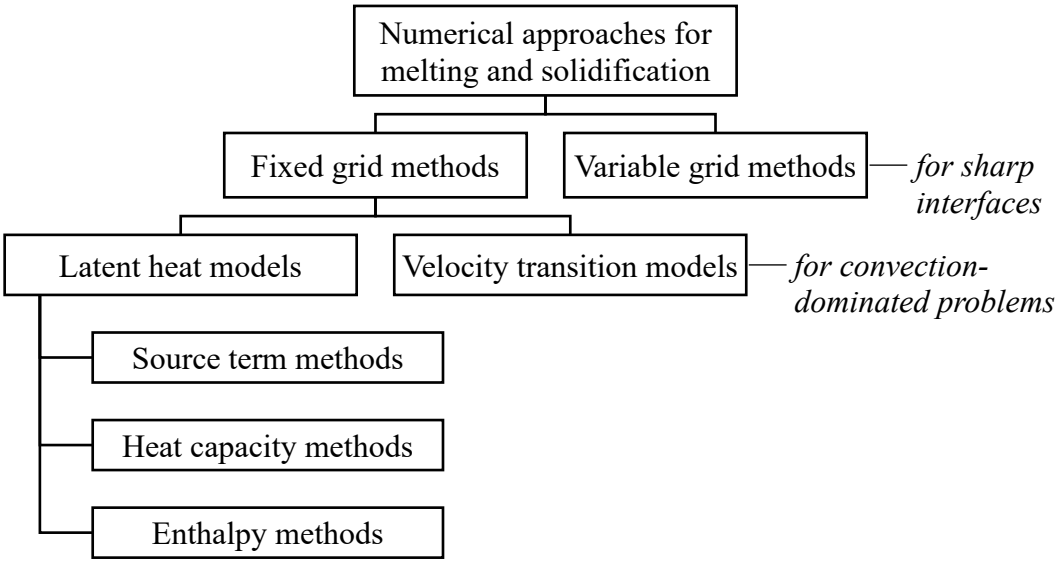

Figure 2-10: Classification of numerical methods for phase change problems (adapted from [25])

On the other hand, fixed grid methods, which only require one computational domain comprising all involved phases, are commonly used for phase change problems involving mixtures such as PCM [25–27]. Mixtures typically exhibit non-isothermal phase change

behavior across a temperature interval leading to the formation of a phase transition zone (also referred to as mushy zone) instead of a sharp solid-liquid interface, as illustrated in Figure 2-11 [10]. The phase change temperature interval is confined by the solidification temperature, also referred to as solidus temperature, and the melting temperature, also referred to as liquidus temperature. Compared to the interfaces seen with pure substances, the numerical treatment of continuous transition zones encountered for mixtures is less challenging, because the properties of the material change gradually over time and space during a phase change [25]. This enables the use of a static instead of an adaptive grid, significantly reducing the computational effort and the complexity of implementation [26]. However, a non-isothermal phase change is not a necessary requirement for using a fixed grid method. Particularly, the fixed-grid based enthalpy method has been reported to give accurate results also for isothermal phase change processes [15,26,28,29]. Therefore, the fixed grid approach is considered versatile and applicable to a broad range of phase change scenarios, while maintaining a low computational effort and ease of implementation.

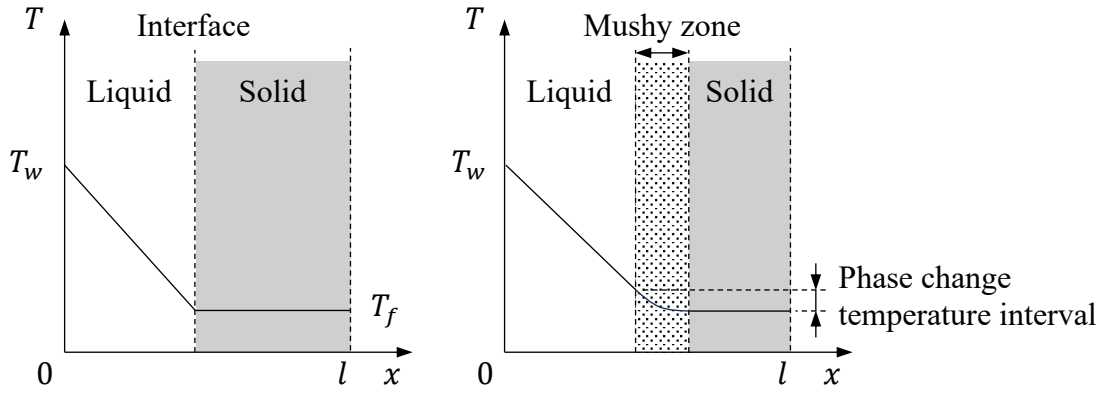

Figure 2-11: Sharp solid-liquid interface during melting of a pure substance (left) and phase transition, or mushy, zone during melting of a PCM mixture (right)

Fixed grid methods can be further categorized based on the modifications made to the governing equations in order to accurately capture the evolution of the phase front. If convective flows within the liquid PCM are to be considered, so-called “velocity transition models” can be applied [25]. Since this approach involves solving the Navier-Stokes equations, the model complexity increases significantly compared to purely conduction driven phase change processes. Whether the inclusion of convection is required depends on the nature of the considered problem (temperature gradients, geometry) and the material properties of the PCM (viscosity, chemical composition).

In the phase change problems discussed in this thesis, convective flows were neglected due to the high viscosity of the liquid PCM and the geometrical shape of the encapsulation. For such problems, so-called “latent heat models” are suitable, which can be categorized according to how the latent heat evolution is incorporated into the heat conduction equation: by modifying the specific heat capacity during the phase change, by expressing the heat conduction equation in terms of enthalpy and/or by adding a source term [27].

Heat capacity methods add the latent heat to the specific heat capacity during phase change:

$$c_{app} = \begin{cases} c_{p,s} & if \quad T < T_s \\ \dfrac{\int_{T_s}^{T_l} c_p dT + L}{T_l - T_s} & if \quad T_s \leq T \leq T_l \\ c_{p,l} & if \quad T > T_l \end{cases} \tag{2.61}$$

In the heat conduction equation, Eq. (2.12), the specific heat capacity is then replaced by the apparent heat capacity c_{app}:

$$\rho c_{app} \frac{\partial T}{\partial t} = \frac{\partial}{\partial x}\left(k \frac{\partial T}{\partial x}\right) \tag{2.62}$$

A shortcoming associated with this method is the requirement of very small time steps in cases when the phase change temperature interval is small and/or large temperature gradients are encountered [27].

The enthalpy method is based on the enthalpy formulation of the heat conduction equation and is viewed as the preferable method to numerically solve phase change problems, due to its versatility and simple implementation [15]. Adopting the enthalpy method, Eq. (2.12) becomes:

$$\frac{\partial H}{\partial t} = \frac{\partial}{\partial x}\left(k \frac{\partial T}{\partial x}\right) \tag{2.63}$$

The enthalpy H contains information about the energy within the solid, liquid, and mushy phases of the PCM, and therefore represents a mixture enthalpy [26]. It is not necessary to explicitly track the phase transition zone (or the solid-liquid interface in case of an isothermal phase change), as the enthalpy captures the total energy of the PCM across its three states (solid, mushy, and liquid). This allows the mushy zone (or interface) location to be derived a posteriori. The mixture enthalpy can be calculated using the following relationship [26]:

$$H = (1 - \gamma) \int_{T_{ref}}^{T} \rho_s c_{p,s} dT + \gamma \rho_l L + \gamma \int_{T_{ref}}^{T} \rho_l c_{p,l} dT \tag{2.64}$$

The liquid fraction γ indicates the state of the material undergoing phase change ranging from 0 (solid) to 1 (liquid). Often, it is simply modeled as a linear function of temperature [28]:

$$\gamma = \begin{cases} 0 & if \quad T < T_s & \text{solid} \\ \dfrac{T - T_s}{T_l - T_s} & if \quad T_s \leq T \leq T_l & \text{mushy} \\ 1 & if \quad T > T_l & \text{liquid} \end{cases} \tag{2.65}$$

However, depending on the nature of the phase change process, it may be necessary to employ a more complex $\gamma(T)$-relationship in order to accurately capture the phase change behavior. Examples of more intricate liquid fraction curves are shown in Figure 2-12.

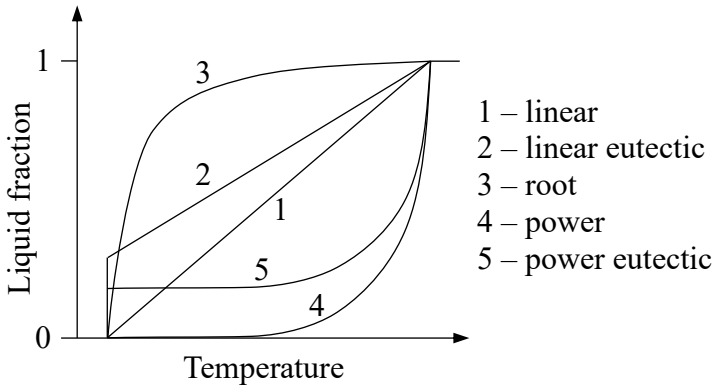

Figure 2-12: Different liquid fraction curves (adapted from [30])

An extension of the classical enthalpy method is the source term method, which adds a source term to the heat conduction equation. It is derived by inserting the definition of the mixture enthalpy, Eq. (2.64), into Eq. (2.63) resulting in [26]:

$$c_{vol}\frac{\partial T}{\partial t} = \frac{\partial}{\partial x}\left(\lambda\frac{\partial T}{\partial x}\right) - \rho_l L\frac{\partial \gamma}{\partial t} \tag{2.66}$$

where c_{vol} is the volumetric heat capacity of the mixture defined as:

$$c_{vol} = (1-\gamma)\rho_s c_{p,s} + \gamma\rho_l c_{p,l} \tag{2.67}$$

while λ is the mixture conductivity:

$$\lambda = (1-\gamma)k_s + \gamma k_l \tag{2.68}$$

and $\rho_l L$ becomes:

$$\rho_l L = \left(\rho_l c_{p,l} - \rho_s c_{p,s}\right)T + \rho_l L_p \tag{2.69}$$

While the purely latent heat L_p in Eq. (2.69) represents the part of the phase change enthalpy that is released/absorbed during an isothermal phase change, the new term accounts for the additional effect of changing thermal properties during a non-isothermal phase change. It is difficult to experimentally determine these two effects separately as they occur simultaneously. For this reason, the manufacturer of the PCM used in this work only provides the overall phase change enthalpy L in its data sheets, which includes both the isothermal and the non-isothermal effect (see [14]). Therefore, the latent enthalpy values used in the case studies refer to the overall phase change enthalpy L and not just the purely latent part L_p.

The equivalent to Eq. (2.66) in spherical coordinates is:

$$c_{vol}\frac{\partial T}{\partial t} = \frac{1}{r^2}\frac{\partial}{\partial r}\left(\lambda r^2 \frac{\partial T}{\partial r}\right) - \rho_l L \frac{\partial \gamma}{\partial t} \tag{2.70}$$

A key feature of the source term method is that equations (2.66) and (2.70) are valid throughout the whole domain of a phase change system dominated by thermal conduction. Also, the non-linearity present in the standard enthalpy method is moved to the source term, which allows for a simpler numerical treatment [31]. For these reasons, the source term method was chosen to model the phase change processes in this work.

Other numerical approaches for melting and solidification problems exist, but are not widespread due to various shortcomings, such as instabilities, the need for very small time steps or low accuracy [27].

2.6 Summary and conclusion

In this chapter, theoretical background information relevant to the problems discussed in the case studies presented in Chapters 4 and 5 was provided. By introducing the basic mechanisms of heat transfer, the foundation for the description of solid-liquid phase change problems was established and corresponding solution techniques were provided.

Phase change problems involving pure substances, simple geometries, and only one active phase can be formulated as Stefan problems and solved analytically. However, more complex problems, such as those involving compound materials, like PCM, and more than one active phase, are easier to solve numerically. A numerical method recommended for transient heat transfer problems is the implicit finite difference method, which has been employed for phase change problems by various authors [8,15,29]. In cases where convective flows within the liquid phase can be neglected enthalpy methods are commonly used in combination with a fixed grid [26]. One such method - the source term method - was identified as a suitable approach for modeling the phase change processes discussed in this thesis. The numerical scheme employed to solve the phase change problems addressed in the case studies is based on this method and is outlined in the following chapter.

3 An implicit finite difference scheme for solid-liquid phase change problems

In this chapter, the numerical scheme used for simulating the phase change processes encountered in the systems that were investigated in the case studies is presented. This scheme was originally developed by Voller & Swaminathan [30] to simulate the solidification in binary alloys. Their approach is based on the source term method discussed in section 2.5.2 and employs the implicit finite difference method outlined in section 2.5.1. It was adopted for this work and implemented as an executable script in MATLAB R2021b. The implemented algorithm was validated using simple test cases, for which analytical solutions were presented in section 2.4.

3.1 Description of the numerical scheme

As mentioned above, the numerical scheme employed in this work is based on the source term method, Eq. (2.66), while using the implicit FDM for discretization. Voller & Swaminathan [30] developed this scheme for solidification problems in binary alloys, which exhibit liquid fraction-temperature relationships such as the ones shown in Figure 2-12. While in this work only linear $\gamma(T)$ curves were used, the outlined scheme should prove capable of solving problems involving more complex relationships as well.

Applying the implicit finite difference method to Eq. (2.66) yields:

$$c_{vol}\frac{T_n^{j+1}-T_n^j}{\Delta t}=\frac{(\lambda_{n+1}+\lambda_n)T_{n+1}^{j+1}}{2\Delta x^2}-\frac{(\lambda_{n+1}+2\lambda_n+\lambda_{n-1})T_n^{j+1}}{2\Delta x^2}+\frac{(\lambda_n+\lambda_{n-1})T_{n-1}^{j+1}}{2\Delta x^2}-\rho_l L\frac{\gamma_n^{j+1}-\gamma_n^j}{\Delta t} \tag{3.1}$$

Applying the same method to Eq. (2.70) yields (see also Appendix A1):

$$c_{vol}\frac{T_n^{j+1}-T_n^j}{\Delta t}=\frac{(\lambda_{n+1}+\lambda_n)(r_{n+1}+r_n)^2}{8\Delta r^2 r_n^2}T_{n+1}^{j+1} - \frac{(\lambda_{n+1}+\lambda_n)(r_{n+1}+r_n)^2+(\lambda_n+\lambda_{n-1})(r_n+r_{n-1})^2}{8\Delta r^2 r_n^2}T_n^{j+1} + \frac{(\lambda_n+\lambda_{n-1})(r_n+r_{n-1})^2}{8\Delta r^2 r_n^2}T_{n-1}^{j+1} - \rho_l L\frac{\gamma_n^{j+1}-\gamma_n^j}{\Delta t} \tag{3.2}$$

Since equations (3.1) and (3.2) contain two unknown quantities that need to be evaluated at the future time step, T_n^{j+1} and γ_n^{j+1}, an iterative procedure is required. Using a common notation for iterative schemes (e.g., see [8,20]), with m as the current iteration, Eq. (3.1) can be written as:

$$\left(\sum_{nb} a_{nb}^m + b_n^m\right)T_n^{m+1} = \sum_{nb} a_{nb}^m T_{nb}^{m+1} + b_n^{old}T_n^{old} + \rho_l L(\gamma_n^{old}-\gamma_n^m) \tag{3.3}$$

with:

$$\sum_{nb} a_{nb}^m = a_{rs,n} + a_{ls,n} = \frac{\Delta t(\lambda_{n+1}^m+\lambda_n^m)}{2\Delta x^2} + \frac{\Delta t(\lambda_n^m+\lambda_{n-1}^m)}{2\Delta x^2} \tag{3.4}$$

$$b_n^m = c_{vol}^m = (1-\gamma_n^m)\rho_s c_{p,s} + \gamma_n^m \rho_l c_{p,l} \tag{3.5}$$

$$\sum_{nb} a_{nb}^m T_{nb}^{m+1} = a_{rs}T_{n+1}^{m+1} + a_{ls}T_{n-1}^{m+1} \tag{3.6}$$

For spherical coordinates, the coefficients a_{rs} and a_{ls} are:

$$a_{rs,n} = \Delta t\left(\frac{(\lambda_{n+1}+\lambda_n)(r_{n+1}+r_n)^2}{8\Delta r^2 r_n^2}\right) \tag{3.7}$$

$$a_{ls,n} = \Delta t\left(\frac{(\lambda_n+\lambda_{n-1})(r_n+r_{n-1})^2}{8\Delta r^2 r_n^2}\right) \tag{3.8}$$

Eq. (3.3) contains only one unknown quantity – the sought future temperature profile T^{m+1}. At the start of the iteration procedure, $\gamma^{m=0}$ and $T^{m=0}$ are set to the values of the previous time step γ^{old} and T^{old}. Next, the linear equation system represented by Eq. (3.3) is solved. However, the new temperature profile is not consistent with the liquid fraction field, since T^{m+1} was calculated from γ^m. This inconsistency can be overcome by applying a liquid fraction update after calculating T^{m+1}:

$$\gamma_n^{m+1} = \gamma_n^m + \omega\Psi \tag{3.9}$$

where ω denotes a relaxation factor and Ψ denotes a correction term. Depending on the nature of the correction, γ_n^{m+1} can be greater than one or smaller than zero. Since the true liquid fraction can only take values between one (fully liquid) and zero (fully solid), an over-/undershoot correction is applied, to make sure that γ_n^{m+1} remains within its physically meaningful bounds:

$$\gamma_n^{m+1} = \begin{cases} 0 & if \quad \gamma_n^{m+1} < 0 \\ 1 & if \quad \gamma_n^{m+1} > 1 \end{cases} \tag{3.10}$$

At the end of an iteration step, the thermal properties are recalculated, and convergence is checked by comparing the enthalpy fields of the current and the previous iteration:

$$\max\left(\frac{|H^{m+1} - H^m|}{H^m}\right) < 10^{-6} \tag{3.11}$$

In case convergence is achieved, T^{m+1} represents the new temperature field of the time step $j + 1$.

An important choice is the selection of the correction term Ψ during the liquid fraction update. In their study, Voller & Swaminathan [30] list and compare different corrections for both linear and non-linear $\gamma(T)$ relationships. A simple yet effective approach is to directly use the known $\gamma(T)$ curve for the update, which for a linear relationship becomes:

$$\Psi = \frac{T_n^{m+1} - T_s}{T_l - T_s} - \gamma_n^m \tag{3.12}$$

However, the direct correction only works for smooth curves without discontinuities and with substantial underrelaxation (ω < 0.001). To overcome this limitation, Voller & Swaminathan [30] suggest using the γ-value at iteration $m + 1$ in Eq. (3.3), resulting in:

$$\left(\sum_{nb} a_{nb}^m + b_n^m\right) T_n^{m+1} = \sum_{nb} a_{nb}^m T_{nb}^{m+1} + b_n^{old} T_n^{old} + \rho_l L(\gamma_n^{old} - \gamma_n^{m+1}) \tag{3.13}$$

With this substitution, a new non-linearity arises as T_n^{m+1} and γ_n^{m+1} are both unknown. As shown by Voller & Swaminathan [30], γ_n^{m+1} can be approximated through Taylor series expansion as:

$$\gamma_n^{m+1} = \gamma_n^m + \left.\frac{d\gamma}{dT}\right|_n^m (T_n^{m+1} - T_n^m) \tag{3.14}$$

In [32], Voller & Prakash recommend using the inverse of $\gamma(T)$ to express T_n^m in Eq. (3.14), i.e., $T_n^m = \gamma^{-1}(\gamma_n^m) = T(\gamma_n^m)$. The reason for this is that in cases of isothermal phase change or when the $\gamma(T)$-curve contains jump discontinuities (as seen in curves 2 and 5 in Figure 2-12), the liquid fraction can become multivalued (e.g., at the fusion temperature). By expressing the temperature as a function of the liquid fraction, i.e., using the inverse $T(\gamma)$, the temperature is always well-defined [32].

Using this recommendation and inserting Eq. (3.14) into Eq. (3.13) yields:

$$\left(\sum_{nb} a_{nb}^{m} + b_n^m + \rho_l L \left.\frac{d\gamma}{dT}\right|_n^m\right) T_n^{m+1} = \sum_{nb} a_{nb}^{m} T_{nb}^{m+1} + b_n^{old} T_n^{old} + \rho_l L(\gamma_n^{old} - \gamma_n^m) + \rho_l L \left.\frac{d\gamma}{dT}\right|_n^m T(\gamma_n^m) \tag{3.15}$$

Eq. (3.15) requires the evaluation of the slope of the liquid fraction curve $\frac{d\gamma}{dT}$ during phase change (i.e., for $0 < \gamma_n^m < 1$). If no phase change is currently taking place (i.e., for $\gamma_n^m = 0$ or $\gamma_n^m = 1$), $\frac{d\gamma}{dT}$ becomes 0.

After the temperature profile T^{m+1} is calculated, the according liquid fraction correction follows from Eq. (3.14):

$$\Psi = \left.\frac{d\gamma}{dT}\right|_n^m \left(T_n^{m+1} - T(\gamma_n^m)\right) \tag{3.16}$$

In order to enhance convergence, Swaminathan & Voller [33] suggest applying Eq. (3.16) only to nodes which undergo phase change, i.e., for $0 < \gamma_n^m < 1$. For nodes which are fully solid or liquid, they suggest the following update in order to allow for the phase change to be initiated (i.e., to avoid skipping the phase change during a time step):

$$\Psi = \frac{c_{p,l}}{L}\left(T_n^{m+1} - T(\gamma_n^m)\right) \tag{3.17}$$

A schematic of the iteration procedure during a time step is shown in Figure 3-1 and can be summarized as follows:

1. The initial values for temperature and liquid fraction for $m = 0$ are set to the values of the old time step.
2. The linear equation system, Eq. (3.15) is solved for the temperature profile T^{m+1} with $\frac{d\gamma}{dT}$ set to 0, if $\gamma_n^m = 0$ or $\gamma_n^m = 1$.
3. From the predicted temperature profile T^{m+1}, the liquid fraction can be determined by Eq. (3.9) and, depending on the state of the material, Eq. (3.16) or (3.17).
4. The over-/undershoot correction for the liquid fraction, Eq. (3.10), is applied.
5. The thermal properties λ and c_{vol} are updated from equations (2.67) and (2.68).
6. Steps 2 through 5 are repeated until convergence is reached, which is the case when the enthalpy fields of two consecutive iterations are consistent within a threshold of 10^{-6} (checked via Eq. (3.11)). Once convergence is achieved, the algorithm proceeds to the next time step.

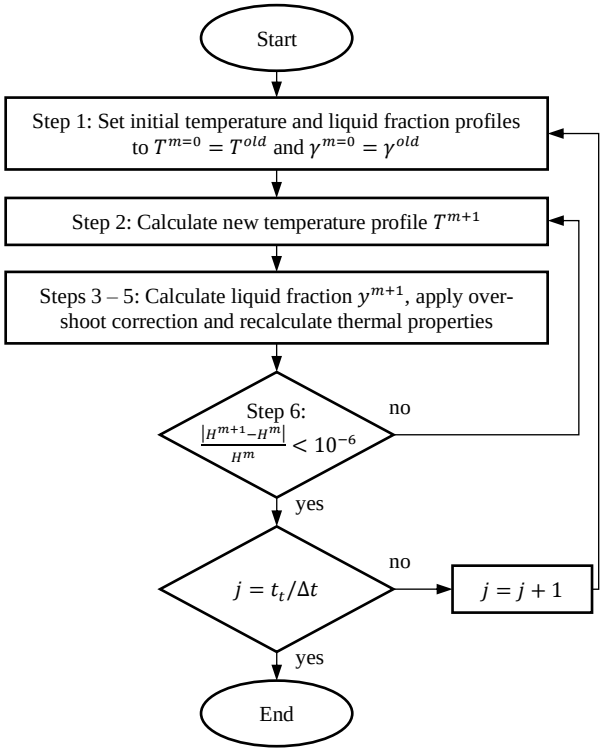

Figure 3-1: Schematic flow chart of the iterative scheme

3.2 Implementation

The outlined algorithm was implemented as an executable script in MATLAB R2021b. To be able to use the linear equation system solver provided by MATLAB, Eq. (3.15) was rewritten in matrix form:

$$\boldsymbol{M}\vec{T} = \vec{d} \tag{3.18}$$

where $\boldsymbol{M}$ is a coefficient matrix, $\vec{T}$ is a vector containing the sought temperature values at $m+1$ and $\vec{d}$ is a column vector containing the remaining terms that are not multiplied with T^{m+1}. The coefficient matrix is a tridiagonal matrix with the following structure:

$$\boldsymbol{M} = \begin{pmatrix} M_{1,1} & M_{1,2} & 0 & & \cdots & & 0 \\ M_{2,1} & M_{2,2} & M_{2,3} & 0 & & \ddots & \\ 0 & \ddots & \ddots & \ddots & 0 & & \vdots \\ & 0 & M_{n,n-1} & M_{n,n} & M_{n,n+1} & 0 & \\ \vdots & & 0 & \ddots & \ddots & \ddots & 0 \\ & \ddots & & 0 & M_{N-1,N-2} & M_{N-1,N-1} & M_{N-1,N} \\ 0 & & \cdots & & 0 & M_{N,N-1} & M_{N,N} \end{pmatrix} \tag{3.19}$$

The diagonal elements of $\boldsymbol{M}$ are:

$$M_{n,n} = \sum\nolimits_{nb} a_{nb}^m + b_n^m + \rho_l L \left.\frac{d\gamma}{dT}\right|_n^m \tag{3.20}$$

$$M_{n,n-1} = -a_{ls,n} \tag{3.21}$$

$$M_{n,n+1} = -a_{rs,n} \tag{3.22}$$

where the indices $n-1$ and $n+1$ refer to the preceding and the next spatial node n, respectively.

The column vector $\vec{d}$ has the following form:

$$\vec{d} = \begin{pmatrix} d_1 \\ d_2 \\ \vdots \\ d_n \\ \vdots \\ d_{N-1} \\ d_N \end{pmatrix} \tag{3.23}$$

with

$$d_n = b_n^{old} T_n^{old} + \rho_l L(\gamma_n^{old} - \gamma_n^m) + \rho_l L \left.\frac{d\gamma}{dT}\right|_n^m T(\gamma_n^m) \tag{3.24}$$

Depending on the boundary conditions, the entries in the first row become:

$$M_{1,1} = b_1^m \tag{3.25}$$

$$M_{1,2} = 0 \tag{3.26}$$

$$d_1 = b_1^{old} T_{w,n=1} \tag{3.27}$$

for Dirichlet boundary conditions,

$$M_{1,1} = 2a_{rs,1} + b_1^m + \rho_l L \left.\frac{d\gamma}{dT}\right|_1^m \tag{3.28}$$

$$M_{1,2} = -2a_{rs,1} \tag{3.29}$$

$$d_1 = b_1^{old} T_1^{old} + \rho_l L\left(\gamma_1^{old} - \gamma_1^m\right) + \rho_l L \left.\frac{d\gamma}{dT}\right|_1^m T(\gamma_1^m) + 2\frac{\Delta t}{\Delta \zeta} \dot{q}_{w,n=1} \tag{3.30}$$

for Neumann boundary conditions, or

$$M_{1,1} = 2a_{rs,1} + b_1^m + \rho_l L \left.\frac{d\gamma}{dT}\right|_1^m + 2\frac{\Delta t}{\Delta \zeta} h_{n=1} \tag{3.31}$$

$$M_{1,2} = -2a_{rs,1} \tag{3.32}$$

$$d_1 = b_1^{old} T_1^{old} + \rho_l L\left(\gamma_1^{old} - \gamma_1^m\right) + \rho_l L \left.\frac{d\gamma}{dT}\right|_1^m T(\gamma_1^m) + 2\frac{\Delta t}{\Delta \zeta} h_{n=1} T_{amb,n=1} \tag{3.33}$$

for Robin and linearized radiative boundary conditions. The spatial discrete $\Delta\zeta$ becomes Δx for Cartesian coordinates or Δr for spherical coordinates. The entries for the last row become:

$$M_{N,N} = b_N^m \tag{3.34}$$

$$M_{N,N-1} = 0 \tag{3.35}$$

$$d_N = b_N^{old} T_{w,n=N} \tag{3.36}$$

for Dirichlet boundary conditions,

$$M_{N,N} = 2a_{ls,N} + b_N^m + \rho_l L \left.\frac{d\gamma}{dT}\right|_N^m \tag{3.37}$$

$$M_{N,N-1} = -2a_{ls,N} \tag{3.38}$$

$$d_N = b_N^{old} T_N^{old} + \rho_l L\left(\gamma_N^{old} - \gamma_N^m\right) + \rho_l L \left.\frac{d\gamma}{dT}\right|_N^m T(\gamma_N^m) + 2\frac{\Delta t}{\Delta\zeta}\dot{q}_{w,n=N} \tag{3.39}$$

for Neumann boundary conditions, or

$$M_{N,N} = 2a_{ls,N} + b_N^m + \rho_l L \left.\frac{d\gamma}{dT}\right|_N^m + 2\frac{\Delta t}{\Delta\zeta} h_{n=N} \tag{3.40}$$

$$M_{N,N-1} = -2a_{ls,N} \tag{3.41}$$

$$d_N = b_N^{old} T_N^{old} + \rho_l L\left(\gamma_N^{old} - \gamma_N^m\right) + \rho_l L \left.\frac{d\gamma}{dT}\right|_N^m T(\gamma_N^m) + 2\frac{\Delta t}{\Delta\zeta} h_{n=N} T_{amb,n=N} \tag{3.42}$$

for Robin and linearized radiative boundary conditions.

Eq. (3.18) can efficiently be solved using the built-in MATLAB-function “mldivide”, which, based on the structure of the coefficient matrix, selects a suitable solution method. Since $\boldsymbol{M}$ is a tridiagonal matrix, the selected solution method is the tridiagonal matrix algorithm, also known as Thomas algorithm.

The implemented iterative algorithm proved to be efficient and versatile, as it can be used for various liquid fraction curves some of which are shown in Figure 2-12, including non-linear functions and curves describing the phase change of a eutectic (combination of linear and power law relation). Further, little to no underrelaxation is required, which significantly speeds up convergence compared to other approaches, such as the one based on Eq. (3.12) or algorithms using the apparent heat capacity method [29].

3.3 Validation test cases for simple geometries

The implemented algorithm outlined in the previous two sections was applied to two simple test cases. The numerical results were compared to the respective analytical solutions

for validation. First, a simple one-dimensional slab is considered that is cooled from one side and insulated on the other. The simulation results were validated against the analytical solution of the Stefan problem given in section 2.4.2. The second test case consists of a one-dimensional spherical PCM capsule that is heated from the outside. As no exact analytical solution exists for this case, the simulation results were compared to the quasi-stationary approximate solutions discussed in section 2.4.3.

3.3.1 Solidification of a one-dimensional slab

The problem considered as a first simple test case was a Stefan problem, as discussed in section 2.4.1. The Neumann solution given in section 2.4.2 served as the basis for validation. The problem data is given in Table 3-1. The PCM used in the case studies was a generic one with properties typical for a paraffin-based material, excluding effects such as subcooling and temperature-dependent variations in material properties.

For the first test case, the solidification of an insulated, one-dimensional slab consisting of PCM with a solidification temperature of 60 °C was considered. The length of the domain was 10 mm, and the simulated time was 300 s. The numerical Fourier number was set to Fo_{num} = 5, resulting in a time step of 0.0163 s for a spatial step of 0.02 mm.

The algorithm outlined in the previous chapters was mainly developed for non-isothermal phase changes, however, the Neumann solution to the Stefan problem is only applicable to isothermal phase changes. A way to also address isothermal phase changes is to ensure that the derivative $\frac{d\gamma}{dT}$ has a very large value, which can be achieved by confining the phase change temperature interval to a very small difference between the solidus and the liquidus temperature, while applying a linear $\gamma(T)$-relationship. Therefore, the difference between the solidus and liquidus temperature was set to 0.002 K for all simulated test cases (accordingly, the solidus and liquidus temperature were 59.999 °C and 60.001 °C, respectively). Further, the initialization temperature was set to 60.002 °C, close to the solidification temperature, in order to resemble the initial condition of the Stefan problem considered by Neumann.

Table 3-1: Test case data for the one-dimensional solidification of a PCM slab

Property	Value
Domain length	10 mm
Spatial discrete	0.02 mm
Time	300 s
Numerical Fourier number	5
Initial temperature	60.002 °C
Wall temperature	50 °C
Phase change temperature	60 °C
Density	814 kg/m³
Heat capacity	2000 J/(kgK)
Thermal conductivity	0.2 W/(mK)
Latent heat	218000 J/kg

As shown in Figure 3-2, the simulation results and the analytical solution are in good agreement. Especially the simulated temperature field corresponds well to that determined by the analytical solution. Regarding the liquid fraction, the simulated phase front advances slightly faster than the analytical one.

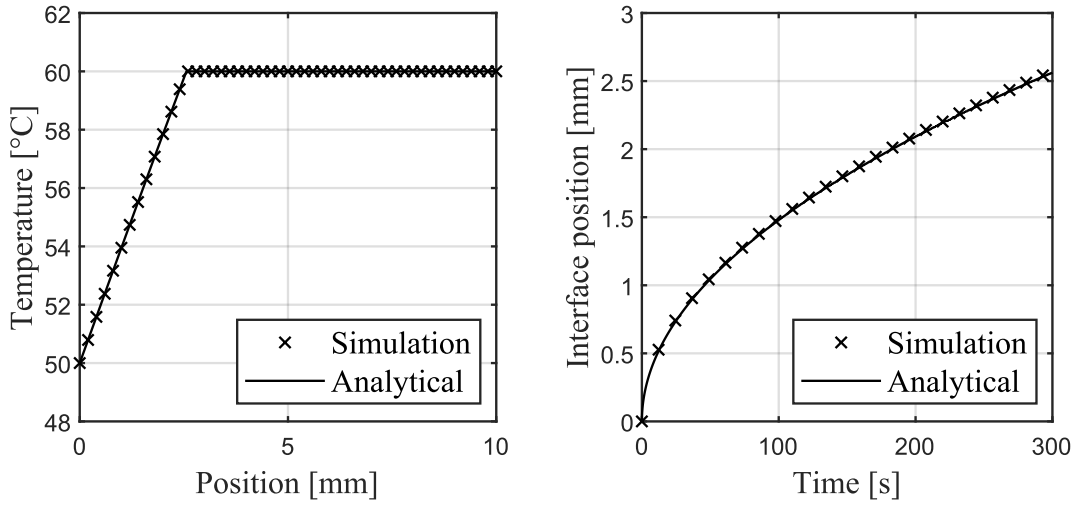

Figure 3-2: Temperature field after 300 s (left) and spatial evolution of the phase front (right) for the solidification of a one-dimensional slab

In order to quantify the deviation between the analytical solution and the simulated results, the mean absolute error MAE was used:

$$MAE = \frac{1}{p}\sum_{i=1}^{p}\left|\hat{Y}_i - Y_i\right| \tag{3.43}$$

Here, $\hat{Y}$ denotes the actual (analytical) value and Y the corresponding predicted (simulated) value, while p is the total number of value pairs. Additionally, to evaluate the relative accuracy, the relative mean absolute error $RMAE$ was used:

$$RMAE = \frac{MAE}{\Delta Y} \cdot 100\% \tag{3.44}$$

where ΔY is a value range that is characteristic for the specific problem. For the test cases discussed here, it was taken as the total length of the domain and the maximum occurring temperature difference, i.e., the difference between the initial and the wall temperature.

The error values determined for the temperature and for the interface location were 0.0012 K (0.012 %) and 0.0099 mm (0.099 %), respectively, indicating very high accuracy. Even when using a coarser spatial discretization of 0.2 mm (which led to a time step of 1.63 s for Fo_{num} = 5) these values remained relatively low, with 0.022 K (0.22 %) and 0.102·mm (1.017 %). These results show that the implemented algorithm performs well for the simple 1D slab test case under isothermal phase change conditions.

3.3.2 Inward melting of a sphere

For the second test case, the convection-driven inward melting of a PCM sphere was considered. The approximate solution used for the validation is given in section 2.4.3, while Figure 2-7, left, shows an illustration of the problem. The same PCM as in the previous test case was used (see Table 3-1). The remaining additional problem data is given in Table 3-2.

Table 3-2: Test case data for the one-dimensional melting of a PCM sphere

Property	Value
Domain radius	5 mm
Spatial step	0.02 mm
Time	5200 s
Numerical Fourier number	15
Initial temperature	59.998 °C
Ambient temperature	61 °C
Heat transfer coefficient	200 W/(m²K)

The radius of the sphere was 5 mm, and the spatial discrete was chosen as 0.02 mm. Due to a longer simulated time, the numerical Fourier number was set to Fo_{num} = 15 enabling a larger time step of 0.049 s compared to 0.0163 s in the previous case study.

As described in section 2.4.3, the approximate solution should only be applied for problems in which the Stefan number is small ($1/St > 7$). With the problem data given in Table 3-2, $1/St = 108.8$, indicating that the approximate solution should be quite accurate and a good basis for the validation of the numerical results.

Figure 3-3 shows the temperature field at different times and the temporal evolution of the phase front. The simulation results and approximate solutions show a qualitatively good agreement. The error values for the temperature were 0.0017 K (0.166 %), 0.0026 K (0.262 %), and 0.0053 K (0.526 %) after ¼, ½ and ¾ of the simulated time. The error values for the interface position were 0.058 mm (0.012 %). These results indicate that the implemented algorithm can also be applied for spherical geometries.

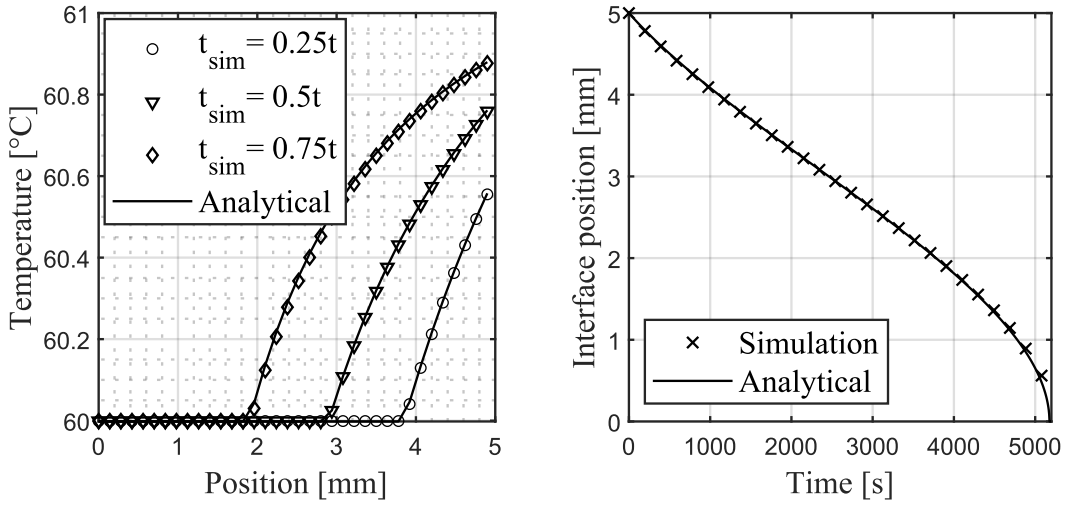

Figure 3-3: Temperature field after ¼, ½ and ¾ of the simulated time t (left) and spatial evolution of the phase front (right) for the inward melting of a sphere

A variation of this test case involving an encapsulated PCM sphere, as shown in Figure 2-7, right, was also investigated. In this case, equations (2.37) - (2.39) were used for comparison. The properties of the encapsulation, which consisted of HDPE, are given in Table 3-3. The capsule thickness was 1 mm, meaning that the radius of the PCM sphere inside the encapsulation was 4 mm.

Table 3-3: Properties of the encapsulation material for the spherical PCM object

Property	Value
Capsule thickness	1 mm
Capsule density	935 kg/m³
Capsule heat capacity	2210 J/(kgK)
Capsule conductivity	0.37 W/(mK)

The simulation results for the melting of PCM inside a spherical capsule are in good agreement with the approximate solution, as shown in Figure 3-4. The error values for the position of the phase front amount to 0.053 mm (0.011 %).

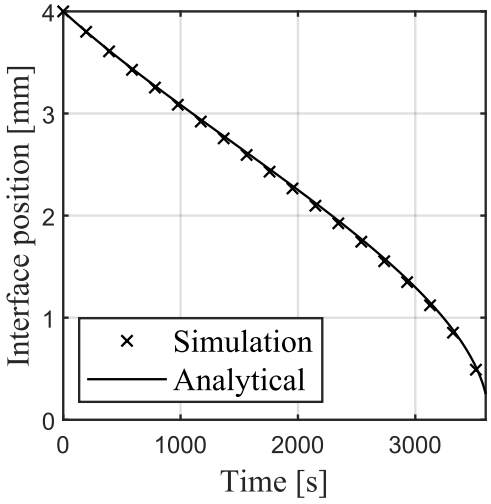

Figure 3-4: Temporal evolution of the phase front during a melting process inside a spherical capsule filled with PCM

The test case results presented above show that the numerical algorithm introduced in section 3.1 can be applied to geometries described both in Cartesian and spherical coordinates, to both melting and solidification problems as well as to problems involving multiple material layers, such as the phase change of PCM encapsulated in another material.

3.4 Summary and conclusion

In this chapter, the numerical solution algorithm for phase change problems developed by Voller & Swaminathan [30] and employed in this work was detailed. The implementation within MATLAB R2021b was described and the applicability to simple test cases was demonstrated.

The governing equations describing the conduction-driven phase change processes in Cartesian and spherical coordinates were discretized using the implicit finite difference method outlined in the previous chapter. The discretized equations were formulated in matrix form and implemented as an iterative scheme within MATLAB. The implemented iterative algorithm was applied to two simple test cases: the solidification of an insulated one-dimensional PCM slab cooled from one side, and the melting of a one-dimensional PCM sphere heated by convection from the ambient. For the first test case, the simulation results were validated against the Neumann solution of the Stefan problem discussed in section 2.4.2. For the second test case, the approximate solutions described in section 2.4.3 were used for validation. In both cases, the algorithm produced excellent results with a mean absolute temperature error of 0.02 K (0.22 %) or less and a mean absolute interface position error of 0.102 mm (1.02 %) or less. These results indicate that the algorithm is applicable to the phase change problems discussed in the case studies presented in Chapters 4 and 5.

4 Case study I: PCM-enhanced solar PV modules

In the first case study, the implemented algorithm for phase change processes was applied to a problem of passive cooling of photovoltaic modules by PCM. An introduction to solar PV is given and the composition of PV modules is briefly described. Current approaches to PV cooling through PCM and the modeling of such PV-PCM systems are discussed. Based on this discussion, the scope of the case study is formulated. A description of the experimental setup installed by the Electrical Energy Technology department at the Paderborn University PV laboratory, shown in Figure 4-1, is given. The thermal model for PCM-enhanced PV modules is presented and the validation based on experimental data is discussed. Additionally, a method to estimate the degradation of PV modules due to thermal fatigue is introduced. The results of a parameter study performed using the validated thermal model are described, and the impact of different PCM heat sink configurations on the efficiency and lifetime of PV modules is evaluated.

Figure 4-1: PV laboratory at Paderborn University (photo: Stefan Krauter, Paderborn University, Department of Electrical Energy Technology)

4.1 State of the art

According to the “Net Zero Emissions by 2050” scenario defined by the International Energy Agency, a 26 % annual growth in solar PV capacity is necessary until 2030 to achieve net-zero greenhouse gas emissions by 2050 – a requirement to limit the average global temperature increase to no more than 1.5 K [34]. Along with installing new solar PV capacity, increasing the efficiency of converting sunlight to electricity in solar cells is a crucial step to achieve this goal. Promising new technologies, such as tandem perovskite solar cells, which utilize additional ranges of the light spectrum, can yield conversion efficiencies of more than 30 % on a lab scale [35]. However, most commercially available solar PV modules based on mono- and poly-crystalline cells exhibit conversion efficiencies between 15 to 24 % [36].

Along with the architecture of the cell and the underlying technology, the conversion efficiency of a PV module also depends on its operating conditions. A high cell temperature in particular has a negative effect on efficiency, which has led to the development of approaches to cool the PV modules during operation using active or passive measures. An example of an active cooling method is the installment of pipes, which distribute a water film onto the surface of the PV module. Another method is active cooling with fans. Such methods are reported to increase the PV module conversion efficiency by more than 50 %, however at high investment and maintenance cost [37]. Passive cooling methods such as fins or air channels inducing natural convection on the back side of the module offer less expensive and low-maintenance solutions to effectively increase the module efficiency. The cooling approach investigated in this case study was to install PCM at the back side of the module. The PCM serves as a heat sink aiming to reduce and stabilize the operating temperature of the solar cells.

4.1.1 Structure and composition of PV modules

Conventional PV modules consist of different material layers that are fixed in a metal frame. The usual setup comprises protective covers at the front (glass) and the back (different polymers), which enclose the solar cells in between. Ethylene-vinyl acetate (EVA) is typically used as adhesive and encapsulation material joining together the individual layers. The structure of a typical solar module is given in Figure 4-2.

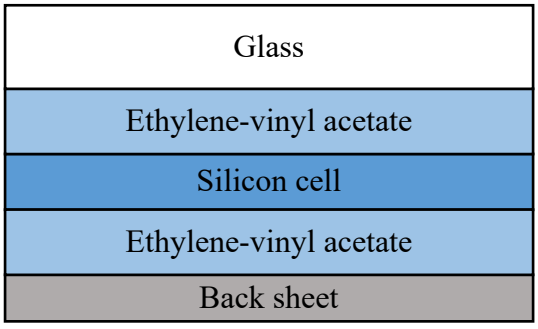

Figure 4-2: Layered structure of a typical PV module

The glass cover typically has a thickness of 3 to 4 mm and protects the cells from water and airborne solid particles like hail and dust. It is usually tempered, highly transmissive and has a low iron content increasing its transparency.

The EVA film is a transparent layer, which is used in the production process (i.e., lamination) to fix the cells. It further increases the module stability and enhances the protection against moisture.

The back sheet is made of polymers, such as polypropylene, polyethylene terephthalate or polyvinyl fluoride. It serves as a protection against moisture and acts as an electrical insulator. It further increases the mechanical stability of the module and is typically of white color.

The metal frame holds together the individual components of the module and provides additional stability. It is usually made of aluminum and therefore light in weight yet still durable against external loads caused by wind or hail.

The solar cells convert solar irradiation into electrical power by utilizing the photoelectric effect. They are made of thin silicon wafers, which are either polycrystalline or monocrystalline. While some of the incoming sunlight is converted to electrical power, the major part is converted to non-usable heat, which increases the temperature of the solar cell reducing its efficiency. Also, temperature fluctuations cause thermal stress within the layer structure leading to the degradation of the module layers and of the interconnectors that electrically connect the individual solar cells.

Since the focus of this case study laid on the thermal modeling of solar PV modules, the electrical phenomena occurring inside a solar cell are not considered further. Corresponding information can be found in, e.g., [38,39].

4.1.2 PV-PCM modules

As mentioned above, the efficiency of PV modules depends on the operating temperature of the solar cells. Promising passive cooling approaches include the use of PCM, which is usually only attached to the backside of the module due to the low transparency of most PCM in their solid state. One of the first groups to study PV-PCM modules was Huang et al. [40], who attached a heat sink containing PCM and aluminum fins for better heat transfer to building-integrated solar PV modules. They used experiments for the validation of their finite-volume simulations and studied different heat sink dimensions, e.g., the thickness, which varied between 20 and 50 mm. They found that the use of the PCM heat sink can significantly stabilize the operating temperature of the PV module and hence its efficiency. Since most PCM have a low thermal conductivity, the addition of fins was necessary in that study. An approach addressing the low conductivity was reported by Japs et al. [41], who aimed to increase it by adding graphite to the PCM. Their experimental results showed that the composite PCM-graphite heat sink leads to fewer and lower temperature fluctuations, but at the expense of efficiency caused by the insulating effect of the liquid PCM. This insulating effect resulted in higher operating temperatures compared to a reference module without PCM. However, their choice of PCM was not

optimal as it had a rather low melting point of around 28 °C. As the cell temperatures can easily reach up to 50 - 60 °C on hot summer days, such low phase change temperatures cause the PCM to melt quite earlier at around 11:30 am. Conclusions that can be drawn from their study are that the PCM layer was likely too thick and the melting point of the PCM was too low. Another aspect they addressed was the additional economic cost of the PCM. In order to become feasible, the price of PCM would have to drop significantly – an observation that was still being made in more recent studies (e.g., Nižetić et al. [42] and Ali [43]).

An aspect that is not addressed in most reviewed papers is the potential increase in lifetime that results from reduced temperature fluctuations – both in frequency and in amplitude. Fewer and smaller cell temperature fluctuations mean less fatigue, which is caused by temperature changes of the different material layers constrained in the frame that have different coefficients of thermal expansion. This means that the different module layers expand at different rates leading to friction, which in turn can lead to the breakage of the interconnectors – small, thin copper bands connecting the individual solar cells. In fact, a long-term analysis of end-of-life causes for PV modules by Wohlgemuth [44] revealed that up to 40 % of the examined modules failed due to interconnector breakage. Considering that thermal fatigue due to cell temperature fluctuations causes most of these breakages, investigating the potential positive effect of PCM on the module lifetime seemed justified. For this reason, Weber et al. [45] introduced a method to quantify the accumulated damage of PV-PCM modules due to temperature fluctuations. They estimated that the lifetime of PV modules can be increased by up to 30 % through the addition of PCM.

In order to design a PCM heat sink for PV modules that is both cost-efficient and potentially lifetime-extending, a predictive thermal model for the PV-PCM module was used in this study. The thermal modeling of conventional PV systems without PCM has been discussed in detail in literature, and numerous models of varying complexity with the aim of determining the cell temperature can be found. An extensive review of cell temperature correlations was carried out by Skoplaki & Palyvos [46], who categorized them into implicit and explicit ones. The former express the cell temperature through quantities which themselves depend on the cell temperature, e.g., the PV efficiency. Such a correlation was suggested by Mattei et al. [47], who determined the cell temperature using an energy balance. Explicit correlations determine the cell temperature based on the ambient temperature and/or the irradiation, which is often sufficient for many practical applications.

For a more detailed description of the heat transfer process inside the PV module, numerical methods can be applied. These methods vary in their complexity from simpler 1D models based on finite differences which only cover the heat transfer by conduction inside the layered module structure, to CFD-based 3D-simulations such as that of Jaszczur et al. [48], which even considered the air flow around the module. 3D-CFD simulations using commercial software tools are both computationally and economically expensive. Especially if long periods of time (> several hours) must be simulated, 3D-methods are often not feasible.

In contrast, 1D methods based on finite differences offer greater flexibility regarding the simulated time periods and are therefore the focus of this overview on different modeling

approaches. The aim of the reviewed models is to accurately predict the cell temperatures over various time frames, typically ranging from several hours to several days, while accounting for fluctuating weather conditions. Consequently, most authors compare their simulated cell temperature profiles with measured data, quantifying deviations between experimental and simulation results using various error types.

Unfortunately, there is no standard for which error types are to be used and how the error values are to be determined, which makes it difficult to compare the quality of the models. Some authors provide the MAE (see Eq. (3.43)), while some specify the $RMAE$ (see Eq. (3.44)) or other error types such as the maximum error or the root mean square error. Additionally, temperature plots of the measured and simulated data are usually provided. In particular, the use of relative error values is problematic for comparing the accuracy of the various models, as the value used as reference depends on factors such as the time span considered, the prevailing weather conditions, and ultimately the preference of the individual author, and thus varies between studies. Therefore, for the sake of consistency and comparability, the error values given in the following paragraphs refer to the root mean square error $RMSE$. While the MAE represents the average of all deviations, the $RMSE$ gives more weight to larger deviations. It is defined as:

$$RMSE = \sqrt{\frac{1}{p}\sum_{i=1}^{p}\left(\hat{Y}_i - Y_i\right)^2} \tag{4.1}$$

or, in relation to a reference value, as:

$$RRMSE = \frac{RMSE}{\Delta Y} \cdot 100\ \% \tag{4.2}$$

Where available, the $RSME$ is cited directly from the reviewed publication, otherwise the corresponding temperature plots were used to derive the $RMSE$ through plot digitalization.

Before discussing modeling approaches for PV-PCM systems, it is useful to take a closer look at models of conventional PV modules, since the environmental influences of wind and radiation as well as the internal heat transport mechanisms (except for the phase change) are similar in both systems. A 1D model of a PV system without PCM based on the explicit FDM was developed by Jones & Underwood [49]. They used a lumped approach, in which all module layers are reduced to one node and a single energy balance is calculated at each time step. With this approach, they achieved a maximum $RMSE$ of 2.8 K for a measurement period of several hours. Another such lumped model was proposed by Abdulrazzaq et al. [50], who achieved improved accuracy by including an empirical fitting parameter resulting in a maximum $RMSE$ of 1.6 K for a measurement period of one day. A more advanced lumped approach was proposed by Notton et al. [51], who approximated a double-glass module through three spatial nodes (instead of just one) and additionally considered the thermal conduction between them. The layers they included in their model were the front glass, the solar cells and the back glass, while neglecting the EVA. They also studied the effect of different convective heat transfer correlations on the

cell temperature. Employing an explicit 4th order Runge-Kutta method as their solution technique, they reported a maximum $RMSE$ of 1.3 K for a measurement period of eight days. A drawback of the explicit methods employed in [49–51] is the necessity to adhere to the Fo_{num} stability criterion (see Eq. (2.50) in section 2.5.1.1). This requirement limits the time step size, as it depends on the thermal diffusivity of the involved materials and the spatial discretization. To overcome this limitation, Bevilacqua et al. [52] developed a model based on the implicit FDM, which enabled the use of a finer spatial discretization and the inclusion of all relevant module layers shown in Figure 4-2. For their model validation, they considered several days from each season and were able to achieve average $RMSE$ values of 1.4 K, 1.3 K, 1.7 K and 1.5 K for spring, summer, fall and winter.

Regarding PV-PCM systems, modeling approaches similar to those used for conventional PV systems can be found, ranging from lumped approaches to 1D models that fully resolve each individual layer. Lo Brano et al. [53] developed a model of a PV-PCM system based on the explicit FDM, assuming an isothermal phase change in the PCM layer. Due to the stability restrictions associated with the explicit FDM, they modeled the solar cell layer as an infinitesimally thin interface acting as heat source, while separating the top and bottom half of the module. Their simulated results yielded $RMSE$ values of up to 3.2 K when compared to measured data gathered over two days. Another PV-PCM modeling approach based on the explicit FDM was reported by Arıcı et al. [54], who also assumed an isothermal phase change. They employed the source term method (see section 2.5.2) within the PCM layer and compared their numerical results to one day of experimental data from Lo Brano et al. [53], resulting in an $RMSE$ of 3.5 K. Díaz et al. [55] assumed non-isothermal phase change conditions and used an enhanced conduction method to account for natural convection within the liquified PCM. They combined the EVA, solar cell, and backsheet into a single layer, employing an implicit finite volume method with a non-uniform spatial grid. Like Arıcı et al. [54], Díaz et al. [55] did not perform their own measurements but compared their simulation data with the experimental results of Lo Brano et al. [53], yielding an $RMSE$ of 3.8 K. Savvakis & Tsoutsos [56], on the other hand, conducted experiments over a time period of a full year and developed a lumped capacity approach to optimize the PCM layer thickness for varying ambient conditions. Unfortunately, they only provided validation data for a reference system without PCM, for which a $RMSE$ of 4.5 K was determined. In their publication, they highlight the positive effects of PCM on the module lifetime and emphasize the importance of field measurements for validating models and monitoring the reliability of PV-PCM systems.

Comparing the reported accuracy of models developed for PV systems with and without PCM reveals that the inclusion of a PCM layer leads to greater deviations between experimental and simulation data. For conventional PV systems the lowest found $RMSE$ was 1.3 K (Notton et al. [51]), whereas for PV-PCM systems, the lowest $RMSE$ was 3.2 K (Lo Brano et al. [53]). For a better understanding of the relative deviation between experimental and simulation results, the $RRMSE$ can be calculated using the largest observed temperature difference (i.e., maximum daily temperature – minimum daily temperature) as reference value ΔY (see Eq. (4.2)). In the study by Notton et al. [51], this temperature

difference was 40 K yielding an $RRMSE$ of 3.25 %. In the study by Lo Brano et al. [53] this difference was 36 K, resulting in an $RRMSE$ of 8.89 %. This substantial difference in accuracy indicates that further efforts are needed to accurately predict the thermal behavior of PV-PCM systems.

4.2 Scope of the case study

The key findings of the literature reviewed above can be summarized as follows:

- In most experimental studies, the determined gain in PV efficiency was too low compared to the high economic cost of PCM. This might be due to an improper design of the PCM heat sink.
- The PCM heat sink can potentially increase the PV module lifetime. A detailed experimental validation as well as an economic analysis of this aspect are missing.
- The thermal modeling of conventional PV systems is well described in literature and can serve as a basis for a PV-PCM model. Often, several correlations for ambient conditions had to be tested to achieve good agreement with experiments.
- Existing models for PV-PCM systems produce less accurate results compared to models for conventional PV modules. This indicates that the phase change processes within the PCM layer are not captured properly.

Based on these findings, the main goals of this case study were to develop a thermal model of PV-PCM systems that includes all relevant material layers in order to determine the temperature distribution across the entire module. The model accuracy should exceed the values reported in the reviewed literature, with an average $RMSE$ of less than 2 K when validated against experimental data. This data should be gathered from a test site at the Paderborn University PV lab, installed and operated by the Electrical Energy Technology department, which was a partner in a joint research project consortium that included the author of this thesis. Based on these goals, the following tasks were defined:

- Conceptualization and installation of an experimental PV-PCM system at the Paderborn University PV lab (see Figure 4-1) in order to collect measured data over at least one month under varying ambient conditions, in collaboration with the Electrical Energy Technology department
- Development of a thermal model for PV-PCM modules based on the implicit finite difference scheme for phase change processes introduced in Chapter 3
- Variation and testing of different correlations for the convective and the radiative heat transfer coefficients to identify the combination giving the best accuracy
- Application of the model to study different PCM heat sink configurations and to evaluate their impact on the module efficiency and lifetime in a parameter study

These activities are described in detail in the following sections.

4.3 System description and experimental setup

The system investigated was the experimental setup shown in Figure 4-3, which was installed by the Electrical Energy Technology department of Paderborn University at its PV lab as part of a joint research project. The PV lab is located at 51°42'24.9"N & 8°46'16.7"E at a height of 20 m above ground. The setup consisted of three PV modules from the PX230 series by Sunset Solar GmbH, with a rated power of 230 W. Each module contains 60 poly-crystalline solar cells. One of these modules was used as a reference module, while a PCM heat sink designed as a foil was attached to each of the other two modules. Two different foil configurations, which are shown in Figure 4-4 were tested: a smooth, plane PCM foil and a bubble wrap type PCM foil. They consisted of an aluminum layer, the PCM, either in form of a plane layer or individual pins, and an HDPE film.

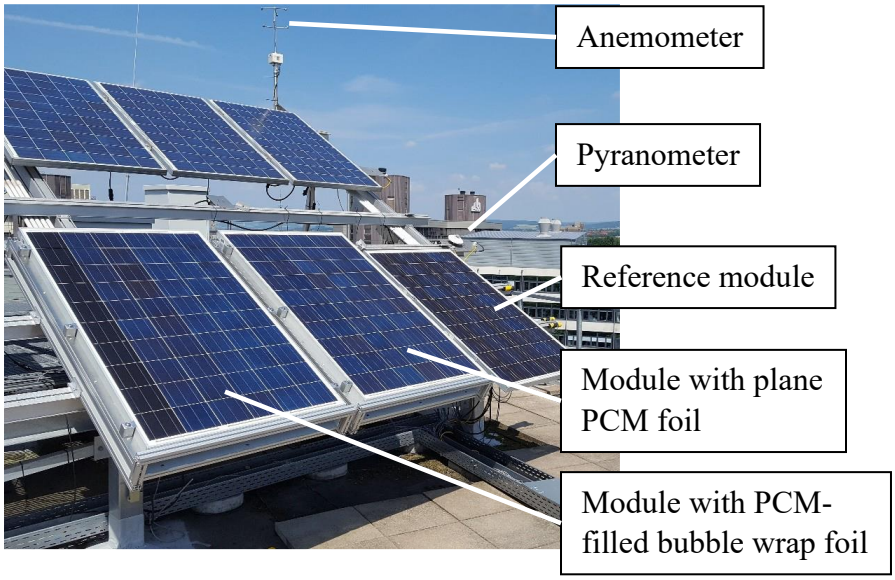

Figure 4-3: Experimental setup at the Paderborn University PV lab with three different module configurations: PV module without PCM as reference, PV-PCM module with plane PCM foil and PV-PCM module with PCM bubble wrap foil

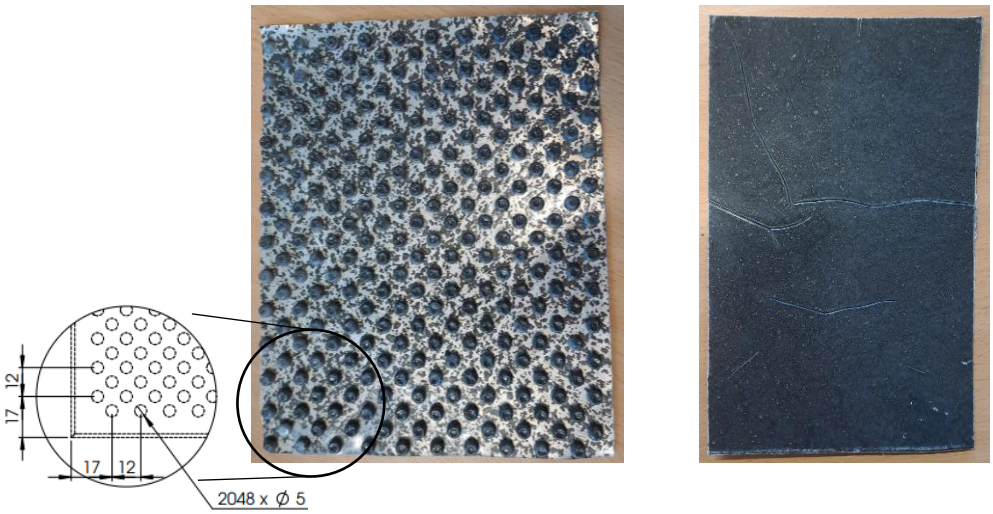

Figure 4-4: Bubble wrap (left) and smooth (right) PCM foils attached to two of the PV modules in the experimental setup

Before adding the PCM foils and installing the modules at the PV lab, all three modules underwent flash tests at Standard Test Conditions (STC). Those conditions are defined as follows: 1000 W/m² irradiance in normal direction of the module plane, an ambient temperature of 25 °C and an air mass coefficient of 1.5 [57]. The flash tests were performed to determine the reference power output and efficiency of the modules. The reference efficiency is defined as the ratio of measured electrical power to irradiance at STC. The flash test results are listed in Table 4-1 and show that the module with the bubble wrap foil has the highest and the smooth foil module the lowest reference efficiency. Another reference parameter is the temperature coefficient, which was determined only for the reference module. This coefficient relates the conversion efficiency to the temperature, and indicates the efficiency decrease with increasing temperatures. The flash tests of the reference module revealed a temperature coefficient of 0.278 %/K.

Table 4-1: Flash test results for PV modules used in the experimental setup

	Reference module	Smooth foil module	Bubble wrap foil module
P_{ref} [W]	231.7	226.0	237.3
η_{ref} [%]	14.06	13.72	14.40

After the flash tests, temperature sensors (PT100) were attached to the back of the modules at the positions indicated in Figure 4-5. In the case of the reference module, they were attached with insulating tape, while they were glued to the backside of the two PV-PCM modules before the PCM foils were attached. In this way, the sensors were all located at the same vertical distance from the PV cells.

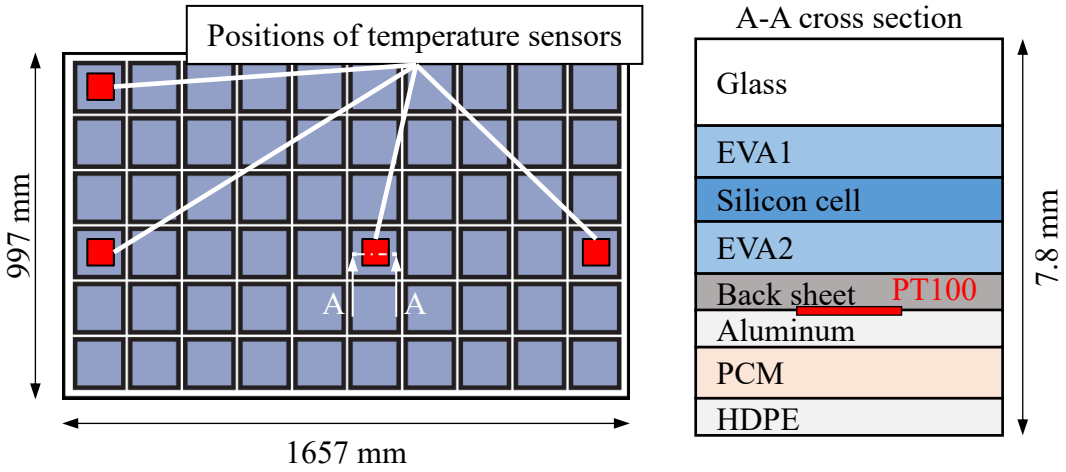

Figure 4-5: Module dimensions and locations of temperatures sensors (PT100) on the back side of each module

Once the temperature sensors and the PCM foils were attached, the modules were installed at the PV lab at an inclination of 30° with respect to the horizontal.

The recorded experimental data included the temperatures of the PT100 elements, wind speed and direction, ambient temperature and solar irradiance. The experimental equipment used for the measurements is listed in Table 4-2.

Table 4-2: Experimental measuring equipment at the experimental setup

Measured quantity	Sensor location	Device	Sampling rate
Module temperature	Module backside	4 x Jumo PT100	10 s
Wind speed and direction	At top of module support structure	Thies 3D-ultrasonic anemometer	5 min
Irradiance	Module plane	Kipp & Zonen CMP21 pyranometer	10 s
Ambient temperature	At lower half of module support structure	Jumo PT100	10 s

The PCM used for the PCM foils was a paraffin-based polymer compound to which graphite particles were added to increase the thermal conductivity, as described by Sonnenrein et al. [58]. The resulting latent heat was 161.4 kJ/kg over a melting range from 35°C to 43°C. The properties of the individual module layers are listed in Table 4-3.

Table 4-3: Material properties of the different PV module layers (last three layers only for the two PV-PCM modules)

Layer		Thickness [mm]	Conductivity [W/(mK)]	Heat capacity [J/(kgK)]	Density [kg/m³]
Solar glass		4	1.8	500	3000
EVA1		0.45	0.35	2090	960
Silicon cell		0.2	148	677	2330
EVA2		0.45	0.35	2090	960
Backsheet		0.35	0.2	1700	1140
Aluminum		0.3	217	865	2700
PCM	liquid	2	0.6	2720	770
	solid		1.1	3150	778
HDPE		0.1	0.42	1900	940

The emissivity, transmittance, and absorptivity of the top layer (glass) were 0.94, 0.91, and 0.02, respectively. The transmittance and absorptivity of the EVA layer were 0.97 and 0.03, respectively, while the emissivity of the bottom layer was 0.94.

4.4 Thermal model of PCM-enhanced PV modules

The thermal model of a PCM-enhanced PV system developed in this work considers the heat transfer inside the layer composition itself, as well as ambient conditions in the form of boundary conditions. An illustration of the considered heat transfer mechanisms and boundary conditions included in the model is shown in Figure 4-6.

The main heat source is the thermal energy influx resulting directly from the incoming solar irradiance. Due to the high transmissivity and low reflection of the glass and the EVA layers, most of the incoming sunlight reaches the solar cell, where a certain part of it is converted into electrical energy. The remaining share of solar energy is directly converted into heat, which then is conducted through the individual layers to the top and bottom surfaces of the module. There, thermal convection and radiation cause heat exchange with the ambient. Within the PCM layer, phase changes occur, which are expected to smoothen the temporal temperature profile. The PCM itself is part of a laminated foil that contains a layer of aluminum for better thermal conduction and vertical temperature distribution. Additionally, a thin HDPE film protects the PCM from leaking.

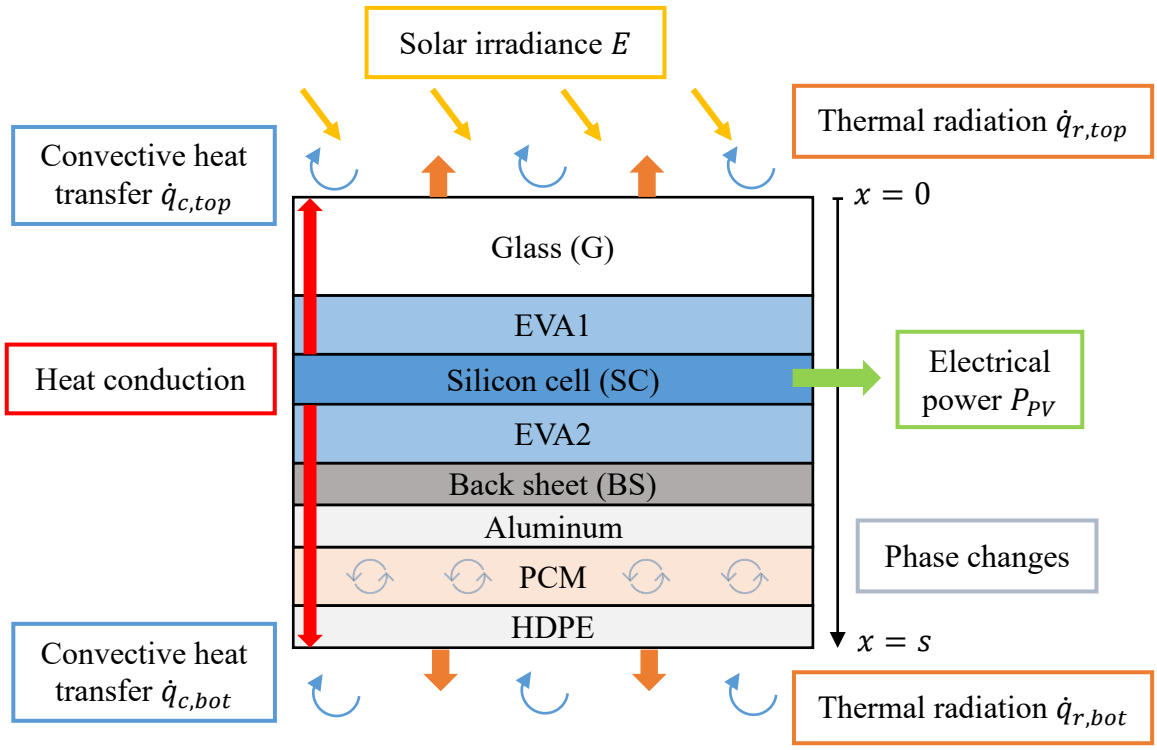

Figure 4-6: Structure of a PCM-enhanced PV module and the heat transfer mechanisms affecting its performance

Neglecting heat conduction through the module frame and assuming a uniform temperature distribution across the module in horizontal direction, a single one-dimensional conduction equation describes the heat transport across the individual layers:

$$\rho c_p \frac{\partial T}{\partial t} = \frac{\partial}{\partial x}\left(k \frac{\partial T}{\partial x}\right) + S \tag{4.3}$$

The material properties ρ, c_p and k differ for each layer but are assumed to be constant within the same material and temperature-independent. The only exception is the PCM layer, for which these properties are determined based on the liquid fraction, which in turn depends on the temperature.

The source term S is individually defined for each layer and accounts for the heat generation by imperfect light transmission within the glass and EVA1 layers, the conversion of irradiance into electrical power as well as the phase change process of the PCM.

4.4.1 Source term

The source term is used for the following layers: glass, EVA1, solar cells and PCM. For the remaining layers it is set to zero. Within the first two layers, some of the solar irradiance E is absorbed and converted into heat. This process is characterized by the absorptivity δ and transmittance τ of the respective materials. Since the glass and EVA layers are almost transparent, most of the incoming sunlight reaches the PV cells. For the glass layer, which has the thickness s_G the source term is defined as:

$$S_G = \delta_G \frac{E}{s_G} \tag{4.4}$$

For the EVA1-layer with the thickness s_{EVA1}, it is:

$$S_{EVA1} = \delta_{EVA1} \tau_G \frac{E}{s_{EVA1}} \tag{4.5}$$

Inside the solar cell of thickness s_{SC}, a part of the incoming sunlight that reaches the surface area of the solar cells A_{SC} is converted into electrical power P_{PV}:

$$S_{SC} = \tau_{EVA1} \tau_G \frac{E}{X_{SC}} - \frac{P_{PV}}{A_{SC} s_{SC}} \tag{4.6}$$

with P_{PV} as:

$$P_{PV} = \eta_{PV} A_{SC} E \tag{4.7}$$

To calculate the electrical power generated by the solar cells, their conversion efficiency η_{PV} needs to be determined. This can be challenging, since the efficiency depends on the cell temperature, which, in turn, is one of the unknown quantities.

Often, the conversion efficiency can simply be assumed as constant or described by correlations. A review of the relationships proposed by different authors was published by Skoplaki & Palyvos [59], in which the authors distinguished between explicit and implicit correlations. For the former, the ambient temperature and, in some cases, the wind speed are used to determine the cell temperature. However, this approach would not be appropriate for the model presented here since these weather-related influences are already covered by boundary conditions, as discussed in the next section. Therefore, an implicit relationship seemed better suited to determine the cell efficiency meaning that it has to

be derived directly from the cell temperature. Such a relationship was developed by Evans & Florschuetz [60] and is given by Eq. (4.8). In addition to the cell temperature, only module-specific parameters are required, which are usually provided by the module manufacturer.

$$\eta_{PV} = \eta_{ref}\left[1 - \beta_{ref}\left(T_{SC} - T_{ref}\right)\right] \tag{4.8}$$

Eq. (4.8) is convenient, since the photovoltaic efficiency η_{PV} only depends on known properties of the actual PV module, i.e., the reference efficiency η_{ref}, the temperature coefficient β_{ref} and the reference temperature T_{ref}. These quantities are determined by the module manufacturers through flash tests under STC.

For the modeling of the phase change processes taking place inside the PCM layer at the back of the module, the source term method discussed in section 2.5.2 (i.e., Eq. (2.66)) was applied.

4.4.2 Initial and boundary conditions

The simulations were initialized assuming a uniform temperature across the whole module. The initial temperature value was taken from the experimental data gathered at the PV lab of Paderborn University. The simulated timespan was usually between 4:00 am and 8:00 pm, which means that the initial temperature was the measured module temperature at 4:00 am.

The heat exchange between the module and its environment was modeled via boundary conditions. These include the convective heat flux $\dot{q}_c$ at the top and bottom surfaces of the module and the radiative heat flux $\dot{q}_r$ between the module and the sky, and the module and the ground, respectively, as indicated in Figure 4-6. The sum of the heat fluxes determines the temperature gradient at the module top and bottom faces:

$$-k\left.\frac{\partial T}{\partial x}\right|_{x=0} = \dot{q}_{c,top} + \dot{q}_{r,top} \tag{4.9}$$

$$k\left.\frac{\partial T}{\partial x}\right|_{x=s} = \dot{q}_{c,bot} + \dot{q}_{r,bot} \tag{4.10}$$

4.4.2.1 Convective heat flux

The convective heat fluxes at the top and bottom side of the module are defined as:

$$\dot{q}_{c,top} = h_{c,top}\left(T_{amb} - T(x=0)\right) \tag{4.11}$$

$$\dot{q}_{c,bot} = h_{c,bot}\left(T_{amb} - T(x=\mathrm{s})\right) \tag{4.12}$$

The convective heat transfer coefficient h_c for solar energy equipment such as PV modules or thermal collectors is difficult to determine as isolating the impact of convection on the heat transfer from other naturally occurring effects like cloud cover, precipitation or dust covering, is not trivial. Therefore, several correlations exist in literature that take

various aspects of the operating and ambient conditions such as wind speed and direction (i.e., windward or leeward), module dimensions or the inclination angle, into account. Often, these correlations give good results only for the corresponding field test site and therefore should be applied with caution. What almost all these correlations have in common, is that they correlate the free stream wind velocity u_f with the heat transfer coefficient, since forced convection by wind is conceivably the most obvious driver for convective heat transfer at solar PV modules.

Palyvos [61] in 2008 published a comprehensive review on correlations for wind-induced convective heat transfer coefficients, which still appears to be the most up-to-date data compendium for such correlations. In his review, he categorized the correlations into linear approaches, power-law approaches, approaches that account for the length of the overflowed plate and approaches that are based on the boundary layer theory. Correlations of the first two categories usually consider both forced and free convection in the resulting value of h_c, which makes them relatively easy to use. The correlations of the third and fourth category are more complex and require additional data such as wind direction, the inclination angle of the module or Reynolds and Prandtl numbers. Furthermore, it is necessary to determine the heat transfer coefficient resulting from free convection, h_{nc}, and to combine it with the forced heat transfer coefficient h_{fc} to receive h_c.

In this work, one correlation from each of the categories mentioned was selected based on their suitability for PV modules. These correlations are given in Table 4-4. The first listed correlation is simply an arithmetic average of about 30 linear correlations that were presented in the review by Palyvos [61] mentioned above. The second correlation by Sharples & Charlesworth [62] was developed for a roof-mounted, inclined solar thermal collector on a field test site. The third correlation by Sartori [63] takes the decay of the heat transfer coefficient along the overflowed surface into account. Since PV modules are usually not square in shape, the length of this surface depends on the wind direction, making the implementation of this correlation more complex. Additionally, an appropriate correlation for natural convection needs to be included as the Sartori [63] correlation only provides the forced convective coefficient. In [63], Sartori formulates one equation for each flow regime – one for laminar, one for transition and one for turbulent flow, but frequently remarks that the regime for wind-induced flow is usually turbulent. Therefore, only Eq (4.15), which is the one for turbulent flow, was used in this case study. Initially, the leeward side was treated similarly to the front side via Eq. (4.15), however, Kaplani & Kaplanis [64] reported that a linear correlation for their experimental setup, which is very similar to the one at the Paderborn University PV lab, gave better agreement with their simulation model. Therefore, it was used for the leeward side in this work as well. The last correlation that was tested was provided by Eicker [65] in her book on solar technologies for buildings. As was the case for the Sartori [63] correlation, the wind direction had to be considered, since the Reynolds number depends on the characteristic length of the overflowed plate. Additionally, Eicker [65] provides a correlation for the heat transfer coefficient in case of natural convection.

Table 4-4: Correlations to determine the convection heat transfer coefficient on the top and bottom sides of PV modules

Equation		Author	Notes
$h_{c,luv} = 7.4 + 4u_f$ $h_{c,lee} = 4.2 + 3.5u_f$	(4.13)	Palyvos [61]	Arithmetic mean of multiple linear correlations
$h_c = 9.4\sqrt{u_f}$	(4.14)	Sharples & Charlesworth [62]	Inclined solar collector dummy
$h_{fc,luv} = 5.74u_f^{0.8}L_{ch}^{-0.2}$	(4.15)	Sartori [63]	Based on boundary layer theory for flat plates
$h_{fc,lee} = 1.5u_f + 3$	(4.16)	Kaplani & Kaplanis [64]	
$Nu_{fc} = \frac{0.037Re^{0.8}Pr}{1 + 2.443Re^{-0.1}\left(Pr^{(2/3)} - 1\right)}$	(4.17)	Eicker [65]	Nusselt correlation for flat plates with turbulent boundary layer
$h_{nc} = 1.78\left(\lvert T_{amb} - T_{top/bot}\rvert\right)^{1/3}$	(4.18)		

Mixed convection

An additional requirement for the use of Eicker's [65] and Sartori's [63] correlations is the determination of the natural convection heat transfer coefficient h_{nc}. Eicker provides a correlation for natural convection in her book, but the application of Sartori's boundary layer approach requires an additional correlation that had to be identified.

Before discussing the natural convection method used with the Sartori correlation, the mixed convection approach by Churchill [66] is presented, which accounts for the combined effect of natural and forced convection:

$$Nu_c = \sqrt[3]{Nu_{fc}^3 + Nu_{nc}^3} = \frac{L_c}{k_{air}}\sqrt[3]{h_{fc}^3 + h_{nc}^3} \tag{4.19}$$

Eq. (4.19) is applicable for situations in which the natural und forced convection follow the same direction. If this is not the case, the difference of both Nusselt numbers should be used [67]:

$$Nu_c = \sqrt[3]{Nu_{fc}^3 - Nu_{nc}^3} = \frac{L_c}{k_{air}}\sqrt[3]{h_{fc}^3 - h_{nc}^3} \tag{4.20}$$

Equations (4.19) and (4.20) have to be applied for both the bottom and top side of the module. The forced convection heat transfer coefficient h_{fc} is determined by Eq. (4.15)/(4.16) or Eq. (4.17). The natural convection heat transfer coefficient h_{nc} can be calculated from Eq. (4.18) or, in case Sartori's h_{fc}-equation is applied, by correlations

for inclined plates, as given in [67]. The inclination is specified by the angle γ_I between the ground and the module, which was 30° for the modules in the experimental setup, as indicated in Figure 4-7.

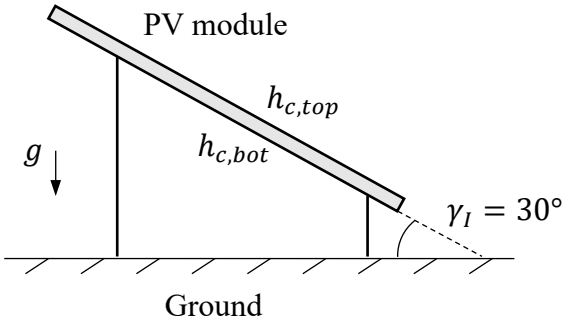

Figure 4-7: Schematic of an inclined PV module

Natural convection

For the top side of the module, the following Nusselt correlation proposed by Fujii & Imura [68] for natural convection on an arbitrarily inclined plate was used:

$$Nu_{nc,top} = 0.13\left(Ra^{1/3} - Ra_{cr}^{1/3}\right) + 0.56(Ra_{cr}\cos(90° - \gamma_I))^{1/4} \tag{4.21}$$

The Rayleigh number Ra describes the ratio of heat transport by conduction and convection and is defined as:

$$Ra = GrPr \tag{4.22}$$

with the Grashof number as:

$$Gr = \frac{g\beta\Delta T L_{ch}^3}{\nu^2} \tag{4.23}$$

where g is the acceleration due to gravitation, β is the coefficient of thermal expansion of air, ΔT is the temperature difference between the ambient and the module surface, L_{ch} is a characteristic length of the module and ν is the kinematic viscosity of air. The critical Rayleigh number Ra_{cr} used in Eq. (4.21) accounts for the faster separation due to the inclination of the plate and the resulting earlier transition from laminar to turbulent flow. It is given by Klan & Thess [67] as:

$$Ra_{cr} = 10^{\left(8.9 - 0.00178(90° - \gamma_I)^{1.82}\right)} \tag{4.24}$$

For the bottom side, the following Nusselt correlation by Churchill & Chu [69] was used, which is applicable for all Rayleigh and Prandtl numbers:

$$Nu_{nc,bot} = \left(0.825 + \frac{0.387(\cos(90° - \gamma_I)Ra)^{1/6}}{(1 + (0.492/Pr)^{9/16})^{8/27}}\right)^2 \tag{4.25}$$

Consideration of the wind direction

The application of Eicker's [65] and Sartori's [63] correlations require the consideration of the wind direction since they make use of the characteristic length in flow direction. Further, the choice, whether to use Eq. (4.19) or (4.20), depends on the wind direction as well. The measured wind data gathered at the PV lab included the direction, which can take values between 0° and 359° (e.g., north at 0°, south at 180°). The modules at the Paderborn University PV lab face south, as indicated in Figure 4-8.

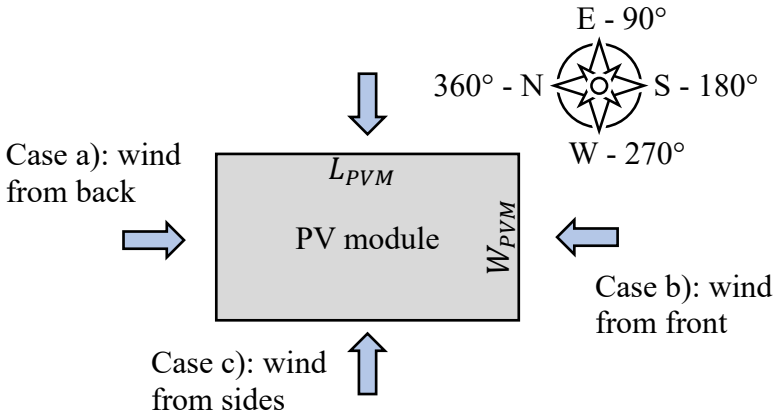

Figure 4-8: Orientation of the modeled PV modules and corresponding wind directions for the determination of the combined convective heat transfer coefficient – case a): wind from north (i.e., toward the module backside), case b): wind from south (i.e., toward the front), case c): wind from east or west (i.e., toward the sides)

The wind direction measured at the PV lab can be used to identify the windward and leeward side of the module, which was required to determine the characteristic length. Based on the cases specified in Figure 4-8, the characteristic length L_{ch} used for equations (4.15) and (4.17) is set to:

- the PV module length L_{PVM} for cases a) and b), when the wind direction takes a value between 315° and 45°, or 135° and 225°.
- the PV module width W_{PVM} for case c), when the wind direction takes a value between 45° and 135°, or 225° and 315°.

Further, the wind direction and the sign of the difference between the module surfaces and the ambient temperature determine whether to use Eq. (4.19) for assisting convective flow (forced and natural convection in the same direction) or Eq. (4.20) for opposing convective flow (forced and natural convection in opposite directions). In the following cases, where natural and forced convection follow the same direction, Eq. (4.19) is used:

- $T(x = 0) > T_{amb}$ & wind direction has a value between 90° and 270° (south)
- $T(x = s) < T_{amb}$ & wind direction has a value between 270° and 90° (north)

In the following cases when the convection types face opposite directions, Eq. (4.20) is used:

- $T(x = 0) < T_{amb}$ & wind direction has a value between 90° and 270° (south)
- $T(x = s) > T_{amb}$ & wind direction has a value between 270° and 90° (north)

4.4.2.2 Radiative heat flux

The radiative heat fluxes in equations (4.9) and (4.10) are determined by the radiative heat transfer coefficients $h_{r,ST}$, $h_{r,GT}$, $h_{r,SB}$ and $h_{r,GB}$, as well as the temperatures of the sky T_{sky} and the ground T_{gro}. For the top surface of the module the radiative heat flux is given as:

$$\dot{q}_{r,top} = h_{r,ST}\left(T_{sky} - T(x = 0)\right) + h_{r,GT}\left(T_{gro} - T(x = 0)\right) \tag{4.26}$$

The first term on the right side of Eq. (4.26) accounts for the radiative heat exchange between the sky and the top surface of the module (index ST), while the second term accounts for the radiative heat exchange between the ground and the top surface of the module (index GT).

Similarly, the radiative heat flux at the bottom is given as:

$$\dot{q}_{r,bot} = h_{r,SB}\left(T_{sky} - T(x = \mathrm{s})\right) + h_{r,GB}\left(T_{gro} - T(x = \mathrm{s})\right) \tag{4.27}$$

where the first term on the right-hand side accounts for the radiative heat exchange between the sky and the bottom surface of the module (index SB), while the second term accounts for the heat exchange between the ground and the bottom surface (index GB).

The radiative heat transfer coefficients can be determined by a linearized relationship (see Eq. (2.57)) discussed in section 2.5.1.2. Since the considered modules are installed with an inclination, the view factor F needs to be considered, which accounts for the partial radiative heat exchange between the sky and the module, and between the ground and the module, as shown in Figure 4-9.

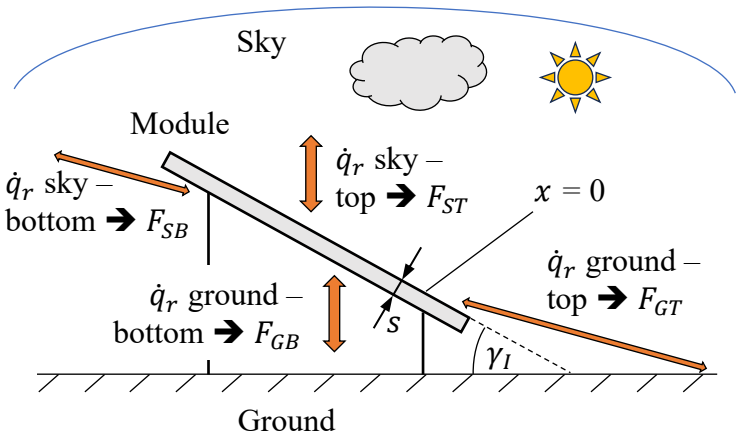

Figure 4-9: Radiative heat exchange between the PV module and its environment

Consequently, the radiative heat transfer coefficients at the top side of the module are:

$$h_{r,ST} = \sigma \varepsilon_{top} F_{ST} \left[\left(T(x=0)^2 + T_{sky}^2 \right) \left(T(x=0) + T_{sky} \right) \right] \tag{4.28}$$

$$h_{r,GT} = \sigma \varepsilon_{top} F_{GT} \left[\left(T(x=0)^2 + T_{gro}^2 \right) \left(T(x=0) + T_{gro} \right) \right] \tag{4.29}$$

For the bottom side, these coefficients are:

$$h_{r,SB} = \sigma \varepsilon_{bot} F_{SB} \left[\left(T(x=s)^2 + T_{sky}^2 \right) \left(T(x=s) + T_{sky} \right) \right] \tag{4.30}$$

$$h_{r,GB} = \sigma \varepsilon_{bot} F_{GB} \left[\left(T(x=s)^2 + T_{gro}^2 \right) \left(T(x=s) + T_{gro} \right) \right] \tag{4.31}$$

F_{ST}, F_{GT}, F_{SB} and F_{GB} are the view factors for radiative heat exchange between the sky and the top surface, between the ground and the top surface, between the sky and the bottom surface, and between the ground and the bottom surface, respectively (see also Figure 4-9). Here, σ denotes the Stefan-Boltzmann constant and ε_{top} and ε_{bot} the emissivity of the top and bottom layer of the module.

The view factors are defined as follows:

$$\begin{aligned} F_{ST} &= 0.5(1 + \cos(\gamma_I)) \\ F_{GT} &= 0.5(1 - \cos(\gamma_I)) \\ F_{SB} &= 0.5(1 + \cos(\pi - \gamma_I)) \\ F_{GB} &= 0.5(1 - \cos(\pi - \gamma_I)) \end{aligned} \tag{4.32}$$

The ground temperature T_{gro} was assumed to be equal to the ambient temperature, an assumption often found in literature [52,70].

Since the experimental setup at the PV lab did not measure the sky temperature T_{sky}, it was necessary to model it appropriately. Correlations found in literature often relate the sky temperature to the ambient temperature or the dew point temperature. Since the latter was not captured by measurements either, the sky temperature correlations used in this work were based on the ambient temperature and are listed in Table 4-5. For further details on the modeling of the sky temperature, the comprehensive review by Algarni & Nutter [71] can be consulted.

Table 4-5: Sky temperature correlations based on field test measurements

Equation		Author	Field test location
$T_{sky} = T_{amb} - 20$	(4.33)	Garg [72]	Australia
$T_{sky} = T_{amb} - 6$	(4.34)	Whillier [73]	Australia
$T_{sky} = 0.0552 T_{amb}^{1.5}$	(4.35)	Swinbank [74]	U.S.A.
$T_{sky} = 0.037536 T_{amb}^{1.5} + 0.32 T_{amb}$	(4.36)	Fuentes [75]	68 U.S.-locations

4.5 Experimental results and model validation

To validate the thermal model, the experimental data gathered from the test site described in section 4.3 was compared to the simulated results. The numerical algorithm is based on the scheme outlined in Chapter 3. The problem specific source term and boundary conditions are discussed in the previous section.

First, the measured data is presented and evaluated. The data is compared to the simulation results and the accuracy of the model is discussed. Next, the different correlations for the convective and radiative heat flux are evaluated, and the combination that best fits the measured data from the Paderborn University PV lab is presented.

4.5.1 Experimental results

For validation, the mean temperature of the four sensors shown in Figure 4-5 was calculated for each module. These mean temperatures along with the PV power output were then used for comparison with the simulation results for four different days without precipitation in July 2019. The days were selected based on the prevailing weather conditions to allow for representative model validation. These days were:

- July 2nd, a mostly sunny day with occasional clouds
- July 7th, a mostly cloudy day with occasional sunshine
- July 16th, a cloudy day
- July 23rd, a sunny day

The temperature and irradiance data for these four days are shown in Figure 4-10. It can be seen that the temperature curves for the PV modules behave similarly and follow the general course of the incoming irradiance. The temperatures of the reference module seem to be higher when the modules heat up and lower when they cool down, which points to the effect of the PCM layer acting as a heat sink. Further, the temperature curves of the PV-PCM modules seem to be smoother and show fewer small-scale fluctuations compared to the reference. The effect of the PCM thus leads to less temperature fluctuations with lower amplitude, which reduces thermally induced mechanical stress inside the PV

module. This effect has the potential to increase the lifetime of the module, an aspect that is discussed in more detail in section 4.6.

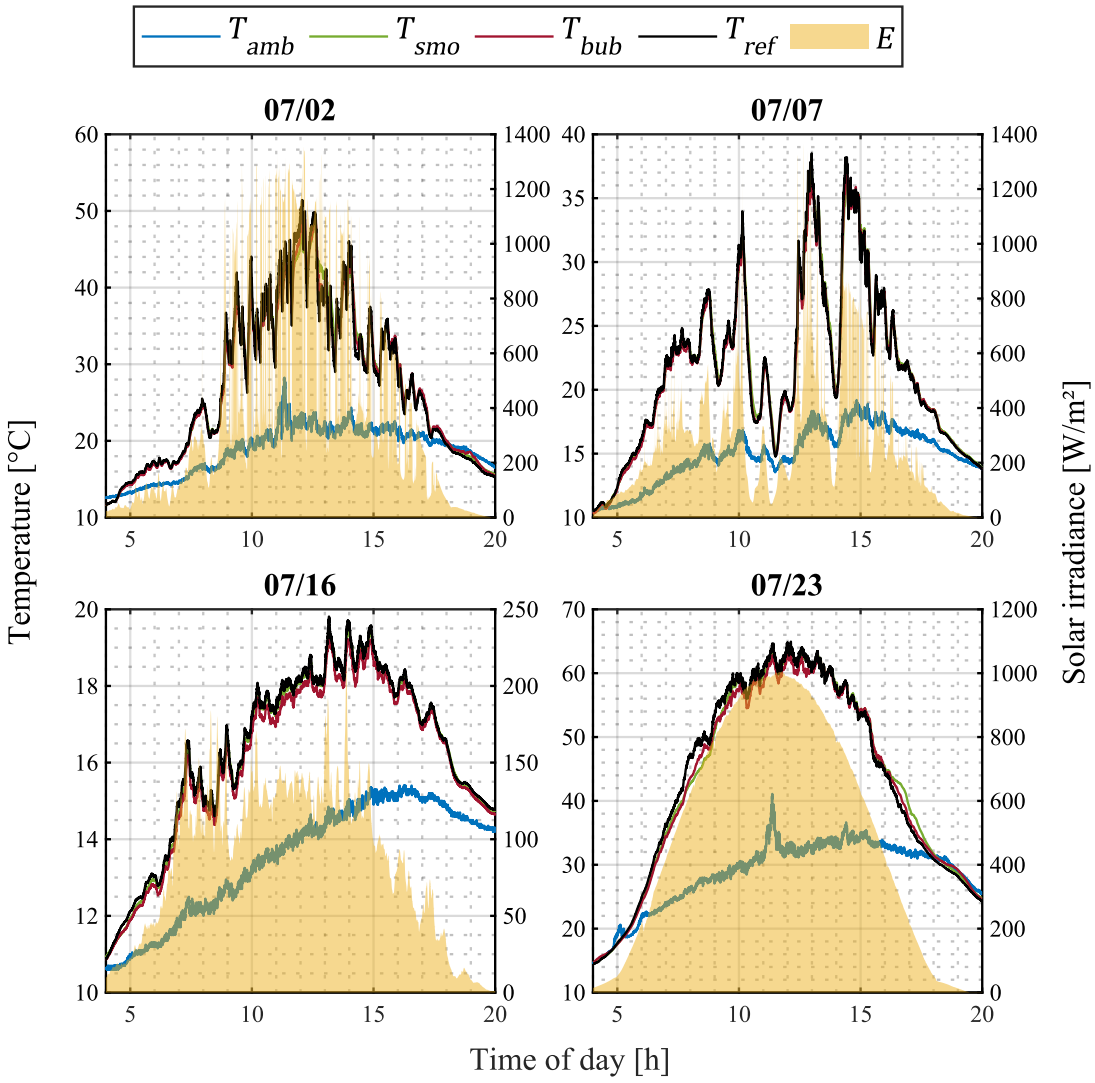

Figure 4-10: Experimental data for four days in July 2019: temperatures of the ambient T_{amb}, the PV-PCM module with smooth foil T_{smo}, the PV-PCM module with bubble wrap foil T_{bub}, and the reference PV module T_{ref}, as well as irradiance E

In order to evaluate the effect of the PCM, the temperature curves for July 2nd shown in Figure 4-11 are further examined. It is difficult to separate the effect of the phase change from other effects such as changes in the incoming solar irradiance due to clouds, wind speed fluctuations or the sensible heating/cooling of the PV module layers. The effect of the PCM on the temperature curves seems to be rather small, as the characteristic temperature plateau that appears during the phase change can hardly be identified. The effect of the sensible thermal inertia of the PCM layer seems to outweigh the phase change effect, even within the phase change temperature interval. The only time periods, during which the phase change could be the reason for smaller temperature fluctuations are those from 11:45 am to 12:15 pm and from 12:45 pm to 1:00 pm. During these periods, the phase change effect prevents the PV-PCM module temperatures from rising or falling as high or low as the reference module temperature. This effect is especially pronounced at times

when rapid changes in temperature can be observed, e.g., shortly before 11:00 am, at around 11:40 am, at around 12:40 pm and at around 2:15 pm. These rapid temperature changes are primarily due to sudden cloud cover, which can cause the incoming irradiance to drop by up to 1000 W/m². Changes in wind speed only seem to have a small effect on the overall course of the module temperatures.

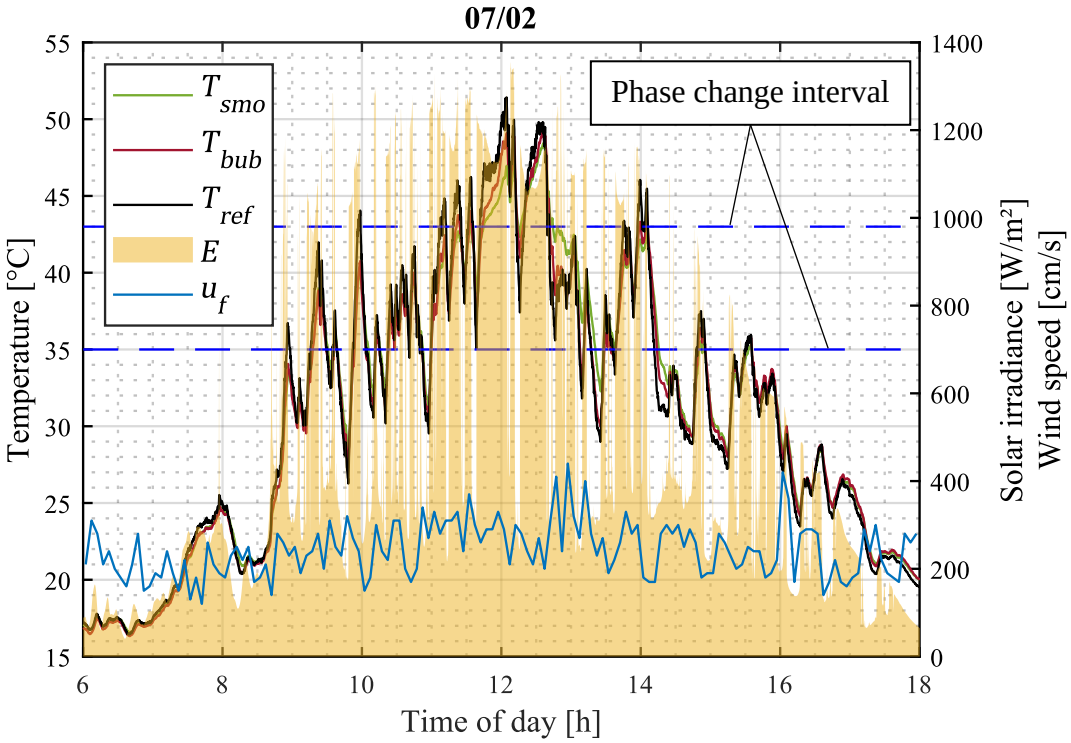

Figure 4-11: Measured module temperatures, solar irradiance and wind speed for July 2nd, 6 am through 6 pm

In conclusion, the PCM foils only seem to have a minor effect on the operating temperatures of the module. In fact, the mean temperature difference between the reference and the smooth foil module across all four days was only 0.613 K, and with 0.606 K it was even smaller for the PCM bubble wrap foil. However, the effect of the foils is more pronounced on the hotter days (2nd and 23rd of July), when the module temperatures exceed the PCM melting point. On these days, the temperature differences were greater than the four-day-average with 0.868 K for the smooth and 0.661 K for the bubble wrap foil on July 2nd, and 1.081 K for the smooth and 1.2 K for the bubble wrap foil on July 23rd. An interesting observation was that the bubble wrap foil led to lower temperatures on July 23rd compared to the smooth foil as can be seen in Figure 4-12. An explanation for this behavior could be that the extended surface of the bubble wrap acts like an array of cooling fins that dissipates heat to the environment more efficiently, while the smooth foil acts as a thermal insulator after the PCM has completely melted. This effect was more pronounced on days with few clouds and relatively low wind speeds.

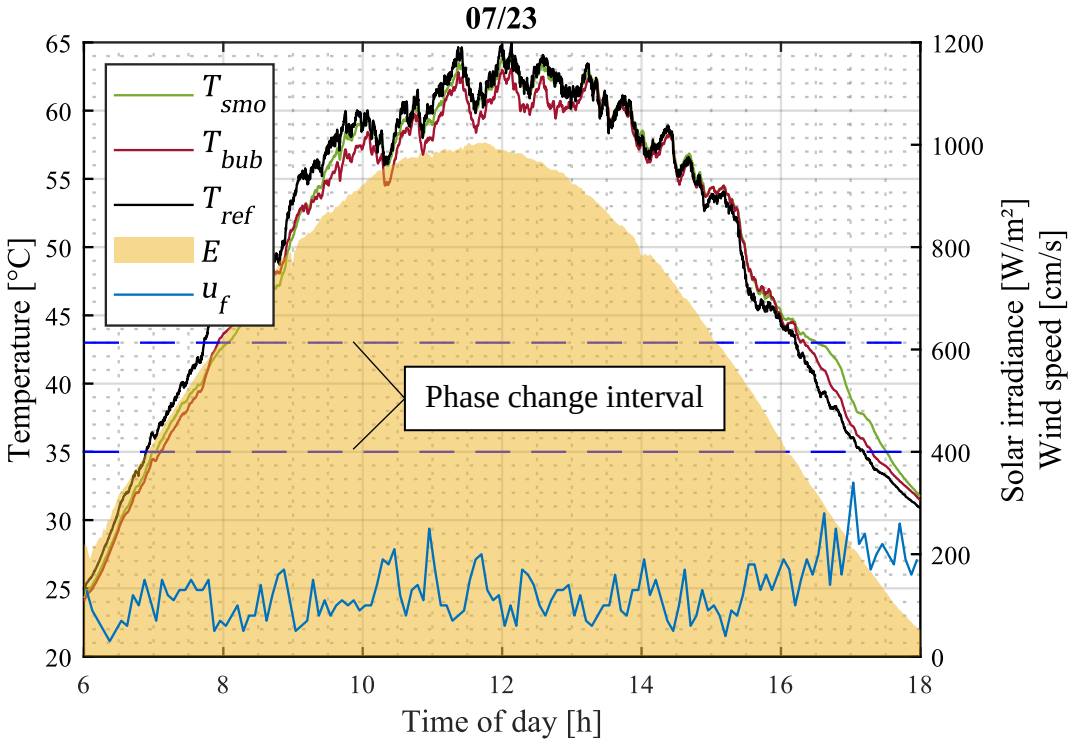

Figure 4-12: Measured module temperatures, solar irradiance and wind speed for July 23rd, 6 am through 6 pm

Regarding the energetic yield, Figure 4-13, left, shows the electrical power generated by the three module configurations for July 23rd between 8 am and 2 pm. It can be seen that the module with the bubble wrap PCM foil generated the highest and the smooth PCM foil module the lowest power. In fact, P_{bub} is up to 14 W higher than P_{smo} at times – a difference of 8.2 %. This observation might lead to the conclusion that the smooth foil has a negative effect on the module performance. Also, it disagrees with the measured temperatures shown in Figure 4-12, since the highest cell temperatures should cause the lowest power output. However, the reference module generated a higher power output than the smooth foil module, even though it was exposed to the highest temperatures.

A possible explanation for this behavior lies in the combined effect of two aspects: the PCM foils, but also the reference power, which differs for each module as was revealed by the flash tests described in section 4.3. Thus, to identify the influence of the PCM foils, the power output was normalized with respect to the module reference power listed in Table 4-2. Accordingly, the normalized electrical power P^* was calculated as:

$$P^* = P_{PV}/P_{ref} \tag{4.37}$$

Examining the normalized power output shown in Figure 4-13, right, the curves for all three modules lie much closer together. In fact, the maximum difference between the smooth and the bubble wrap foil module now amounts to only 3.1 %. Also, the curves now agree better with the measured temperatures as the module with the highest temperatures has the lowest normalized power output (i.e., the reference module), while the module with the lowest temperatures generates the highest power output (i.e., the bubble wrap foil module).

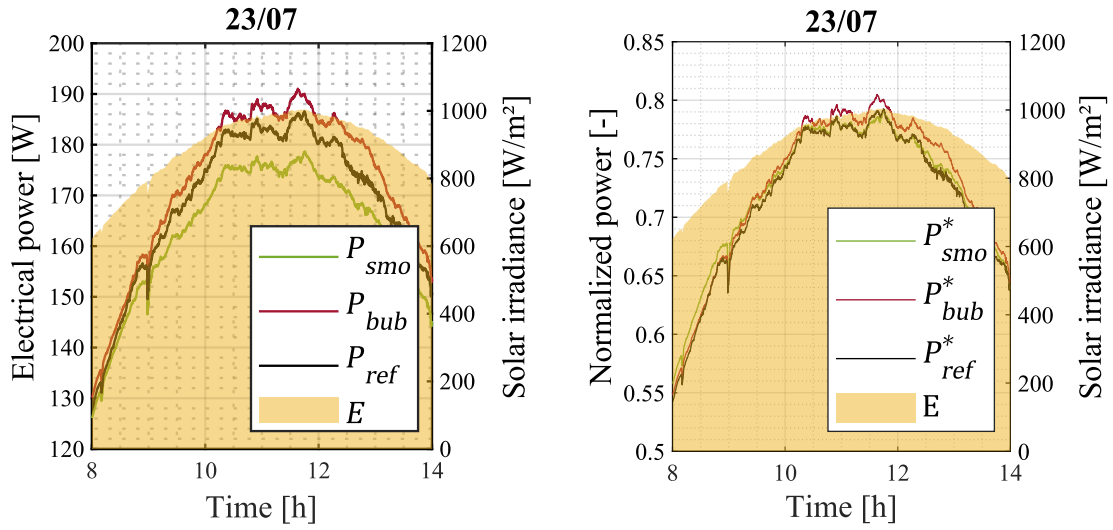

Figure 4-13: Measured electrical power (left) and normalized power (right) generated by the three module configurations on July 23rd between 8 am and 2 pm

To quantify the effect of the PCM foils on the electrical energy output, the average power and average normalized power throughout July 2019 were used and are given in Figure 4-14. As the left chart shows, the smooth foil module appears to perform worse than the other two module configurations when only the nominal power output is considered. Again, this is mostly due to the low reference power of the smooth foil module and not due to the PCM. In fact, Figure 4-14, right, shows that the smooth foil module configuration performs best when the normalized power output is considered, while the bubble wrap foil and reference module are second and third. This means that the greatest improvement attributed to the PCM heat sink was observed for the module configuration with the smooth PCM foil.

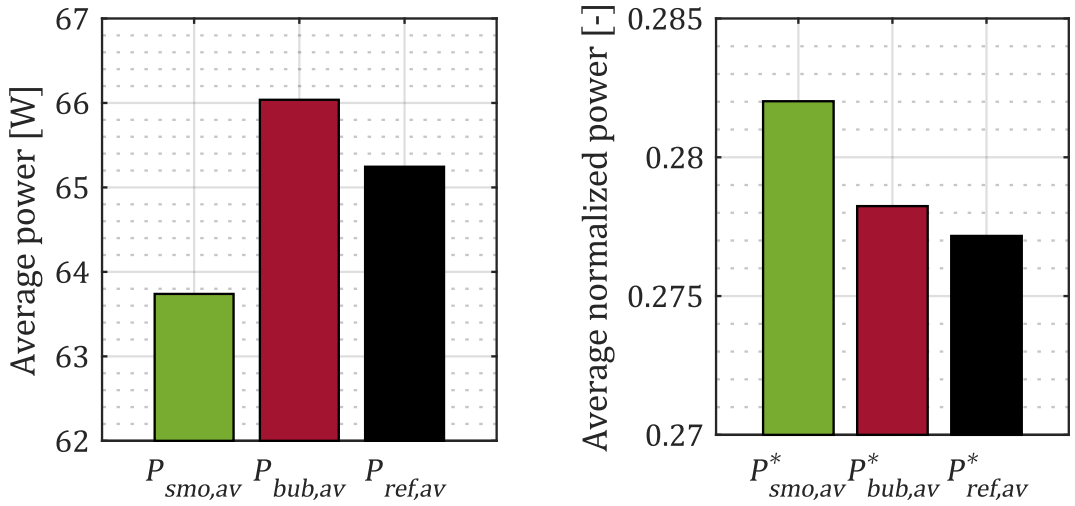

Figure 4-14: Averaged (index av) power (left) and averaged normalized power (right) of the three module configurations for July 2019

In summary, the analysis of the experimental data showed that the influence of the PCM heat sink configurations on the module temperatures is relatively small and lies within less than ±1 K. However, a dampening effect of the PCM on the temperature fluctuations

was visible and a relative improvement regarding the electrical power output could be observed. Both effects were greatest for the smooth PCM foil configuration.

4.5.2 Model validation

Before the validation was carried out, it had to be ensured that the simulation results did not depend on the spatial grid spacing (spatial step Δx). Therefore, a grid independence study was performed for the day of July 2nd. It was carried out by first running an initial simulation with a spatial step size of 50 µm followed by the reduction of the step size by half for each consecutive simulation run until no significant change in the results could be observed. The step size determined by this procedure was 5 µm, which means the thinnest layer of the module composition (the solar cell) was divided into 40 spatial nodes. The time step was set to 2.5 s for each simulation.

To determine the accuracy of the thermal model introduced in section 4.4, the experimental data recorded on the aforementioned four days in July 2019 was compared to the results from simulations performed with the thermal model of PV-PCM systems outlined in section 4.4. The following measured data were used as input for the model:

- Solar irradiance
- Ambient temperature
- Wind speed and direction

Other inputs include the geometric and performance specifications of the modules as well as material properties (see also Table 4-3). As mentioned above, the correlations for the convective heat transfer coefficient (Table 4-4) and the temperature of the sky (Table 4-5) were tested in all possible constellations resulting in 16 different combinations. These 16 combinations were tested for all four days considered. To evaluate the model accuracy, the mean absolute error MAE (see Eq. (3.43)) and the root mean square error $RMSE$ (see Eq. (4.1)), averaged across the four days considered, were used.

Table 4-6 shows the values of the temperature error MAE_T for the PV module with the smooth PCM foil attached to it. It can be seen that the combination giving the least deviation is that using the correlations developed by Sartori [63] / Kaplani & Kaplanis [64] (Eq. (4.15) and (4.16)) for the convective heat transfer coefficient h_c and Whillier [73] (Eq. (4.34)) for the temperature of the sky T_{sky}, which results in an MEA_T of 1.21 K. Assuming an average temperature range across all four days of 32 K as reference value, the corresponding $RMAE_T$ is 3.78 %.

Table 4-6: Mean absolute temperature error averaged across the four considered days for 16 combinations of correlations for the sky temperature and the convective heat transfer coefficient (minimum value in bold)

T_{sky} ↓ h_c →	Eq. (4.13)	Eq. (4.14)	Eq. (4.15) & (4.16)	Eq. (4.17) & (4.18)
Eq. (4.33)	3.83	3.75	2.80	2.94
Eq. (4.34)	2.25	2.16	**1.21**	1.33
Eq. (4.35)	3.39	3.30	2.39	2.52
Eq. (4.36)	2.78	2.69	1.78	1.90

Taking a look at the $RMSE_T$ values shown in Table 4-7, the combination with the least deviation is the same as for the MAE_T, with a value of 1.46 K (4.56 %). This represents a significant improvement in accuracy compared to the lowest $RMSE$ value of 3.2 K (8.89 %) found in the literature reviewed in section 4.1.2.

Table 4-7: Root mean square temperature error averaged across the four considered days for 16 combinations of correlations for the sky temperature and the convective heat transfer coefficient (minimum value in bold)

T_{sky} ↓ h_c →	Eq. (4.13)	Eq. (4.14)	Eq. (4.15) & (4.16)	Eq. (4.17) & (4.18)
Eq. (4.33)	4.17	4.07	2.94	3.11
Eq. (4.34)	2.68	2.57	**1.46**	1.57
Eq. (4.35)	3.74	3.64	2.57	2.71
Eq. (4.36)	3.20	3.09	2.01	2.13

For the power output, similar error calculations were performed. The results are shown in Table 4-8 and Table 4-9. Surprisingly, here, the opposite behavior as for the temperature can be observed. The combination with the best accuracy for the temperature shows the worst accuracy for the calculated power output. However, the difference between all combinations is marginal as the MAE_P values vary only between 3.05 W and 3.22 W. This corresponds to an $RMAE_P$ 1.33 % and 1.40 %, respectively, when using the nominal electrical power of the PV module of 230 W as the reference.

Table 4-8: Mean absolute power error averaged across the four considered days for 16 combinations of correlations for the sky temperature and the convective heat transfer coefficient (maximum value in bold)

T_{sky} ↓ h_c →	Eq. (4.13)	Eq. (4.14)	Eq. (4.15) & (4.16)	Eq. (4.17) & (4.18)
Eq. (4.33)	3.08 W	3.08 W	3.05 W	3.05 W
Eq. (4.34)	3.14 W	3.14 W	**3.22 W**	3.20 W
Eq. (4.35)	3.06 W	3.06 W	3.08 W	3.07 W
Eq. (4.36)	3.09 W	3.10 W	3.15 W	3.13 W

The $RMSE_P$ values listed in Table 4-9 show a trend similar to that of the MAE_P values. The combination that provides the best accuracy for temperature leads to the worst accuracy for power output. As with the MAE_P values, the range of $RMSE_P$ values is quite narrow, varying only between 4.00 W (1.74 %) and 4.29 W (1.87 %).

Table 4-9: Root mean square power error averaged across the four considered days for 16 combinations of correlations for the sky temperature and the convective heat transfer coefficient (maximum value in bold)

T_{sky} ↓ h_c →	Eq. (4.13)	Eq. (4.14)	Eq. (4.15) & (4.16)	Eq. (4.17) & (4.18)
Eq. (4.33)	4.02 W	4.02 W	4.04 W	4.03 W
Eq. (4.34)	4.10 W	4.11 W	**4.29 W**	4.26 W
Eq. (4.35)	4.00 W	4.00 W	4.10 W	4.08 W
Eq. (4.36)	4.04 W	4.05 W	4.20 W	4.16 W

The same correlation testing procedure was performed for the reference module. Here it was found that the same combination as for the smooth foil module, i.e., Sartori [63] / Kaplani & Kaplanis [64] (Eq. (4.15) and (4.16)) and Whillier [73] (Eq. (4.34)), achieved the highest accuracy with an MAE_T of just 1.12 K (3.50 %) and an $RMSE_T$ of 1.36 K (4.25 %). Comparing these values to that reported for the thermal model of PV systems by Notton et al. [51], which showed the lowest $RMSE_T$ of 1.3 K (3.25 %) in the literature reviewed in section 4.1.2, leads to the conclusion that the model developed in this case study also works very well for conventional PV systems. Good results were also achieved regarding the power output, with an MAE_P of 3.00 W (1.31 %) and an $RMSE_P$ of 3.96 W (1.72 %).

After two of the three module configurations were simulated using various correlations, it was found that the combination with the best accuracy in terms of the module temperature prediction was Sartori [63] / Kaplani & Kaplanis [64] (Eq. (4.15) and (4.16)) and Whillier [73] (Eq. (4.34)). However, this combination gave a relatively low accuracy for the predicted power output, albeit only marginally. This seems surprising, as the electrical power output is directly coupled with the cell temperature via the module efficiency (see

Eq. (4.7) and (4.8)). Therefore, it was expected that if the temperature is predicted well, the power output prediction should also be accurate. A possible explanation for this mismatch could be that the efficiency correlation by Evans & Florschuetz [60] (Eq. (4.8)) is inaccurate, or that the reference values for the module η_{ref}, β_{ref} and/or T_{ref} provided by the manufacturer were not correctly determined. However, since the main goal of this case study was to develop a thermal model to predict the cell temperature, the combination chosen for further investigations was Sartori [63] / Kaplani & Kaplanis [64] for h_c together with Whillier [73] for T_{sky}.

This combination also showed good results for the module with the bubble wrap PCM foil. In this case, a major approximation was employed: the PCM volume inside the bubbles was summed up and then evenly distributed as a smooth PCM layer which had a resulting thickness of 0.78 mm. This simplification allowed the application of the model without further modifications. The resulting MAE_T and $RMSE_T$ were 1.29 K (4.03 %) and 1.58 K (4.93 %), respectively, which is the lowest accuracy for all three simulated module configurations. The resulting MAE_P and $RMSE_P$ were 2.76 W (1.20 %) and 3.63 W (1.58 %).

All in all, the thermal model with the correlation combination Sartori [63] / Kaplani & Kaplanis [64] (Eq. (4.15) and (4.16)) and Whillier [73] (Eq. (4.34)) predicts the temperatures of all three module configurations quite well, with an average MAE_T of less than 1.3 K (4.06 %) and an average $RMSE_T$ of less than 1.6 K (5.00%).

To evaluate the impact of different weather conditions, the MAE and $RMSE$ resulting from using this correlation combination for the individual days are listed in Table 4-10. The highest single-day MAE_T was observed for the module with the bubble wrap foil with a value of 1.44 K (4.50 %) on July 16th (the cloudy day). The lowest MAE_T was observed for the reference module with 0.67 K (2.09 %) on July 7th (the mostly cloudy day with occasional sunshine). The $RMSE$ values match the MAE ones only partially, as the highest $RMSE_T$ with 2.00 K (6.25 %) was found for the bubble wrap foil module on July 23rd, i.e., the sunny day (as opposed to the highest MAE_T on July 16th). The lowest $RMSE_T$, however, coincides with the lowest MAE_T on July 7th for the reference module. Remarkably, the error values for the electrical power output are among the highest for this day and module, an observation that corresponds to the findings made above based on Table 4-6 through Table 4-9.

Table 4-10: Deviations between the modeled and simulated temperature and power values for the three module configurations on the four considered days of July 2019

	Reference module					Module with smooth PCM foil					Module with bubble wrap PCM foil				
July	02nd	07th	16th	23rd	**Mean**	02nd	07th	16th	23rd	**Mean**	02nd	07th	16th	23rd	**Mean**
MAE_T [K]	1.10	0.67	1.37	1.32	**1.12**	1.02	1.06	1.42	1.35	**1.21**	1.12	1.16	1.44	1.43	**1.29**
$RMSE_T$ [K]	1.42	0.83	1.42	1.76	**1.36**	1.29	1.18	1.46	1.91	**1.46**	1.51	1.33	1.47	2.00	**1.58**
MAE_p [W]	3.11	4.25	1.94	2.72	**3.00**	3.31	4.46	2.07	3.06	**3.22**	2.76	3.28	1.71	3.26	**2.76**
$RMSE_P$ [W]	4.44	5.53	2.42	3.46	**3.96**	4.87	5.77	2.56	3.98	**4.29**	4.02	4.36	2.10	4.05	**3.63**

To get a qualitative understanding of the simulation results, Figure 4-15 shows the simulated and measured temperatures for the module with smooth PCM foil on the four considered days. The simulated and experimental data correspond well, and the model accurately predicts the temperature course throughout the day. The times of temperature peaks and valleys are predicted correctly, although for the two cooler days (July 7th and 16th), the model seems to systematically underpredict the module temperatures.

On the very sunny day (July 23rd), the simulation results show larger fluctuations than the experimental data. However, the highest overshoot can be attributed to the concurrent peak in ambient temperature measured at around 11:20 am. This sudden ambient temperature increase and equally sudden drop after only a few minutes seems unrealistic as the ambient temperature is rather inert and usually follows a steadier slope. A similar peak could also be observed on July 2nd at the same time of day, but not on the two cloudy days. This suggests that the ambient temperature sensor was likely exposed to direct sunlight for a short period of time leading to an inaccurately high temperature reading. Since the measured ambient temperature serves as one of the input parameters to determine the convective and radiative heat transfer coefficients, the model cannot predict the module temperatures properly if the measured ambient temperature is incorrect.

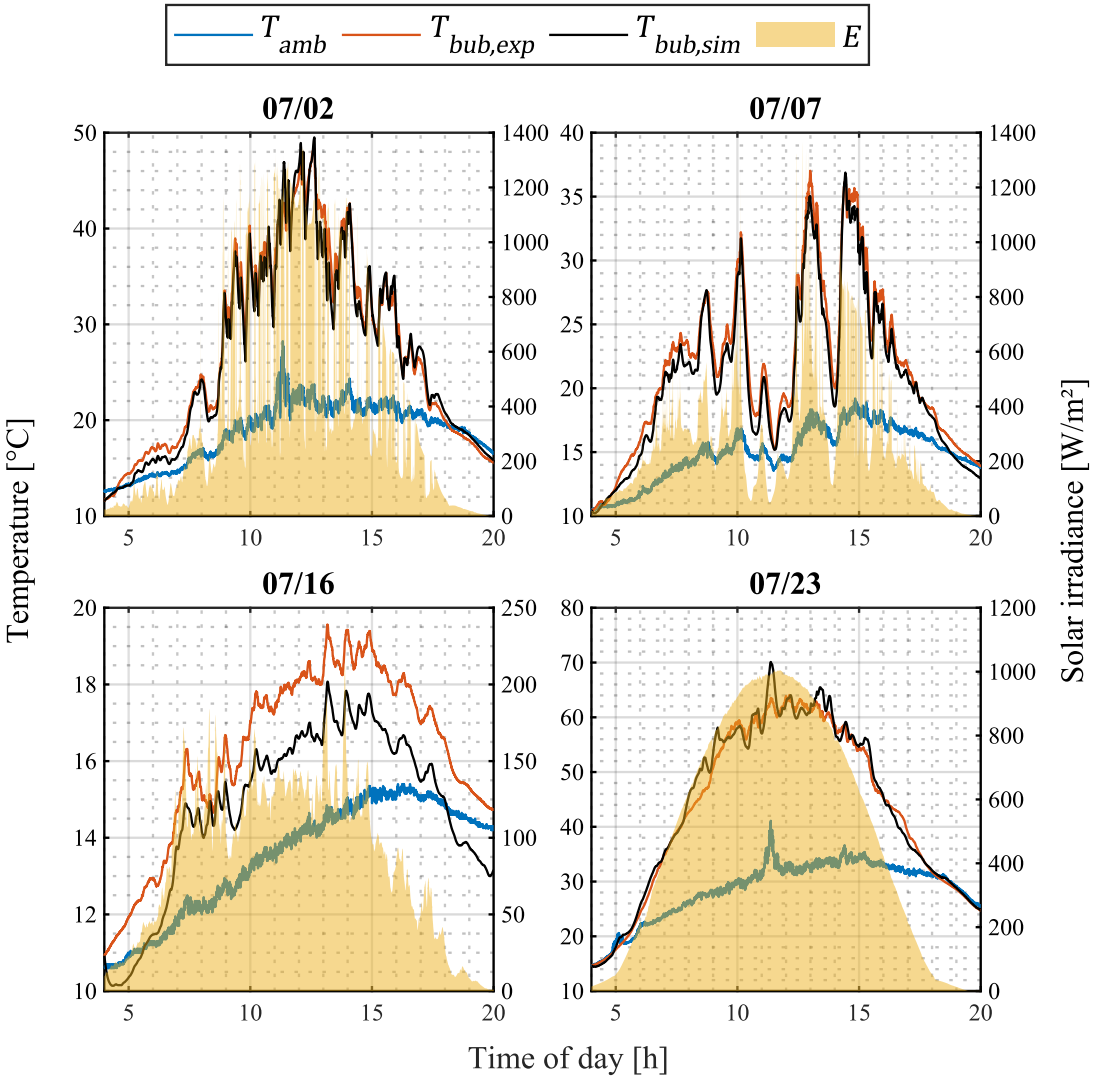

Figure 4-15: Simulated and measured temperatures for the PV-PCM module with smooth PCM foil on four days in July 2019

Figure 4-16 shows the temperature plots for the reference module. As was discussed above, the average temperature deviations between the experimental and simulation results were the smallest for this setup, which is also observable in the diagrams. The simulated temperature curves are closer to the measured ones than in Figure 4-15. On July 2rd, the model seems to slightly overpredict the temperatures. On July 7th and 23rd, the simulated temperature fluctuations are slightly larger than the experimental ones. And on July 16th the model systematically underestimates the module temperature, an observation that was made for the smooth foil setup as well. Also, the already mentioned unrealistic ambient temperature peak at around 11:20 am leads to a short-lived but significant overprediction by the model on the two sunny days.

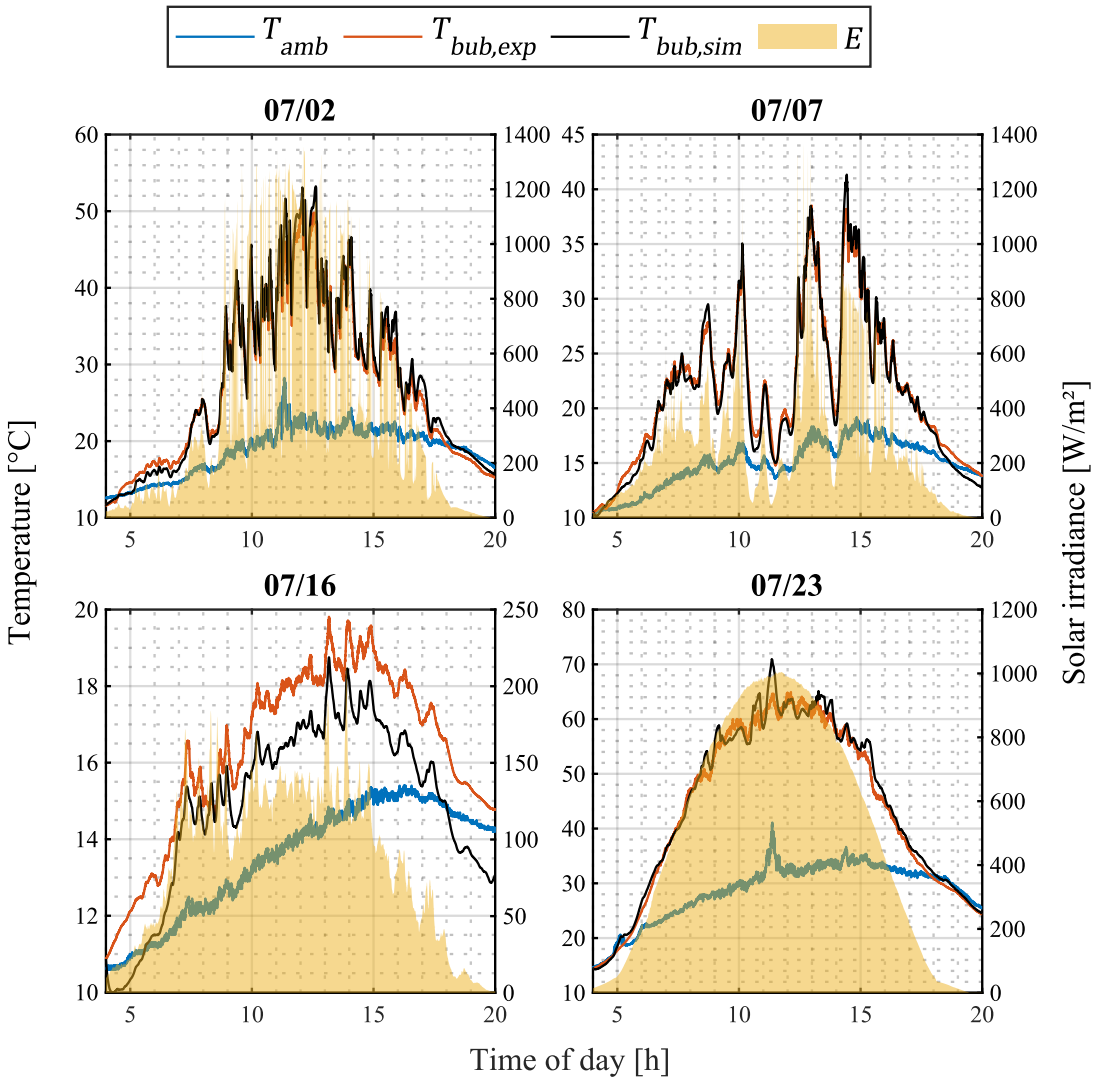

Figure 4-16: Simulated and measured temperatures of the reference PV module for four days in July 2019

Figure 4-17 shows the simulated and measured temperatures for the PV module with the bubble wrap PCM foil. Similar observations as above can be made: the general temperature course is captured well, while some fluctuations are overpredicted, especially for July 2nd and 7th. The simulated temperatures for July 16th are generally too low and for July 23rd too high. As was previously concluded by the error analysis above, the model shows the lowest accuracy for this setup, which is also confirmed by the temperature plots.

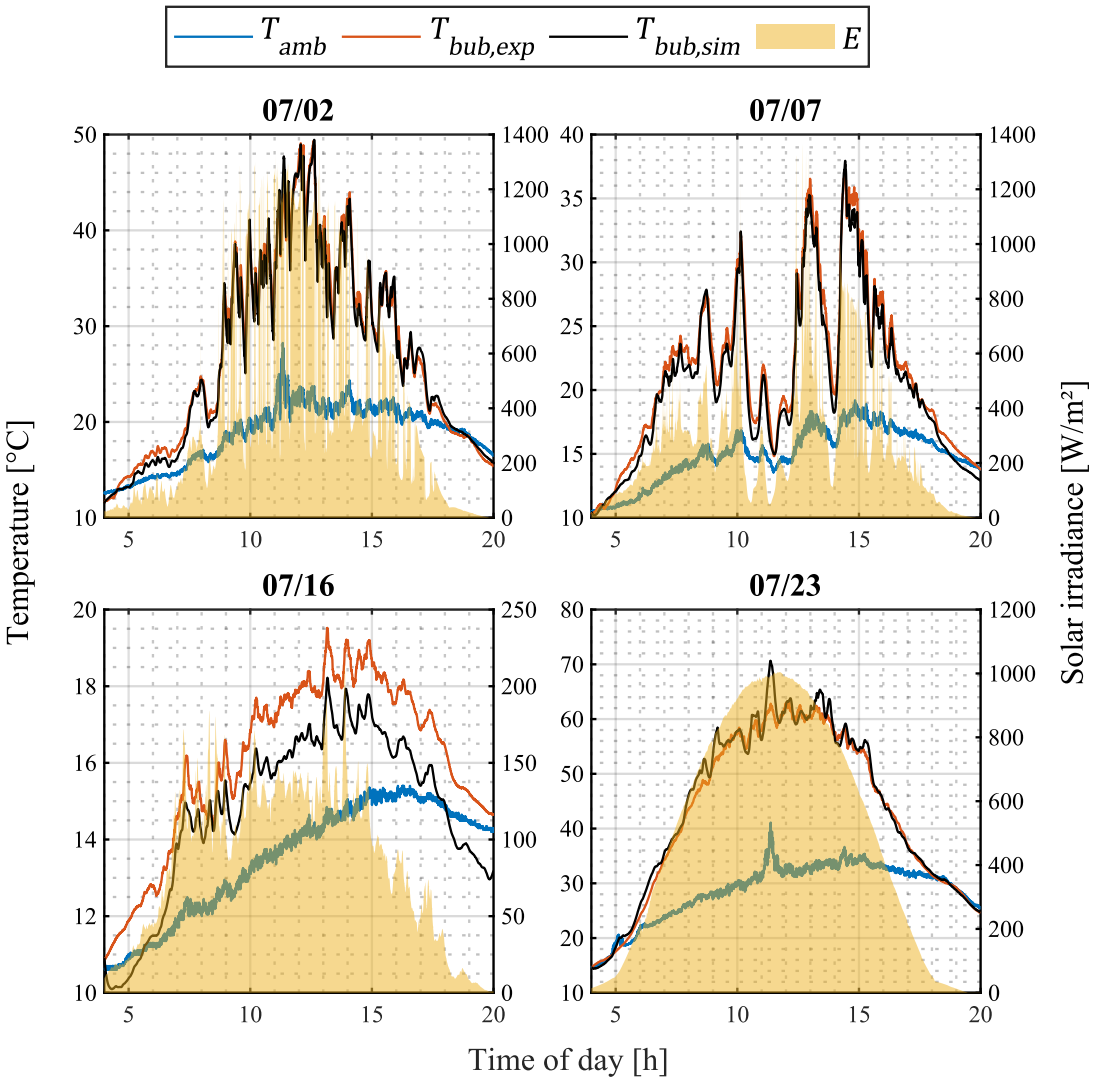

Figure 4-17: Simulated and measured temperatures of the PV-PCM module with bubble wrap PCM foil for four days in July 2019

In conclusion, the thermal model with the correlation combination Sartori [63] / Kaplani & Kaplanis [64] for the convective heat transfer coefficient and Whillier [73] for the temperature of the sky gave the least average deviations for the three considered experimental setups. The average MAE_T was 1.12 K (3.50 %) for the reference module, 1.21 K (3.78 %) for the smooth PCM foil module and 1.29 K (4.03 %) for the bubble wrap PCM foil module. The corresponding $RMSE_T$ values were 1.36 K (4.25 %), 1.46 K (4.56 %), and 1.58 K (4.94 %). Compared to the error values reported in literature (see section 4.1.2), these results are excellent, especially for the two PV-PCM modules. Also, the qualitative analysis of the temperature plots showed a good agreement between measured and simulated data, although there appears to be a systematic underestimation of the cell temperature for the cloudy day (July 7th). These deviations seemed acceptable, as cloudy days are less relevant for degradation (only small temperature fluctuations) and electrical yield (low irradiance).

Since the simulations produced $RMSE_T$ values of 2 K (6.25 %) or less, one of the main goals of this case study, as outlined in section 4.2, was successfully achieved. Therefore,

the validated model could be used to investigate the influence of different PCM heat sink configurations on the lifetime and electrical energy yield of PV modules.

4.6 Degradation estimation

As discussed in section 4.1.2, degradation due to thermal fatigue is one of the major factors limiting the lifetime of PV modules. A PCM heat sink can act as thermal inertia and reduce the amount and amplitude of damaging temperature oscillations inside the module. The weak points for thermal fatigue in a PV module are its interconnectors, which electrically connect the individual solar cells through an S-shaped interconnector band, as illustrated in Figure 4-18. When the module is subjected to temperature fluctuations, the individual materials expand at different rates in accordance with their coefficient of thermal expansion. This causes mechanical stress and friction, which over time can lead to the detachment of the interconnectors from the cells or breakage of the S-shape interconnector band.

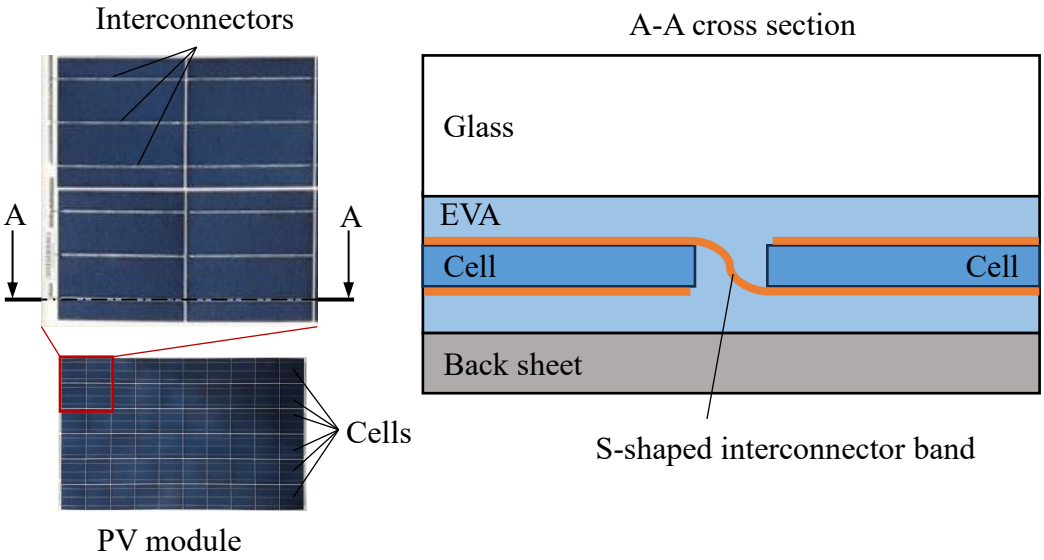

Figure 4-18: Structure of a PV module with focus on the interconnectors

In order to evaluate the effect of a PCM heat sink on the module lifetime, the method proposed by Weber et al. [45], which is based on the summation of thermal cycles using a rainflow-counting algorithm (RFCA) was applied. This algorithm identifies relevant full and half cycles of a fluctuating quantity, here, the temperature. A detailed description of the RFCA used by Weber et al. [45] is given in [76]. The input for the algorithm is the temperature history, either measured or simulated, over a specified period of time. The output quantities are the number of specific temperature cycles n, characterized by the cycle amplitude ΔT, the maximal cycle temperature T_{max} and the cycle duration t_c. The latter three of those quantities can be used to estimate the number of cycles until failure N_f (defined here as the breakage of the interconnector band) by the Coffin-Manson equation (see [77]) in the form proposed by Cui [78]:

$$N_f = k_{\mathrm{CM}} \Delta T^{-2} \left(\frac{1}{t_c}\right)^{\frac{1}{3}} e^{\frac{E_a}{k_{\mathrm{B}} T_{max}}} \tag{4.38}$$

Here, E_a denotes the material-specific activation energy, which takes a value of 0.5 eV for the interconnectors mostly made of copper. Further, k_B is the Boltzmann constant and k_{CM} is an empirical, problem-specific factor that has to be determined via experiments or mechanical-stress simulations using a finite element method. As argued by Bosco et al. [79], it can be assumed that k_{CM} takes the same value for the three considered modules, since their interconnector geometries are similar. This allows for a relative comparison of the damage received by the three module setups (since k_{CM} is canceled out), which can be determined using the Palmgren-Miner linear damage hypothesis [80]:

$$D = \sum\nolimits_{i=1} \frac{n_i}{N_{f,i}} \tag{4.39}$$

Eq. (4.39) represents the damage accumulation in the interconnector band based on the ratio of the actual number of specific temperature cycles n_i identified by the RFCA for a given day, to the maximum number of such specific cycles $N_{f,i}$ that the interconnector band can endure until failure. The accumulated damage D is calculated by summing up these ratios over all relevant characteristic cycles. When D = 1, the interconnector band has reached the point of failure.

Making use of the RFCA method by Weber et al. [45] and equations (4.38) and (4.39), the damage received by the three module configurations can be estimated based on the simulated solar cell temperatures. Since Eq. (4.39) yields rather small values ($< 10^{-9}$) and the relative comparison between the three module configurations was of interest, it is more convenient to express D in relation to a reference value. Here, this reference value was the total accumulated damage received by the reference module $D_{ref,acc}$ during the time span considered.

The accumulation of relative damage during July 2nd is shown in Figure 4-19. It can be seen that the PCM heat sink significantly reduces the degradation for this day. The module with the bubble wrap PCM foil only takes 60 % and the smooth foil module takes only 56 % of the damage that was received by the reference module.

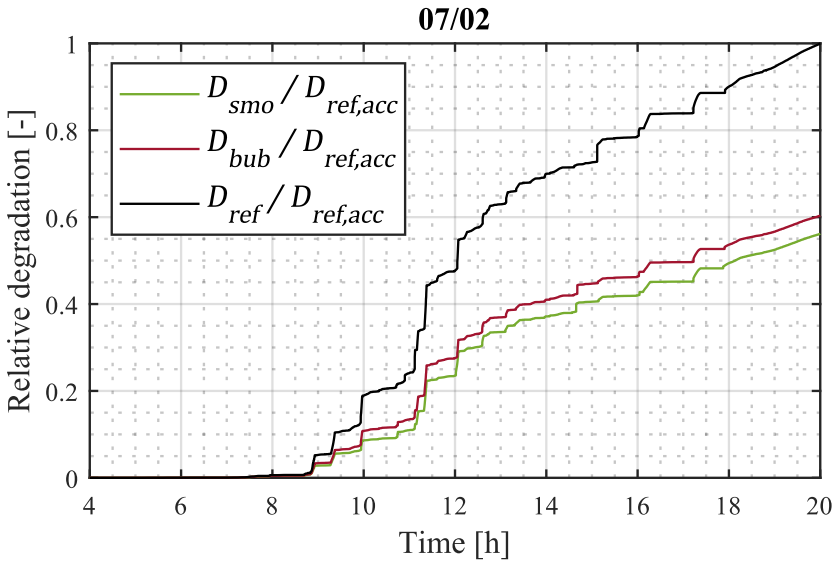

Figure 4-19: Relative damage accumulation during July 2nd for the three considered module configurations

The relative degradation for the other considered days is listed in Table 4-11. For July 7th, the relative damage values are similar to those determined for July 2nd. As expected, the difference to the reference module becomes smaller for days with more steady temperature courses, i.e., for July 16th and 23rd, since there are lower and fewer temperature fluctuations. The effect of the PCM heat sink is much smaller for these days, and especially for the hot and sunny 23rd of July it is only marginal. Altogether, the relative reduction in degradation varied between 3 % and 45 %.

Table 4-11: Relative accumulated damage received by the PV-PCM modules on the four considered days of July 2019

	Smooth foil	Bubble wrap foil
07/02/2019 (mostly sunny)	56 %	60 %
07/07/2019 (mostly cloudy)	55 %	63 %
07/16/2019 (cloudy)	74 %	80 %
07/23/2019 (sunny)	92 %	97 %
Four-day average	69 %	75 %

To estimate the lifetime improvement attributed to the PCM heat sink, the economic lifetime of PV modules can be taken as a basis, which lies between 25 and 30 years. Assuming that the heat sink can reduce degradation by up to 45 % the lifetime may be increased by more than ten years through the addition of PCM. On the other hand, the improvement would be less than a year if a reduction of only 3 % is assumed. Of course, other failure modes for PV modules exist along with fatigue as it only accounts for around 40 % of all module failures [44].

In conclusion, by using the RFCA and the Coffin-Manson approach it was shown that the PCM heat sink has a positive effect on the mitigation of fatigue-induced degradation of PV modules. Quantifying the concrete gain in lifetime is challenging as temperature fluctuations depend on the specific weather conditions. The lifetime-improving effect is greatest for unsteady weather conditions such as those observed for most of the year in temperate climate zones but rather small for steady conditions observed in arid or continental ones. Therefore, the feasibility of the PCM heat sink in terms of lifetime-improvement depends on the location of the PV site and the prevailing weather conditions.

4.7 Parameter study

To analyze the impact of different PCM heat sink configurations on the PV conversion efficiency and degradation, a parameter study was performed using a generic PCM. The module specifications remained the same as before (see Table 4-3). The parameters that were varied included the thickness of the PCM layer, the PCM phase change temperature and the PCM thermal conductivity. The other PCM properties remained constant. Further, the PCM properties were considered independent of the state of the PCM (properties of solid PCM were the same as the liquid ones). All simulations were performed with weather data from July 2nd 2019, because this day showed a high number of temperature fluctuations allowing the thermal dampening effect of the PCM layer to be investigated. At the same time, the solar irradiance on this day was still quite high, which offers a good opportunity to study the effect of the heat sink on the energy yield.

The thickness was increased in three steps from 5 mm to 30 mm. The phase change temperature was varied between 29-31 °C, 39-41 °C and 49-51 °C, meaning a phase change interval of 2 K was assumed. The thermal conductivity was varied between 0.2 W/mK (which corresponds to the conductivity of most paraffin based PCM) to 5 W/mK (which is unrealistically high for most PCM). All possible parameter combinations were tested resulting in a total of 27 simulations that were performed during the parameter study. All PCM heat sink properties for the study are given in Table 4-12.

Table 4-12: PCM heat sink properties varied throughout the parameter study

Thickness [mm]	Phase change temperature [°C]	Conductivity [W/mK]	Latent heat [kJ/kg]	Heat capacity [J/kgK]	Density [kg/m³]
5	29-31	0.2	200	2.000	800
15	39-41	2.5			
30	49-51	5.0			

Graphical representations of the parameter study results are shown in Figure 4-20 and Figure 4-21, in which the generated electrical energy and the accumulated damage are illustrated by bar charts for the considered parameter combinations. Regarding the generated electrical energy, it can be seen that the PCM heat sink configuration with a

conductivity of 5 W/mK, a phase change temperature of 29-31 °C and a thickness of 30 mm yields the highest amount of electrical energy. This result is somewhat surprising as an increase in foil thickness was expected to cause higher cell temperatures and thus a lower efficiency due to the insulating effect of the liquified PCM. However, this insulation effect was overcome by the relatively high thermal conductivity of 5 W/mK, which is an unrealistically large value for most PCM. But even a conductivity of 2.5 W/mK appears to offset the insulating effect as it yields the second highest amount of electrical energy. To increase the thermal conductivity to such high values, graphite could be added to the PCM, as was demonstrated by Japs et al. [41]. They measured a thermal conductivity of 2.4 W/mK for a 20 % mass fraction of expanded graphite, which, however, came at the expense of a lower latent heat capacity.

The combination yielding the lowest amount of electrical energy was the one with low thermal conductivity, high phase change temperatures and a large foil thickness, as was expected. Here, the PCM foil acts as a thermal insulator, which leads to high cell temperatures causing low efficiency.

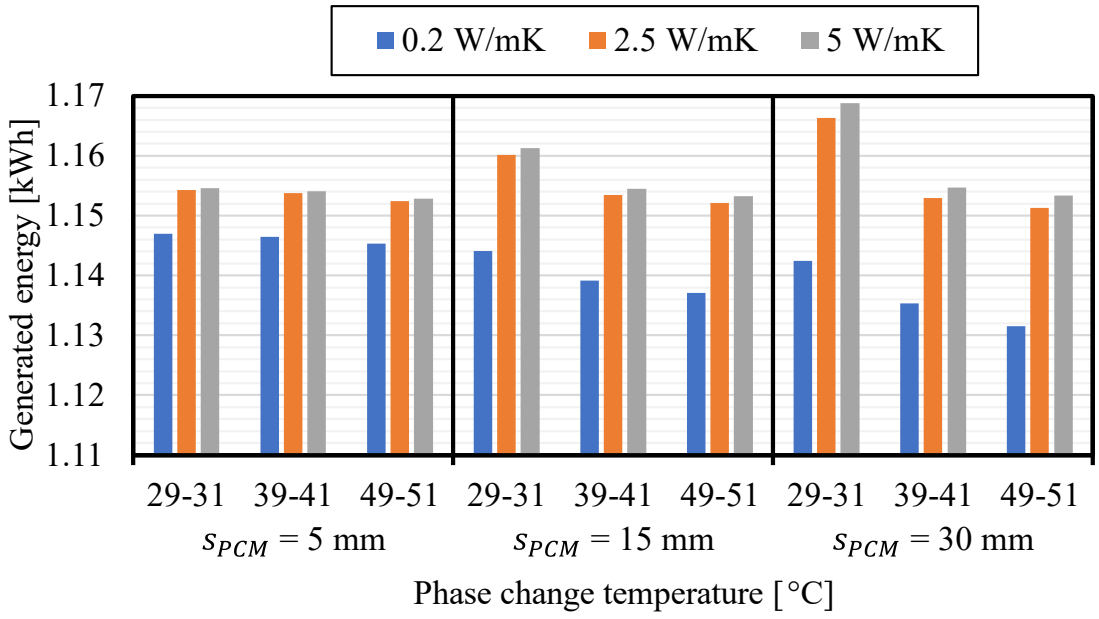

Figure 4-20: Parameter study results: generated electrical energy as a function of phase change temperature and thermal conductivity for three PCM foil thicknesses

It can be seen that the impact of the three considered parameters is most significant at the highest PCM layer thickness and is quite low for a thickness of only 5 mm. In fact, the difference between the highest and lowest energy yields for each thickness increases from 0.0093 kWh for s_{PCM} = 5 mm to 0.0373 kWh for s_{PCM} = 30 mm. This means that the benefit from an increased conductivity is greater when the PCM thickness is large. The same can be said for the phase change temperature, which only has a minor effect when the PCM thickness is small. However, it should be noted that the overall improvement potential is relatively low, as the generated electrical energy varies only between 1.132 kWh and 1.169 kWh, or 3.3 %.

Regarding the accumulated damage, Figure 4-21 shows that the combination yielding the highest amount of electrical energy also received the lowest damage. This result indicates that it is possible to design a heat sink that efficiently dampens temperature fluctuations while also producing a relatively high energy output. However, this can only be achieved with a sufficiently thick PCM layer. For thinner PCM foils, the increased conductivity causes comparatively large cell temperature fluctuations and thereby greater damage to the module. Also, for the smaller values of s_{PCM}, the phase change temperature appears to have a greater impact than it does for the thickest foil configuration. While the accumulated damage increases with higher phase change temperatures, a temperature range of 39-41 °C results in the lowest accumulated damage, with a minimum observed at a conductivity of 5 W/mK for the two lower thickness values.

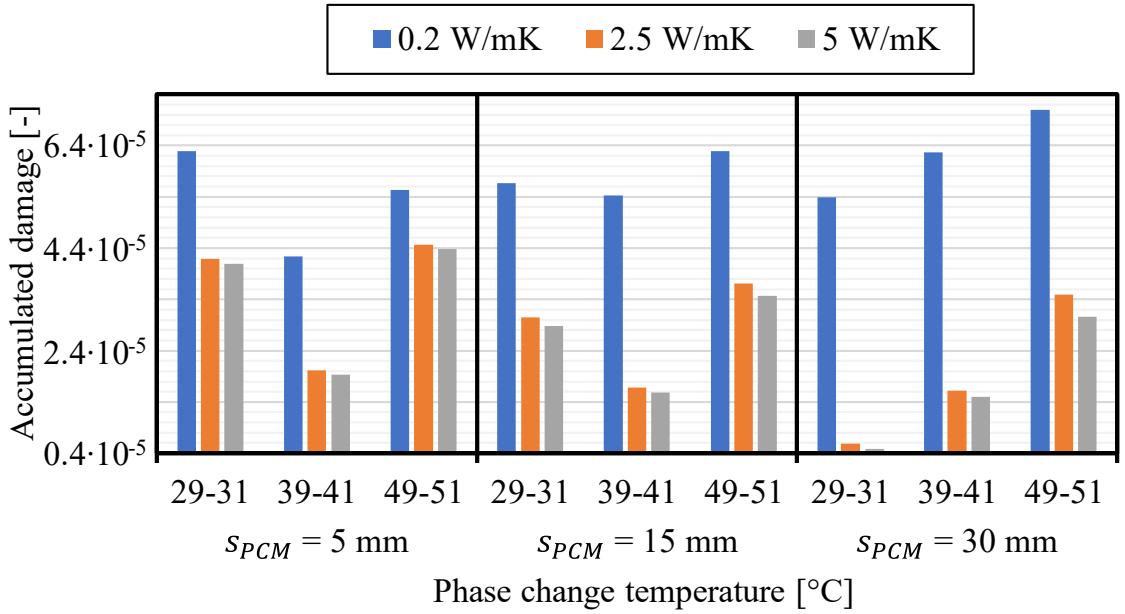

Figure 4-21: Parameter study results: accumulated damage D_{acc} as a function of phase change temperature and thermal conductivity for three PCM foil thicknesses

In terms of damage reduction potential, the parameter study revealed a much wider range for optimization compared to electrical power generation, with the highest observed damage value being more than 15 times higher than the lowest one. However, whether the additional investment cost of PCM with an improved conductivity (achieved by adding graphite or other additives) is outweighed by an increase in energy output and lifetime requires further investigation in future economic studies.

In conclusion, the parameter study revealed that the PCM heat sink configuration with a thickness of 30 mm, a conductivity of 5 W/mK and a phase change temperature at 29-31°C gave the best results in terms of both power generation and accumulated damage. This shows that a relatively high thermal conductivity outweighs the thermal insulation caused by a comparatively large PCM layer thickness. Even a conductivity of only 2.5 W/mK yields good results and offers a promising solution for PCM-enhanced PV modules while a conductivity of 5 W/mK seems unrealistically high. In case the PCM layer thickness is restricted to lower values due to economic or constructional constraints, the phase change temperature giving the best results was at 39-41 °C.

It should be noted that the parameter study was performed for only one day, July 2nd, 2019, which was a mostly sunny day with occasional cloud cover. For other days with different weather conditions, the results may look different revealing the challenge to design the optimal PCM heat sink that works well throughout the whole year. The most sensible design strategy would be to perform a detailed weather/climate analysis and to identify a "standard day" with weather conditions that are representative for the specific PV site location. Such a detailed analysis is very challenging and was not within the scope of this thesis. However, through this case study it could be demonstrated that the introduced thermal model of PCM-enhanced solar PV modules is applicable for studying different PCM heat sink configurations and identifying an optimal design once a detailed weather analysis has been completed.

4.8 Summary and conclusion

The first case study addressed the thermal modeling of PCM-enhanced solar PV modules. Based on the literature review given in section 4.1, the goals of this case study were defined as follows:

- To install an outdoor test site for collecting experimental data for at least one month, in collaboration with the Electrical Energy Technology department of Paderborn University
- To develop a thermal model of PV-PCM modules that includes a suitable correlation combination for the radiative and convective heat transfer coefficients, explicitly resolves the temperature of the solar cell, and produces a deviation of less than 2 K (6.25 %)
- To perform a parameter study of different PCM heat sink configurations and to evaluate the result based on generated electrical energy and received accumulated damage

All these goals could be achieved. A test site at the PV laboratory at Paderborn University described in section 4.3 was installed, and three different PV module configurations were tested: a reference module without PCM, a module with a smooth PCM foil attached to its back side and a module with a bubble wrap PCM foil attached to its back side. The measurements were carried out by the Electrical Energy Technology department during the month of July 2019. The experimental data revealed that even though the influence of the PCM foils on the cell temperatures is on average less than 1 K compared to the reference module, the thermal inertia of the PCM has a positive effect on the normalized electrical power.

The developed thermal model for PV-PCM systems outlined in section 4.4 showed an $RMSE$ of less than 2 K (6.25 %) for all three module configurations on four selected days in July 2019, which is an excellent result when compared to the error values of at least 3.2 K found in literature. The model is based on the implicit finite difference scheme outlined in Chapter 3, which was adapted to account for ambient weather conditions

through correlations determining the radiative and convective heat exchange at the top and bottom sides of the modules. To identify the best-fitting correlation combination, 16 different combinations for the sky temperature (required to determine the radiative heat transfer coefficient) and the convective heat transfer coefficient were tested. The combination yielding the highest accuracy was Sartori [63] / Kaplani & Kaplanis [64] for the convective heat transfer coefficient and Whillier [73] for the sky temperature.

With the validated thermal model, a parameter study was performed, in which three of the PCM heat sink parameters were varied in three steps resulting in a total of 27 different configurations. These parameters were the PCM layer thickness, the PCM phase change temperature and the PCM thermal conductivity. To evaluate the heat sink configurations, the electrical energy yield and the accumulated damage determined by the methods outlined in section 4.6 were considered. The analysis revealed that a heat sink with a large thickness and high thermal conductivity can greatly reduce thermal fatigue and slightly improve the electrical energy yield. Whether these positive effects outweigh the PCM investment cost, especially given the steep decline in PV module prices, needs further investigation.

Overall, the developed model for PV-PCM systems predicts their thermal behavior with high accuracy. It effectively captures changing weather conditions through boundary conditions and produces physically sound results. The model can be used to study further PCM heat sink configurations and is also applicable to conventional PV systems without PCM. It can be used to estimate the electrical energy yield for specific PV site locations, provided that correctly measured weather data is available.

5 Case study II: Packed bed latent heat storages

The second case study investigated the storage of thermal energy using PBLHS. An overview of current heat storage technologies with focus on latent heat storage systems is given. Packed bed heat storages based on macroencapsulated PCM are introduced and the state of the art regarding their modeling and optimization is presented, based on which the scope of this case study is formulated. The specific PBLHS system under investigation, along with two experimental setups designed and installed by a partner institute (Department of Energy - Building – Environment at Münster University of Applied Sciences) to collect validation data, is described. A model to simulate the thermal behavior of PBLHS is presented, and the validation steps are outlined. The results of a parameter study determining the packing density of new PCM capsule designs, which was carried out using a discrete element method (DEM), are discussed. The influence of the new capsule shapes on the heat storage capacity and thermal power output is evaluated based on the results of simulations performed with the validated PBLHS model.

5.1 State of the art

With a share of almost 50 %, heating and cooling contributed the biggest part to the global energy consumption and 40 % of annual CO_2 emissions in 2021 [81]. To accelerate the transition of the heating sector toward a sustainable state, renewable sources, such as solar and wind power, need to replace conventional energy sources like coal or gas. Since renewable energy sources tend to be highly volatile, efficient thermal storage technologies are required to smoothen the temporal fluctuations and to ensure a constant heat supply.

5.1.1 Thermal energy storages

Types of thermal energy storages (TES) can be categorized into three groups according to the underlying storage principal: sensible, latent and thermo-chemical heat storages, as illustrated in Figure 5-1.

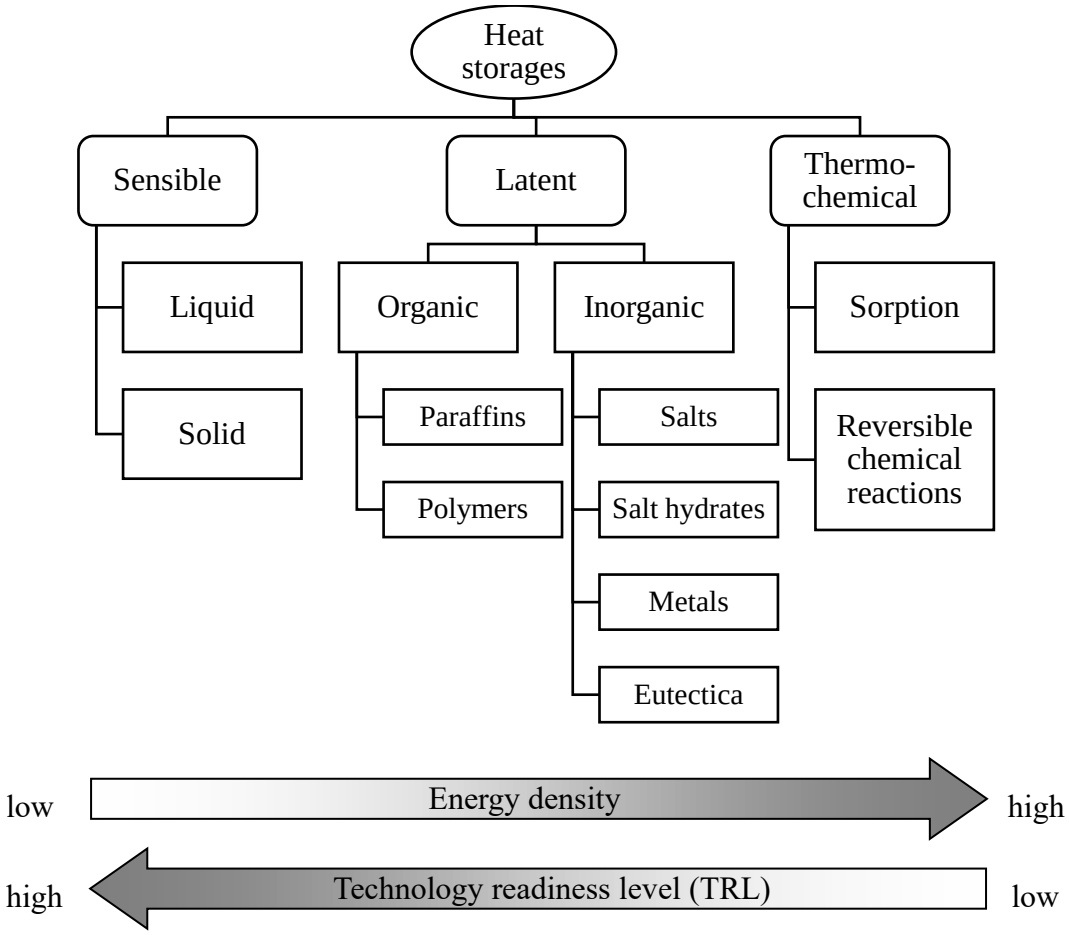

Figure 5-1: Overview of thermal storage technologies with focus on latent heat storages (adapted from [82])

5.1.1.1 Sensible heat storages

Sensible heat storages are the most common type of thermal storage and are used both in industrial and domestic applications [83]. In sensible heat storages, the stored amount of thermal energy depends on the temperature difference and the specific heat capacity of the storage material. Often, the storage material is a liquid, e.g., water or oil, but also solids, like sand, gravel and rocks or simply the envelope of a building are used as sensible heat storages [12]. In industrial processes requiring steam for heating purposes, water is also used in its gaseous state as storage material in steam accumulators [84].

Since space for storage tanks is often limited, both in industrial and domestic applications, it is desirable to use storage materials that have a high specific heat capacity and/or a high density resulting in a high volumetric heat capacity. Some materials that are commonly used for sensible heat storages are listed in Table 5-1.

Compared to latent and thermo-chemical heat storages, sensible storages usually have a lower volumetric heat capacity. Further, their application is limited to feasible temperature intervals, e.g., for unpressurized water it is 0 - 100 °C. However, in case the storage medium is a fluid, sensible storages can achieve very high charging and discharging rates, and thus, a high thermal power output, which is only limited by pumping power [13]. Solid sensible heat storages based on sand or ceramics often require a heat transfer fluid

(HTF), which transfers the thermal energy into or out of the storage [11]. This imposes an additional convective heat transfer resistance between the storage medium and the heat transfer fluid. However, solid sensible heat storages can achieve very high storage temperatures of up to 1600 °C [85]. Besides, sensible heat storages are well established, easy to operate and cost-efficient, which makes them the most common type of TES [10].

Table 5-1: Thermal properties and applications of common materials used in sensible heat storages [13]

Material	Temperature range [°C]	Specific heat capacity [kJ/kgK]	Density [g/cm³]	Applications
Water	0 - 100	4.2	0.96 - 1	Space heating, district heating
Thermal oil	0 - 400	1.6 - 2.1	0.85 - 0.9	Oil heaters
Molten salts	150 - 450	1.3	2.2 - 2.6	Concentrating solar-thermal power plants
Sand, gravel, rock	0 - 800	0.7	1.8 - 2	Soil thermal storages
Concrete	0 - 500	0.8 - 0.9	1.9 - 2.3	Building envelopes

5.1.1.2 Thermo-chemical energy storages

Thermo-chemical energy storages utilize the reaction energy of reversible chemical reactions. Also, adsorption- and absorption-based heat storages are often categorized as thermo-chemical, although the underlying principle is a physical effect [13]. A benefit of such storage concepts is the absence of heat losses during the storage period since energy is not stored by means of a thermal but rather of a chemical potential.

Adsorption is the accumulation of molecules at the surface of a solid, and often, porous medium. During this process, the kinetic energy of the molecules is converted into heat, which increases the temperature of the adsorbent (i.e., the porous medium). A common adsorption heat storage concept uses zeolite as adsorbent and water vapor as adsorbate [86]. Cold air containing water vapor is guided through the heat storage, where the water molecules adhere to the porous structure of zeolite. This process releases heat to and removes the vapor from the air stream. To recharge the zeolite storage, hot dry air is guided through the storage tank, evaporating and removing the water. The air flow exits the storage with a lower temperature containing water vapor. Such a storage concept could be used in combination with solar thermal energy generation or to utilize low temperature (< 140 °C) exhaust gas flows [87].

For absorption-based heat storages, salt, salt solutions, acids or brines are used as storage materials. Here, the absorbent is a liquid and the absorbate is a component of a gas flow. In practice, sodium hydroxide and water are often used as a working pair [88]. For charging, diluted brine is heated by a heat source, such as waste heat from industrial processes

or solar thermal collectors. During heating, water evaporates and the concentration of sodium in the brine is increased. For the discharging process, water vapor is mixed with the concentrated sodium hydroxide solution absorbing the water molecules, which leads to an increase in brine temperature. The resulting heat potential can be utilized by an appropriate heat exchanger. Due to the corrosiveness of the brine, special care must be taken when selecting the materials of the tanks and hydraulic components [82].

True chemical heat storages utilize reversible endothermal chemical reactions for charging and exothermal reactions for discharging. This storage concept usually involves a substance A and a substance B that are stored separately until a discharge is required by a process (for example, in case of a seasonal storage, heat release during winter). Both substances are brought together, and a chemical reaction is initiated, which produces a substance C and heat. During charging, heat is applied to drive the reaction in reverse, causing C to decompose back into its individual components, A and B. For both charging and discharging, catalysts are often required to increase the reaction rate [82].

5.1.1.3 Latent heat storages

Latent heat storage systems utilize the phase change of a PCM to store thermal energy. Compared to sensible heat storages, the temperature during charging and discharging stays constant for pure substances like water or mostly constant for mixtures. Generally, any substance, which has the desired phase change temperature for a specific application can be used as PCM in a latent heat storage.

In practice, different technological approaches can be found that make use of PCM for heat storage, as illustrated in Figure 5-2. Following Mehling & Cabeza [10], the design concepts of latent heat storages can be categorized according to how the thermal energy is absorbed/released:

- By exchanging the storage medium,
- At the surface of the storage unit itself,
- At surfaces within the storage unit.

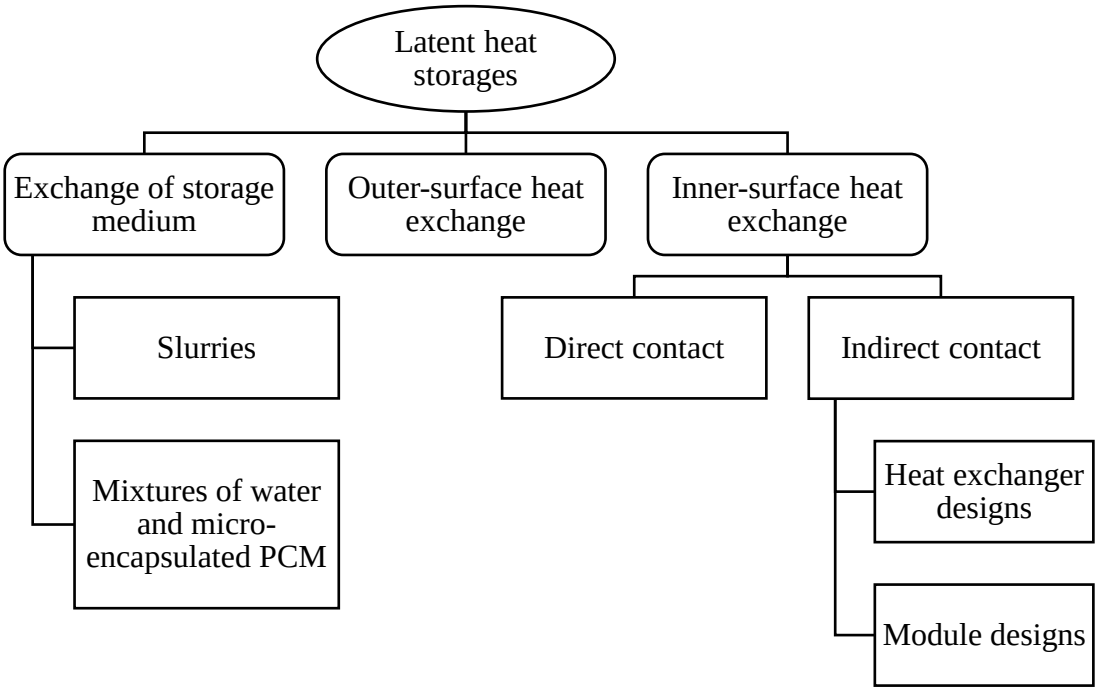

Figure 5-2: Overview and categorization of different latent heat storage technologies (according to [10])

The first method refers to mixtures, which contain a permanently liquid phase and a component that can undergo phase change. Examples of such mixtures include water-ice slurries or HTF mixed with microencapsulated PCM particles. The slurries are stored in a tank and are pumped through one or more heat exchangers connected to the heat demand side during discharge. The whole hydraulic circuit including the piping and other components containing the PCM-HTF-mixture (e.g., heat exchangers, buffer tanks) acts as thermal storage, leading to a large volumetric heat capacity. A disadvantage of this storage type is the high pressure drop due to the high viscosity of most slurries [10].

The second method is limited to situations where only low thermal power output is required and the main purpose of the PCM is to maintain a certain operating temperature in a well-insulated environment [11]. Such applications include the cooling/heating of food or beverages by thermal packs, or heat sinks for electronic components.

The third method is the one on which most latent heat storages are based on. Here, the heat transfer occurs inside the storage at surfaces that separate the PCM and the HTF. Such surfaces are either created by direct contact between the PCM and the HTF forming an interface or they are part of an additional material such as pipes or encapsulation materials (indirect contact). In case of the direct contact type latent heat storage, PCM and HTF are in direct contact. To prevent mixing of the two substances, the PCM must not be soluble in the HTF [11]. As opposed to the indirect contact storage type, no separating materials such as pipes or plates causing additional thermal resistance are needed. The energy density of this storage type is generally high since the storage tank is almost completely filled with PCM. Also, enhanced convection and a large interfacial area between PCM and HTF ensure a high thermal power output. A drawback of the direct contact type

is the entrainment of liquid PCM droplets by the HTF, which can cause serious fouling in heat exchangers and pumps, resulting in high maintenance [12].

Latent heat storage concepts based on the indirect contact type are the most common ones. Here, a further distinction with respect to how the PCM is integrated into the storage can be made. In heat exchanger type storages, the PCM is located in the outer volume of the storage tank, e.g., the mantle volume in case of a shell-and-tube design, while the HTF flows through pipes or plates. In module type latent heat storages, PCM-filled capsules (i.e., the modules) are located in a storage tank, while the HTF fills the remaining tank volume. Examples for the latter type are PBLHS and plate type storage systems making use of PCM-filled plate-like capsules such as the ones shown in Figure 2-4, left. For both indirect storage types, the energy storage density and the specific heat transfer area determining the thermal power are crucial parameters. Heat exchanger type storages can achieve storage densities of up to 95 % (i.e., 95 % of the internal storage volume is PCM), however, at the cost of thermal power due to a lower specific heat transfer area [11]. Module type storages, on the other hand, sacrifice some storage density for an increased surface area. In a packed bed filled with spherical capsules, for example, the maximum packing density is 74%, which corresponds to the densest possible spherical packing.

Module type latent heat storages, and especially PBLHS, represent an interesting option for integration into existing heating or cooling systems. Since additional PCM capsules can easily be inserted into conventional sensible heat storages such as hot water tanks, they are suitable for retrofitting projects. Further, storages based on encapsulated PCM can relatively easily be upscaled through additional modules. The production of PCM capsules, e.g., through blow molding, and their transportation are also straightforward, which makes the module type storage a suitable choice for domestic and small scale industrial off-the-shelf solutions [10].

5.1.2 Modeling of packed bed latent heat storages

PBLHS comprise a tank containing a fixed packed bed that consists of PCM capsules, as shown in Figure 5-3. In most cases, the geometry of the capsules and the PCM inside them do not vary within one storage system. The encapsulation material is usually either metal or plastic. The storage volume that is not occupied by the packed bed is filled with HTF, which is often water but may also be a thermal oil for high-temperature or a water-glycol mixture for cooling applications. The tank has at least one inlet and one outlet, which can usually be hydraulically switched to be able to control the flow direction of the HTF (typically charging with hot fluid from the top and discharging with cold fluid from the bottom of the tank).

An essential quantity of a packed bed is its porosity ϕ, which is defined as the ratio of the void volume V_v and the total volume V_t occupied by the bed. Assuming that the porosity is homogenous across the bed, it can also be expressed in terms of the cross-sectional areas of the voids A_v and the tank A_t:

$$\phi = \frac{V_v}{V_t} = \frac{A_v}{A_t} \tag{5.1}$$

The porosity affects the fluid flow through the bed, as it determines the available cross-sectional area. Due to mass conservation, with decreasing porosity, the fluid velocity increases, since a larger part of the total cross-sectional area is occupied by the packed elements. The flow velocity inside the voids u_v is determined by:

$$u_v = \frac{u}{\phi} = \frac{\dot{m}}{\rho \phi A_t} \tag{5.2}$$

where u is the free flow velocity (i.e., the velocity the fluid would have if there were no packed elements present inside the tank) and $\dot{m}$ is the mass flow.

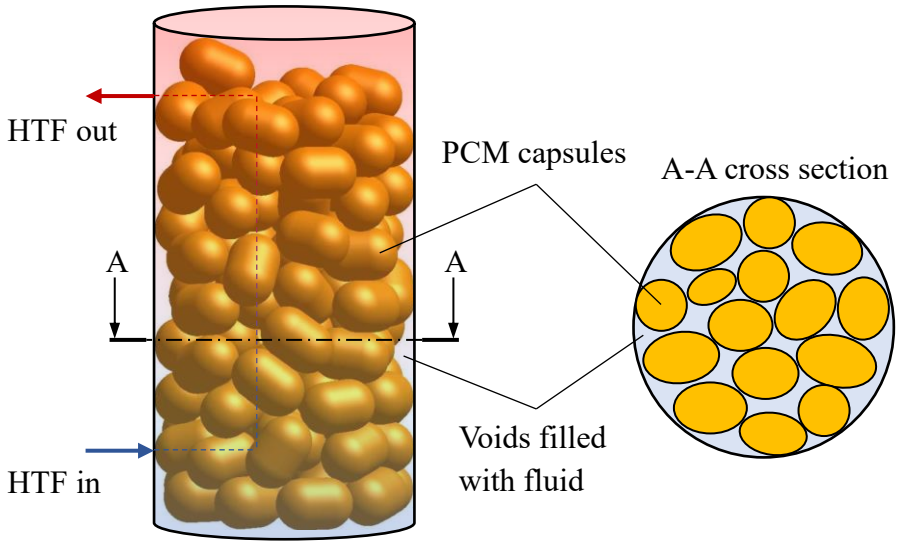

Figure 5-3: Schematic of a PBLHS filled with non-spherical PCM capsules (adapted from [89])

Compared to sensible hot water storages, which are still the most common type of heat storage for domestic applications, the design process and operational control of PBLHS are more challenging due to the phase change, during which the temperature is no longer an indicator of the storage charging level. Therefore, appropriate modeling approaches need to be identified for predicting the transient behavior of PBLHS especially during their charging and discharging periods.

Existing thermal modeling approaches can be distinguished by the way the heat transfer between the bed and the HTF is treated. Following a review on different numerical PBLHS simulation approaches by de Gracia & Cabeza [90], they can be divided into two groups: single-phase and two-phase models, as shown in Figure 5-4. Additionally, due to the steady increase of computational capacities, fully resolved 3D CFD simulations using commercial software tools are becoming an interesting alternative to study local phenomena inside the PBLHS. However, even packed beds consisting solely of spheres are quite challenging to simulate with CFD methods, since pre-processing and meshing can be very time-consuming. If the thermal behavior of different packed bed configurations is to be

investigated, the packed beds themselves have to be generated first, which requires the use of discrete element methods or rigid body simulations. For these reasons, CFD methods are usually unsuitable for optimization studies of PBLHS, which is why they were not considered for this case study. Instead, the focus was set on less complex approaches based on the single-phase and two-phase models.

Single-phase models consider the whole packed bed as one porous domain described by a single governing equation. The underlying assumption is that any change in temperature occurs instantaneously in both the HTF and the bed meaning that they are considered to be in a state of thermal equilibrium. According to Ismail & Stuginsky [91], this assumption holds true for systems in which the fixed bed has high thermal conductivity and heat capacity in comparison to the HTF. This is usually not the case for PBLHS based on macroencapsulated PCM, as the thermal conductivity of PCM is low (< 1 W/mK). He et al. [92] point out that single-phase models can be used for cases in which the PCM particles are very small or granular, since the heat capacity of one individual particle is low. For this case study, which investigated PBLHS based on macroencapsulated PCM, however, single-phase models are not suitable.

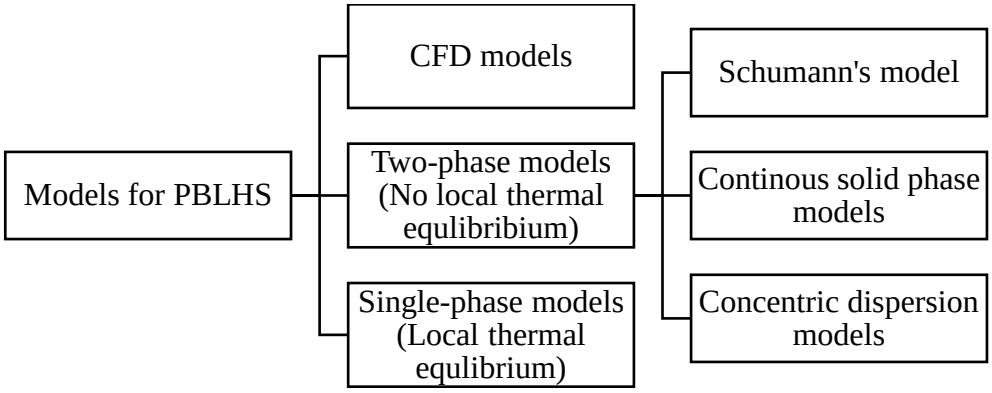

Figure 5-4: Classification of thermal models for PBLHS (adapted from [92])

Two-phase models treat the involved phases – the packed bed and the HTF – individually, with one governing equation for each phase. These approaches differ by how heat conduction is treated in each phase. In order of increasing complexity, they can be divided into models based on Schumann's approach [93], continuous solid phase models and concentric dispersion models. Schumann's model neglects thermal conduction in both phases. Further, it only considers the axial direction and was developed for a liquid flowing through a duct filled with a porous medium. The corresponding governing equation for the HTF reads:

$$\phi\left(\rho c_p\right)_{HTF}\frac{\partial T_{HTF}}{\partial t}+\left(\rho c_p u\right)_{HTF}\frac{\partial T_{HTF}}{\partial x}=h_{HTF-PB}a_{PB}(T_{PB}-T_{HTF})+S_{HTF} \qquad (5.3)$$

The governing equation for the solid only accounts for the accumulation of heat caused by the convective heat exchange with the HTF:

$$(1-\phi)\left(\rho c_p\right)_{PB}\frac{\partial T_{PB}}{\partial t}=h_{HTF-PB}a_{PB}(T_{HTF}-T_{PB})+S_{PB} \qquad (5.4)$$

In both equations the subscripts HTF and PB refer to the HTF and the packed bed, respectively. The heat transfer coefficient h_{HTF-PB} accounts for the heat transfer between the HTF and the packed bed across the specific surface area of the bed a_{PB} (in m²/m³). Note, that u_{HTF} refers to the free flow velocity of the HTF.

In its original form, Schumann's model cannot accurately capture the heat transfer in PBLHS, since it does not account for spatial temperature gradients within the PCM capsules. However, the temperature distribution within the individual capsules is crucial for predicting the charging and discharging behavior of the storage. For this reason, Regin et al. [94] modified Schumann's approach by incorporating the transient evolution of the thermal resistance within the PCM during phase change into the heat transfer coefficient. They investigated the thermal response of a storage system based on spherical PCM capsules by varying different parameters such as flow rate, capsule size and melting temperature range. Their approach is widely cited in literature due to its simple implementation, even though no validation against experimental data was provided by the authors.

Continuous solid phase models treat the packed bed as one continuous phase instead of a medium comprised of individual particles. As opposed to Schumann's model, heat conduction is considered in both phases and can be accounted for in both axial and radial directions. However, if the thermal conductivity of the continuous solid phase is not constant with respect to space, a lumped modeling approach is required. The governing equation for the HTF and the continuous solid phase are given (for simplicity in axial direction only) as [95]:

$$\phi\left(\rho c_p\right)_{HTF}\frac{\partial T_{HTF}}{\partial t}+\left(\rho c_p u\right)_{HTF}\frac{\partial T_{HTF}}{\partial x} = \phi\frac{\partial}{\partial x}\left(k_{HTF}\frac{\partial T}{\partial x}\right)+h_{HTF-PB}a_{PB}(T_{PB}-T_{HTF})+S_{HTF} \tag{5.5}$$

$$(1-\phi)\left(\rho c_p\right)_{PB}\frac{\partial T_{PB}}{\partial t} = (1-\phi)\frac{\partial}{\partial x}\left(k_{PB}\frac{\partial T_{PB}}{\partial x}\right)+h_{HTF-PB}a_{PB}(T_{HTF}-T_{PB})+S_{PB} \tag{5.6}$$

The lumped bed conductivity k_{PB} accounts for the fact that the packed bed does not represent just one single continuous phase but comprises individual PCM capsules. It considered effects such as contact thermal resistance between the capsules, varying conductivities of the encapsulation material and the PCM and, in some cases, radiative heat exchange between the individual capsules [91].

The main advantage of the continuous solid phase model is the ability to take the radial direction into account, which allows to consider varying porosity profiles and heat losses to the environment across the storage walls. Similar to Regin et al. [94], Bellan et al. [96] suggested a continuous solid phase model with the phase change process incorporated into the heat transfer coefficient, which accounts for the changing thermal resistance due to the movement of the phase front. Their 2D packed bed model of spherical PCM capsules arranged as a rhombic packing, which was described in a series of papers [96–98], appears very comprehensive as it takes varying radial porosity, varying axial flow

velocities and natural convection effects within the liquid PCM via an effective conductivity approach into account. They solved their model equations numerically and compared the results to experimental data. A good agreement between the simulations and experiments was achieved, albeit by using fitting parameters. Regarding the computational effort, 2D continuous solid phase simulations have been reported to take a considerably longer time than Schumann's and concentric dispersion models [91].

The concentric dispersion model treats the packed bed particles as individual elements and accounts for thermal conduction in both the HTF and the individual particles. Within these elements, all relevant heat transfer processes are captured by a corresponding governing equation. Since in literature most PBLHS are based on spherical PCM capsules, the energy conservation equation is given in spherical coordinates, while the governing equation for the HTF is similar to that of the continuous solid phase model (i.e., Eq. (5.5)):

$$\begin{aligned}\phi\left(\rho c_p\right)_{HTF}\frac{\partial T_{HTF}}{\partial t}+\left(\rho c_p u\right)_{HTF}\frac{\partial T_{HTF}}{\partial x}\\ =\phi\frac{\partial}{\partial x}\left(k_{HTF}\frac{\partial T}{\partial x}\right)+h_{HTF-PB}a_{PB}(T_{PB}-T_{HTF})+S_{HTF}\end{aligned} \tag{5.7}$$

$$\left(\rho c_p\right)_{PB}\frac{\partial T_{PB}}{\partial t}=\frac{1}{r^2}\frac{\partial}{\partial r}\left(k_{PB}r^2\frac{\partial T_{PB}}{\partial r}\right)+S_{PB} \tag{5.8}$$

Eq. (5.8) represents the heat conduction equation in spherical coordinates with an additional source term (see also Appendix A1). Eq. (5.7) and Eq. (5.8) are coupled by a boundary condition at the outer surface of the PCM capsules (where $r = R_C$):

$$k_{PB}\frac{\partial T_{PB}}{\partial r}\Big|_{r=R_C}=h_{HTF-PB}(T_{HTF}-T_{PB}) \tag{5.9}$$

Figure 5-5 illustrates some of the different heat transfer phenomena occurring during melting inside and at the surface of a spherical PCM capsule that are usually considered within the concentric dispersion approach. Thermal conduction determines the movement of the phase front indicated by $R_{Int}(t)$. Further, natural convection inside the liquid PCM influences the heat transport from the capsule wall to the solid PCM. Often, the effect of natural convection is incorporated into the thermal conductivity using an effective thermal conductivity approach (e.g., in [99]). In addition, convective heat transfer takes place at the outer surface of the capsule, by either natural, forced or mixed convection.

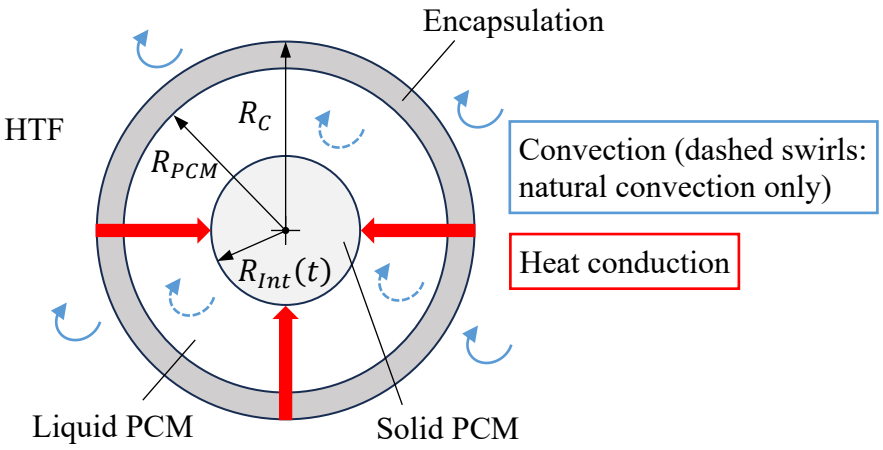

Figure 5-5: Heat transfer processes inside and at the surface of a spherical PCM capsule during melting

Eq. (5.8) can be adapted based on the specific method for solving phase change problems, some of which are discussed in section 2.5.2. For example, Ismail & Henríquez [100] applied a variable grid method to predict the position of the solid-liquid interface inside PCM capsules filled with water (or water ice, respectively). The authors validated their model against experimental data and simulated the thermal response of their storage system to varying flow rates and different encapsulation materials. Foudhil et al. [101] applied an apparent heat capacity approach (see equations (2.61) and (2.62)) based on a fixed grid and validated their model against experimental data. Other authors employed the enthalpy method (see equations (2.63) - (2.65)) to model the phase change of the PCM [99,102]. An interesting study by Karthikeyan & Velraj [103] compared the three different modeling approaches for PBLHS (Schumann's model, continuous solid phase model and concentric dispersion model) employing the enthalpy method. They used explicit finite differences as solution technique and found that only the concentric dispersion model produced acceptable results when compared to experimental data.

Based on the analysis of different modeling approaches for heat transfer in packed beds in general, and PBLHS in particular, the concentric dispersion model was chosen for this case study. It appears obvious that the thermal gradients within the packed bed elements, i.e., the macroencapsulated PCM capsules used in this study, are crucial to predict the thermal response of the storage. Such detailed resolution of the thermal processes inside the PCM capsules enables a more accurate prediction of the storage behavior without relying on lumped quantities or fitting parameters. Moreover, the convective heat transfer from HTF to the bed can effectively be modeled using Nusselt correlations to determine h_{HTF-PB}. Such correlations are readily available for various operating conditions and can be found in sources such as [4,10,90,104], and others. Lastly, the concentric dispersion approach allows the incorporation of the phase change process directly into the source term S_{PB} in Eq. (5.8), enabling the use of the solution algorithm presented in Chapter 3, which is based on the source term method.

5.2 Scope of the case study

In addition to predicting the thermal behavior of PBLHS, the second focus of this case study was on optimizing these systems to enhance their thermal performance. A thermal storage should have:

- a high volumetric storage capacity (also referred to as energy density),
- a high thermal power output,
- other preferential characteristics (e.g., low pressure drop, no toxic and flammable media, cost efficient hydraulic equipment, low maintenance cost, long economic life span, etc.).

The first point addresses the question of how much energy can be stored per unit of volume, while the second one is focused on how quickly this energy can be released/absorbed. As this case study aimed for the optimization of the thermal performance, the aspects mentioned under the third point are not discussed further.

Along with physical properties such as specific heat capacity and latent enthalpy, the energy density of the PBLHS is determined by the packing density of the packed bed, which, in turn, depends on the shape of the PCM capsules. The packing density ε is ratio of the volume of the packed elements and the total packed bed volume and is linked to the porosity:

$$\varepsilon = \frac{V_{PB}}{V_t} = 1 - \phi \tag{5.10}$$

Studies considering the packing density of different geometrical bodies were performed, e.g., by Delaney & Cleary [105] and Zhao et al. [106]. They investigated the packing properties of so-called superellipsoids, which are described in more detail in section 5.6.

To identify different enhancement strategies for PBLHS with respect to thermal power output, it is worth taking a look at Eq. (5.9) again. Five factors that influence the heat flow between the interior of the PCM capsule and the HTF can be identified:

- the thermal conductivity k_{PB},
- the thickness of the PCM capsules (R_C for spherical capsules),
- the heat transfer coefficient h_{HTF-PB},
- the specific heat transfer area a_{PB}, and
- the temperature difference between the bed and the HTF.

The latter factor depends on the operating conditions of the storage system and is usually predetermined by external factors such as the availability of high-temperature heat sources or the temperature level on the demand side. The specific thermally active surface area a_{PB}, on the other hand, is almost exclusively influenced by the geometric shape of

the packed bed elements. To a certain extent, it may be influenced by the packing arrangement of the elements (flat surface contacts between the packed elements and HTF recirculation zones might reduce a_{PB}). The heat transfer coefficient is influenced by both the geometry of the packed elements and the operating conditions of the PBLHS system such as flow rate and the temperature difference between the bed and the HTF. In addition to the heat transfer taking place at the boundary, the thermal resistance inside the PCM capsules influences the PBLHS performance. To reduce the resistance within the capsules, their thickness can be reduced (flat shapes melt/solidify faster compared to bulky ones). Additionally, the typically low thermal conductivity of PCM can be enhanced by adding particles of a highly conductive material such as graphite or nanoparticles, albeit at the expense of specific latent heat. Further, the conductive particles need to be fixed within the PCM compound using thickeners to avoid separation, which are not available for all temperatures.

In summary, the main optimization potential lies in the shape of the PCM capsules, which affects the active heat transfer area, the capsule thickness, the packing and hence the energy density, as well as the heat transfer coefficient. Consequently, the specific optimization goals for PCM capsules were derived:

- In order to maximize the energy density of the PBLHS, the capsules should have a geometry that enables high packing densities.
- At the same time, their geometry should minimize the inner thermal resistance and enable a large heat transfer area to maximize the thermal power output of the PBLHS.

The state of the art regarding the shape of PCM capsules for PBLHS appears to be that spherical or near-spherical capsules are used in most numerical and experimental studies. In fact, almost all of the literature sources cited in the previous section describe studies using spherical capsules. While spheres can achieve rather high packing densities – up to 74 % for the densest possible packing – they also have a major disadvantage: their surface-area-to-volume ratio (SVR) is the lowest among all geometrical bodies. This not only has a negative effect on the heat transfer rate at the capsule surface, but also leads to a high internal thermal resistance. A non-spherical body with the same volume as a sphere is always “thinner” in the sense that the minimum distance from its center to its surface is smaller than that of a sphere (which is the sphere’s radius). Since the net thermal resistance is determined by the length of the conducting material, PCM spheres need a much longer time to fully change their state than other geometries. Therefore, simply increasing the surface area of the PCM capsule is not sufficient - the overall topology has to be adapted as well. For example, a golf ball has a considerably larger surface area than a perfect sphere, yet the inner thermal resistance of these two objects is quite similar.

To improve the thermal performance of PBLHS, capsule geometries that deviate from the spherical design were investigated in this case study regarding their thermal power and energy density. The goal was to find a capsule shape that achieves packing densities similar or close to that of spheres, while enabling a higher thermal power output. To reach this goal, the following steps were performed:

- Development of a thermal model of PBLHS containing non-spherical PCM capsules aiming at an accuracy of at least 90 % when compared to experimental data
- Geometrical parameter study of different PCM capsule geometries based on superellipsoids with respect to SVR and packing density, performed using DEM filling simulations
- Application of the PBLHS model to new, promising capsule designs evaluating their energy density and thermal power

These steps are described in detail in the following sections.

5.3 System description and experimental setup

The investigated PBLHS systems are two different experimental setups located at Münster University of Applied Sciences. The first system is based on a cuboid storage tank, and was designed and installed by Linnemann [107]. With this experimental setup, Richter [108] conducted experiments using lenticular PCM capsules. The second system is based on a cylindrical tank filled with cylindrical capsules, and was designed and installed by Richter [109]. The goal of the experiments was to study the charging and discharging behavior of the PBLHS under varying operating conditions and with different PCM capsule designs. Parts of the content of this chapter are taken from the works of Linnemann [107] and Richter [108–110].

The first PBLHS comprises a cuboid steel tank with a quadratic cross section shown in Figure 5-6, left, that was filled with a structured packed bed consisting of lenticular PCM filled capsules. An illustration of the lenticular capsule design is shown in Figure 5-7, left.

Figure 5-6: Cuboid storage tank (left, [108]) and a PBLHS filled with cylindrical heatStixx (right, illustration by Axiotherm GmbH [111])

The second PBLHS consists of a cylindrical storage tank filled with randomly packed, cylindrical PCM capsules that are shown in Figure 5-7, right. An illustration of a storage tank filled with such cylindrical capsules is shown in Figure 5-6, right.

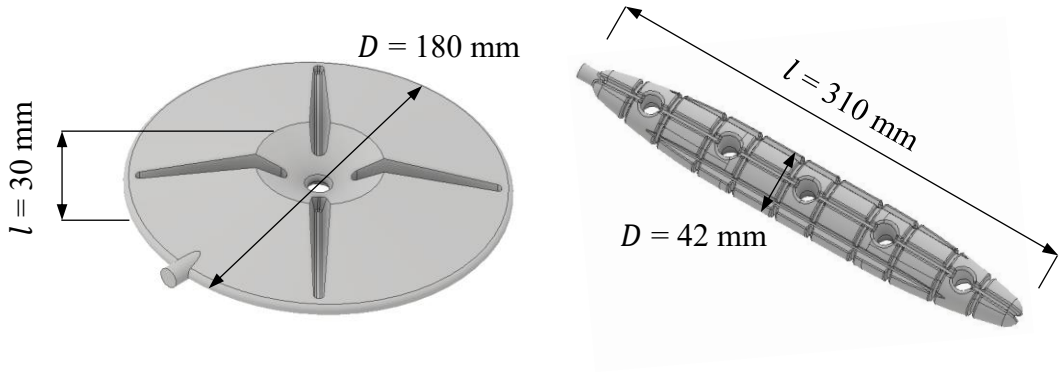

Figure 5-7: Investigated capsule designs based on the heatSel (left) and the heatStixx (right) by Axiotherm GmbH

Both investigated capsule designs are based on former designs by Axiotherm GmbH of the heatSel and the heatStixx. Their geometric characteristics are listed in Table 5-2.

Table 5-2: Geometrical characteristics of HeatSels and HeatStixx derived from CAD data

		HeatSel	HeatStixx
Nominal diameter	[mm]	180	42
Nominal length	[mm]	30	310
Wall thickness	[mm]	1	
Surface area	[m²]	$61.49 \cdot 10^{-3}$	$45.30 \cdot 10^{-3}$
Volume	[ml]	352.2	275.1
SVR	[m^{-1}]	174.6	164.6

Both PBLHS experimental setups are based on steel tanks (one cuboid and one cylindrical) with an HTF inlet at the top and an outlet at the bottom. The inlet and outlet of the cuboid storage consist of perforated pipes ensuring an even fluid distribution. These fluid distributors are separated from the packed bed by steel grates. An additional grate was installed in the middle of the tank to ensure mechanical stability, resulting in one packed bed in the bottom and one packed bed in top half of the storage tank. Each bed consisted of 475 heatSels, which were arranged in a structured pattern shown in Figure 5-8. The bed porosity resulting from this arrangement was 0.47.

Figure 5-8: First two layers of heatSel arrangement inside the cuboid storage tank [108]

Pt100 temperature sensors were located at the inlet and outlet as well as at a distance of approximately 35 cm from the inner tank wall at around half the bed height. A schematic of the cuboid tank with relevant dimensions is shown in Figure 5-9.

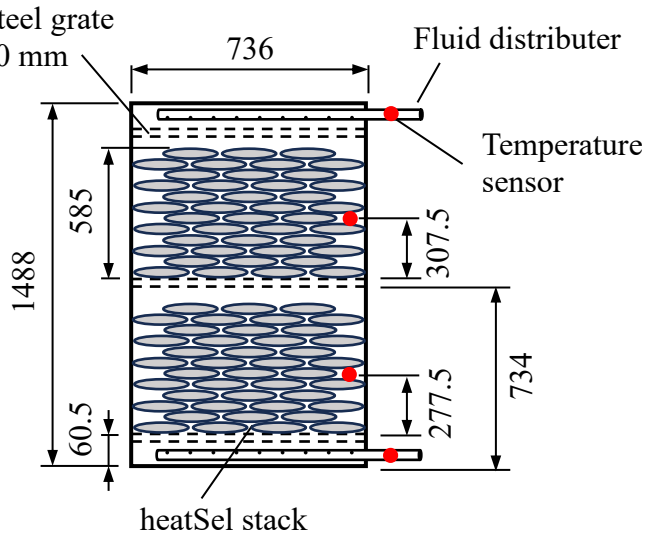

Figure 5-9: Schematic of the cuboid storage setup containing two structured packed beds comprised of HetSels together with relevant dimensions (in mm)

The second investigated PBLHS system consists of a cylindrical tank filled with 1466 randomly packed heatStixx and is illustrated in Figure 5-10. The general setup is simpler compared to the cuboid storage tank as no separating grate was installed in the middle of the tank, resulting in a single packed bed that filled almost the entire internal volume of the storage. Only a small, perforated steel plate was positioned at the top of the storage to separate the bed from incoming piping. The bed porosity of this setup was 0.55. Temperature sensors were located at the inlet and outlet as well as at half the tank height at a distance of around 35 cm from the inner tank wall. The properties of both storage tanks are summarized in Table 5-3.

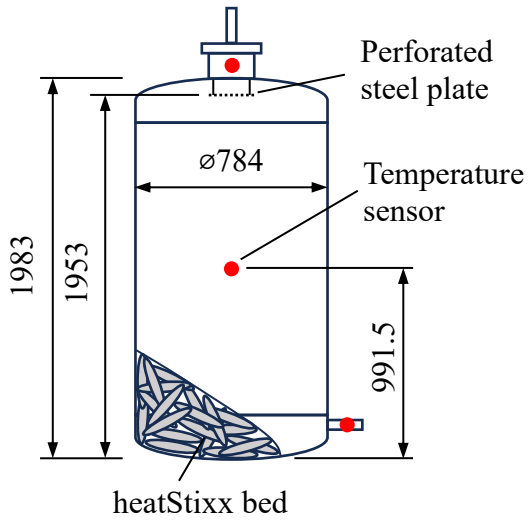

Figure 5-10: Schematic of the cylindrical storage setup filled with randomly packed heatStixx together with relevant dimensions (in mm)

Table 5-3: Dimensions and properties of the storage setups used in the experiments

		Cuboid tank	Cylindrical tank
Height	[m]	1.454	1.983
Inner side length / diameter	[m]	0.736	0.784
Packed bed height	[m]	2 x 0.585	1.953
Number of capsules	[-]	2 x 475	1466
Porosity	[-]	0.47	0.55

The PCM used in both setups was ATS 58 by Axiotherm, which has a solidus temperature of 56.4 °C and a liquidus temperature of 58 °C in case of melting and a solidus temperature of 54.8 °C and a liquidus temperature of 56.6 °C in case of solidification, which means the PCM has a slight hysteresis tendency (see also Figure 2-5). The encapsulation material for both the heatSel and heatStixx was PP, and in both setups the HTF was water. The thermal properties of all involved substances are listed in Table 5-4.

Table 5-4: Thermal properties at 58 °C of materials and HTF used in the experiments

			ATS58	PP	Water
Thermal conductivity	solid liquid	[W/mK]	0.4 0.35	0.21	0.65
Density	solid liquid	[kg/m³]	1450 1260	900	984.7
Specific heat capacity	solid liquid	[J/kgK]	2120 2970	1989	4181.8
Latent heat		[kJ/kg]	200	-	-

The experimental data was collected in multiple runs with different operating conditions (mainly inlet temperature and mass flow rate). In each individual experimental run, the mass flow rate and the inlet temperature were kept constant.

The experimental procedure was as follows: a run was started when an even temperature distribution prevailed across the tank, which was the case when the inlet and outlet temperature sensors showed the same value (within around ± 0.5 K). Then, the mass flow rate was adjusted to the desired value. Next, the water heater was set to the desired inlet temperature, which was below the phase change temperature in case of discharging and above the phase change temperature in case of charging. Inlet temperature and mass flow rate were kept constant until a uniform temperature distribution throughout the storage tank was achieved, which was indicated by the outlet temperature being similar to the inlet temperature again. Subsequently, the next run could be started by setting a new inlet temperature and flow rate.

The flow direction of the HTF was adjusted accordingly depending on the process (charging or discharging). During the charging process, which was usually the first part of an experimental cycle, cold HTF entered the storage tank at the bottom. During the discharging process, hot HTF was pumped into the storage at the top. In this way, natural and forced convection followed the same flow direction, allowing a sharp temperature front inside the tank.

5.4 Thermal model for packed bed latent heat storages

The developed model for predicting the thermal response of PBLHS systems is based on the concentric dispersion approach (Equations (5.7) - (5.9)), which is detailed in section 5.1.2., along with the source term method introduced in section 2.5.2. The applied solution method for handling the phase change processes within the PCM capsules is outlined in Chapter 3. Some modifications to the basic concentric dispersion model were necessary in order to account for PCM capsule geometries such as those shown in Figure 5-7 that deviate from the spherical design.

An approximation of the two experimental storage setups described in the previous section is shown in Figure 5-11. The thermal PBLHS model is based on the following assumptions:

- The storage tank is perfectly insulated (i.e., no heat losses to the ambient).
- There are no temperature gradients in radial direction, and only heat transfer in the axial direction is considered.
- The effect of natural convection inside the liquid PCM is neglectable due to its high viscosity.
- The PCM capsules can be approximated by spherical shells. The approximation procedure is detailed in the following section.
- The packed bed has a homogenous porosity and its whole surface area is thermally active (ignoring potential local recirculation and flat surface contacts).
- Charging occurs from top to bottom and discharging from bottom to top, i.e., in the direction of natural convection.
- Thermal effects of tank internals, possible pockets of air inside the PCM capsules, heat conduction through capsule contact and radiation are negligible.
- Properties of the HTF, the encapsulation material and the PCM are temperature-independent.

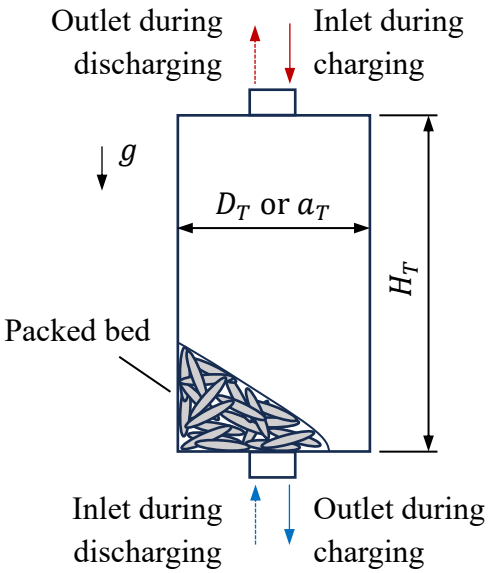

Figure 5-11: Schematic of the PBLHS described by the thermal model: storage tank defined by height H_T and diameter D_T (cylindrical tank) or side length a_T (cuboid tank)

5.4.1 Treatment of non-spherical PCM capsule geometries

While the concentric dispersion model assumes spherical packed bed elements, the PCM capsules investigated in this case study had various geometries, which were non-spherical. Therefore, the non-spherical capsules had to be approximated in a way that preserves

their integral geometric characteristics. At first glance, it seems reasonable to simply approximate a non-spherical PCM capsule as a sphere with the same PCM volume. The diameter of the resulting sphere would be relatively small. The problem that arises is that the surface area of the resulting sphere is smaller than that of the original capsule. This greatly decreases the modeled heat transfer rate between the capsule and the HTF, which leads to unrealistically high phase change durations. A more suitable alternative is to keep the surface area of the model sphere equal to that of the real PCM capsule resulting in a sphere with a relatively large diameter. An illustration of the two approximation approaches is shown in Figure 5-12.

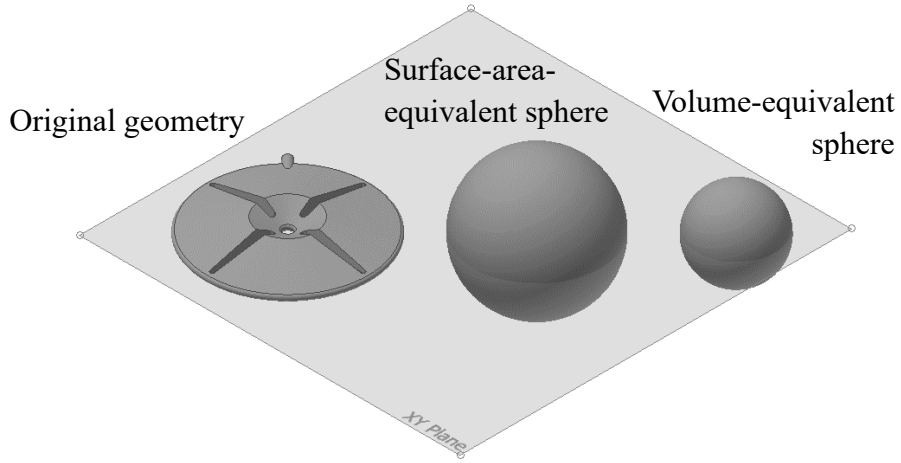

Figure 5-12: Approximation approaches for a non-spherical PCM capsule (adapted from [112])

The surface-area-equivalent sphere contains a PCM volume that is much larger than that of the original capsule geometry. To address this discrepancy and to generate a spherical approximation, which has both the same volume and the same surface area as the original capsule, a spherical shell model was introduced by Grabo et al. [112]. The structure of the spherical model shell is illustrated in Figure 5-13. As shown there, the PCM volume is evenly distributed around an empty core region, which is considered thermally inactive. The thickness of the encapsulation remains the same as in the original geometry (1 mm for the PCM capsules considered in this case study). The main advantage of the spherical shell approximation lies in its simplicity and versatility. Moreover, it maintains two key characteristics of the original PCM capsule geometry, i.e., the surface area and the PCM volume.

In theory, this approximation should also be applicable to sensible packed bed heat storages filled with gravel, rock or other materials, since the geometrical parameters that influence their thermal performance – the surface area and volume of the packed elements – are the same as for PBLHS. In this case, no encapsulation is included, and the shell domain consists only of the sensible storage material. The only requirement for the application of the spherical shell approximation on sensible packed bed heat storages is that the packed elements have a uniform size and shape.

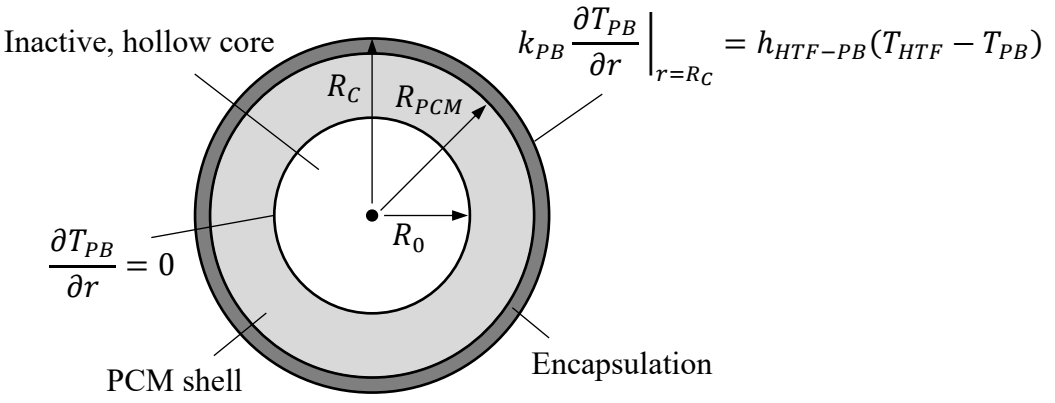

Figure 5-13: Spherical shell approximation of non-spherical PCM capsules as well as boundary conditions used in the developed concentric dispersion approach

The main limitation of the spherical shell approximation becomes apparent, when geometries with a large number of surface extensions, that are small in size compared to the overall length scale of the capsule, are considered. This is the case with the golf ball geometry already mentioned above. The approximation of such a shape that features many small dimples, would result in a shell with a very large radius, leading to an unrealistically thin PCM layer, which in turn would cause the model to predict charging and discharging durations that are too short. In such a case, the spherical shell approximation is therefore not applicable. The maximum SVR to thickness ratio, for which the approximation still yields acceptable results, could not be determined in this study, since experimental data was only available for the two capsule designs shown in Figure 5-7. Future studies should investigate the range of validity of this approximation in more detail, particularly for geometries of compact shape, yet large surface area.

5.4.2 Governing equations

The governing equations used to model the thermal response of PBLHS are based on the concentric dispersion approach discussed in section 5.1.2 in combination with the source term method outlined in section 2.5.2. Under consideration of the previously made modeling assumptions, the equation for the heat transfer of the HTF becomes:

$$\phi\left(\rho c_p\right)_{HTF}\frac{\partial T_{HTF}}{\partial t} + \left(\rho c_p u\right)_{HTF}\frac{\partial T_{HTF}}{\partial x} = \phi k_{HTF}\frac{\partial^2 T_{HTF}}{\partial x^2} + h_{HTF-PB}a_{PB}\left(T_{PB,R_C} - T_{HTF}\right) \tag{5.11}$$

Note that the thermal conductivity of the HTF is assumed to remain constant. The porosity ϕ of the packed bed is determined by the number of capsules N_C (which is usually known), their individual volume V_C and the volume occupied by the packed bed they form V_{PB}:

$$\phi = \frac{V_{PB} - N_C V_C}{V_{PB}} = \frac{H_{PB}A_T - N_C V_C}{H_{PB}A_T} \tag{5.12}$$

The volume occupied by the packed bed inside the storage tank V_{PB} is determined by the packed bed height H_{PB} and the inner cross-sectional area of the storage tank A_T.

The free flow velocity u_{HTF} is calculated according to Eq. (5.2), while the specific packed bed surface area a_{PB} is determined by:

$$a_{PB} = \frac{A_{PB}}{V_{PB}} = \frac{N_C A_C}{V_{PB}} \tag{5.13}$$

Here, A_{PB} is the total surface area of the packed bed, i.e., the product of the number of all PCM capsules comprising the bed and the surface area of one individual capsule A_C. All material properties of the HTF (density, heat capacity and conductivity) are assumed to be constant.

At the inlet, the temperature determined by the temperature sensors located inside the incoming pipe is used as boundary condition. At the outlet, a zero-gradient boundary condition (i.e., $\frac{\partial T}{\partial x} = 0$ for $x = H_T$) is applied, assuming that the outlet pipe is perfectly insulated.

Using the enthalpy-based source term method outlined in section 2.5.2 (see Equations (2.66) - (2.68)) the governing equation for the spherical shell domain (i.e., for $R_0 < r \leq R_C$) becomes:

$$c_{vol,PCM} \frac{\partial T_{PB}}{\partial t} = \frac{1}{r^2} \frac{\partial}{\partial r} \left(\lambda_{PCM} r^2 \frac{\partial T_{PB}}{\partial r} \right) - \rho_{l,PCM} L_{PCM} \frac{\partial \gamma}{\partial t} \tag{5.14}$$

In practice, the liquid fraction term is only relevant for the PCM region. For the encapsulation, the last term is set to 0 and the respective material properties are used. As boundary condition at the inner side of the spherical shell, a zero-gradient condition is applied (i.e., $\frac{\partial T}{\partial r} = 0$ for $r = R_0$). The outer boundary condition couples Eq. (5.14) with Eq. (5.11) and is based on Eq. (5.9):

$$k_C \frac{\partial T_{PB}}{\partial r}\bigg|_{r=R_C} = h_{HTF-PB} \left(T_{HTF} - T_{PB,R_C} \right) \tag{5.15}$$

where k_C is the conductivity of the encapsulation material. The remaining parameter that needs to be determined is the convective heat transfer coefficient h_{HTF-PB}, which can be related to the corresponding Nusselt number Nu_{HTF-PB} by:

$$h_{HTF-PB} = \frac{k_{HTF}\, Nu_{HTF-PB}}{2R_C} \tag{5.16}$$

The flow rates encountered in the packed beds during this case study were quite low, which indicates that forced convection might be accompanied by natural convection in the heat exchange between the HTF and the bed. To determine whether forced or natural convection is dominant or whether both have to be considered to calculate the packed bed

Nusselt number, the Richardson number Ri representing the ratio of buoyancy and flow shear stress is used:

$$Ri = \frac{2R_C g \phi \beta_{HTF} \left| T_{PB,R_C} - T_{HTF} \right|}{u_{HTF}^2} = \frac{Gr_{HTF}}{Re_{HTF}^2} \tag{5.17}$$

with β_{HTF} as the thermal expansion coefficient of the HTF, Gr_{HTF} as the Grashof number of the HTF and Re_{HTF} as the packed bed Reynolds number, which is calculated using the intrinsic pore velocity $u_v = u_{HTF}/\phi$ (see also Eq. (5.2)). The characteristic length (here $2R_C$) is the outer diameter of the spherical shell determined by:

$$D_C = 2R_C = \sqrt{A_C/\pi} \tag{5.18}$$

Following the mixed convection approach by Churchill [66], the Nusselt number becomes:

$$Nu_{HTF-PB} = \sqrt[3]{Nu_{fc}^3 + Nu_{nc}^3} \tag{5.19}$$

For the calculation of Nu_{HTF-PB}, the following cases have to be considered:

- If $Ri > 10$, forced convection is negligible, i.e., $Nu_{fc} = 0$.
- If $Ri < 0.1$, natural convection is negligible, i.e., $Nu_{nc} = 0$.
- If $0.1 \leq Ri \leq 10$, both types of convection have to be considered.

To estimate the forced convection Nusselt number, Gnielinski [113] suggests a correlation based on the Nusselt number for laminar and turbulent flow and a shape factor f:

$$Nu_{fc} = f\left(2 + \sqrt{Nu_{fc,lam}^2 + Nu_{fc,turb}^2}\right) \tag{5.20}$$

The laminar Nusselt number is given as:

$$Nu_{fc,lam} = 0.664\sqrt{Re_{HTF}}\sqrt[3]{Pr_{HTF}} \tag{5.21}$$

and the turbulent Nusselt number as:

$$Nu_{fc,turb} = \frac{0.037 Re_{HTF}^{0.8} Pr_{HTF}}{1 + 2.443 Re_{HTF}^{-0.1}\left(Pr_{HTF}^{2/3} - 1\right)} \tag{5.22}$$

The shape factor is an empirical quantity and is given by Gnielinski [114] for different packing elements such as cylinders, cubes, Raschig rings and others. For spheres, it is a function of the bed porosity:

$$f = 1 + 1.5(1 - \phi) \tag{5.23}$$

The Nusselt number for natural convection around a heated or cooled sphere is provided by Kast et al. [115] as:

$$Nu_{nc} = 2 + 0.56\left(\frac{Pr_{HTF}Ra^*}{0.846 + Pr_{HTF}}\right)^{1/4} \tag{5.24}$$

Since the influence of the packed bed has to be considered, Thess & Kaiser [116] suggest using a modified version of the Rayleigh number Ra^* based on the Darcy number Da:

$$Ra^* = RaDa = \frac{g\beta_{HTF}D_C^3\left|T_{PB,R_C} - T_{HTF}\right|}{\nu_{HTF}a_{HTF}}\frac{D_C^2}{180}\frac{\phi^3}{(1-\phi)^2H_{PB}^2} \tag{5.25}$$

As mentioned in the previous section, the spherical shell approximation may also be applied to the packed elements of sensible heat storages. To adapt the model to such sensible storages, only minor modifications are required. By simply setting the liquid fraction γ in Eq. (5.14) to 0 (or by setting the liquidus and solidus temperature higher than the temperatures encountered in the simulated process), λ and c_{vol} become k_s and $\rho_s c_{p,s}$, respectively, for which the according properties of the solid packed elements such as gravel, rock or metal particles can be used. Additionally, by setting the specific packed bed surface area a_{PB} to 0 and the porosity ϕ to 1, purely sensible liquid storage systems such as hot water or oil storages can be simulated.

5.4.3 Numerical algorithm

The two governing equations for the developed PBLHS model are discretized using different finite differences schemes. The equation for the HTF (Eq. (5.11)) is discretized using the explicit finite differences method (see Eq. (2.48)), while the spherical shell domain (Eq. (5.14)) is discretized using the implicit finite differences method according to the procedure outlined in section 3.1. In this way, the temperature field of the HTF is calculated with information from the previous time step, which is then used to determine the boundary heat flux according to Eq. (5.15) required for calculating the shell domain temperature field. Through this procedure, both domains are evaluated in a time-consistent manner, while avoiding any iteration process between the HTF and shell domain.

During a simulation run, first, the material and geometrical properties are initialized. Thereafter, the spherical shell approximation is performed, and the temporal and spatial grids are generated based on the chosen discretization parameters (i.e., Δt, Δx and Δr). It follows the initialization of the temperature fields in the HTF and spherical shell domain, while a uniform temperature distribution is assumed for both the HTF and PCM capsules. From these temperature values, the initial liquid fraction and enthalpy are determined for each PCM grid node.

After initialization, the time loop starts with the calculation of the first time step. The discretized equation (5.11) is solved for the whole HTF domain based on the initial conditions, the inlet flow rate (determining u_{HTF}) and the inlet temperature, which is the boundary condition for T_{HTF} at $x = 0$. Additionally, the convective heat transfer

coefficient h_{HTF-PB} is calculated for each HTF node based on the flow velocity u_{HTF} and temperatures T_{HTF} and T_{PB}. The new HTF temperature field is used to determine the heat flux between HTF and the PCM capsules, which is calculated by Eq. (5.15) for each HTF node and serves as the boundary condition at the outer surface of the spherical shell domain. Now, the algorithm outlined in section 3.1 is started, iteratively determining the new temperature field of the spherical shell domain T_{PB} for each HTF grid node according to Eq. (5.14). Based on this temperature field, the surface temperature of the packed bed T_{PB,R_C} is evaluated in order to calculate the new HTF temperature field in the next time step via Eq. (5.11). This procedure is repeated until the end of the total simulated time t_t. A flow chart of the described algorithm is shown in Figure 5-14.

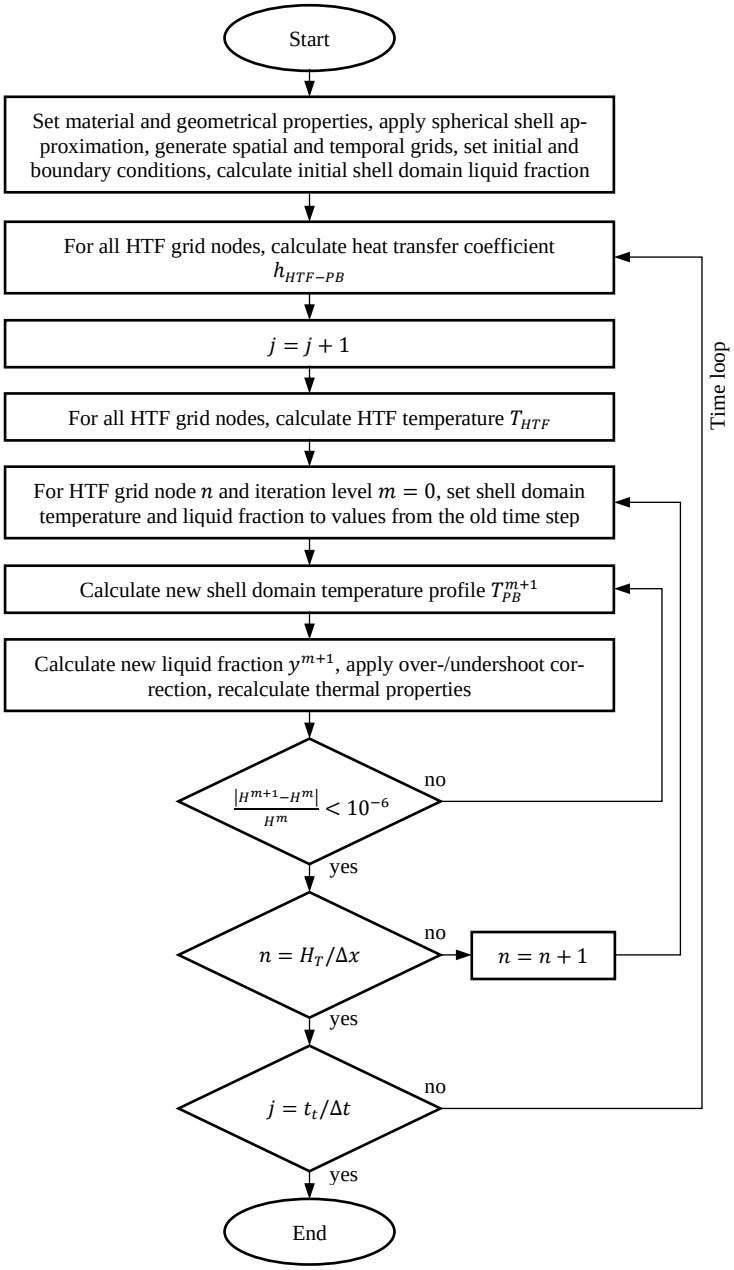

Figure 5-14: Flow chart of the numerical algorithm used for simulating the thermal response of PBLHS

5.5 Experimental results and model validation

5.5.1 Experimental results

The experimental data used for validation were obtained with the two test storage systems described in section 5.3. The experiments were conducted with varying flow rates and inlet temperatures. These flow rates were 216 kg/h, 360 kg/h, 600 kg/h and 1000 kg/h. The inlet temperature was defined in relation to the melting point T_m = 57 °C as $T_{in} = T_m + \Delta T/2$ for charging and $T_{in} = T_m - \Delta T/2$ for discharging. ΔT was varied between 7.2 K, 12 K and 20 K.

5.5.1.1 Cuboid storage system

The parameter combinations for the experimental runs performed with the cuboid storage are shown in Table 5-5. An experimental run consisted of a full charging process and a full discharging process. The charging/discharging durations, defined as the time required for the storage to reach a uniform temperature distribution, are listed as well. A uniform temperature distribution is assumed when all sensors read the same temperature (within a certain threshold of < 0.6 K).

Table 5-5: Parameter combinations and charging/discharging durations for experimental runs performed at the cuboid storage setup

Run number	1	2	3	4	5	6	7	8
Flow rate [kg/h]	360	600	1000	216	360	600	216	360
Temperature difference ΔT [K]	7.2	7.2	7.2	12	12	12	20	20
Charging duration [h]	23.7	15.7	11.1	22.5	14.5	9.5	14.9	9.7
Discharging duration [h]	21.9	14.9	12.1	22.3	14.9	10.2	15.5	10.3

The temperature curves for charging and discharging the cuboid storage system are shown in Figure 5-15 and Figure 5-16. The first three runs are shown in the upper diagram (ΔT = 7.2 K), the next three runs in the middle diagram (ΔT = 12 K) and the last two runs in the lower diagram (ΔT = 20 K). The flow rates are indicated by symbols in accordance with the run number (e.g., in the top charts, ΔT = 7.2 K, so the diamond symbol indicates run 2 with a flow rate of 600 kg/h). The colors represent the location of the temperature sensors as indicated in Figure 5-9. During the charging process, hot HTF enters from the inlet at the top (red), then passes the upper sensor (yellow), then the lower sensor (green) and then leaves through the outlet at the bottom (blue). During the discharging process, cold HTF enters from the bottom inlet (blue), then passes the lower sensor (green), then the upper sensor (yellow) and then leaves through the outlet at the top (red).

The results show that with large temperature differences ΔT and high flow rates, the charging/discharging duration reduces, as expected. For the experimental runs listed in Table 5-5, the charging duration varied between 23.7 h (run 1) and 9.5 h (run 6), and the

discharging duration varied between 22.3 h (run 4) and 10.2 h (run 6). For low flow rates and small temperature differences, discharging is faster than charging, while for high flow rates and larger temperature differences, it is vice versa. Further, for a flow rate of 1000 kg/h, the temperature curve of the lower sensor cuts the curve of the outlet sensor, which indicates a certain degree of maldistribution (the incoming HTF moves faster close to the storage wall where the packing is less dense and flows around the packed bed instead of through it).

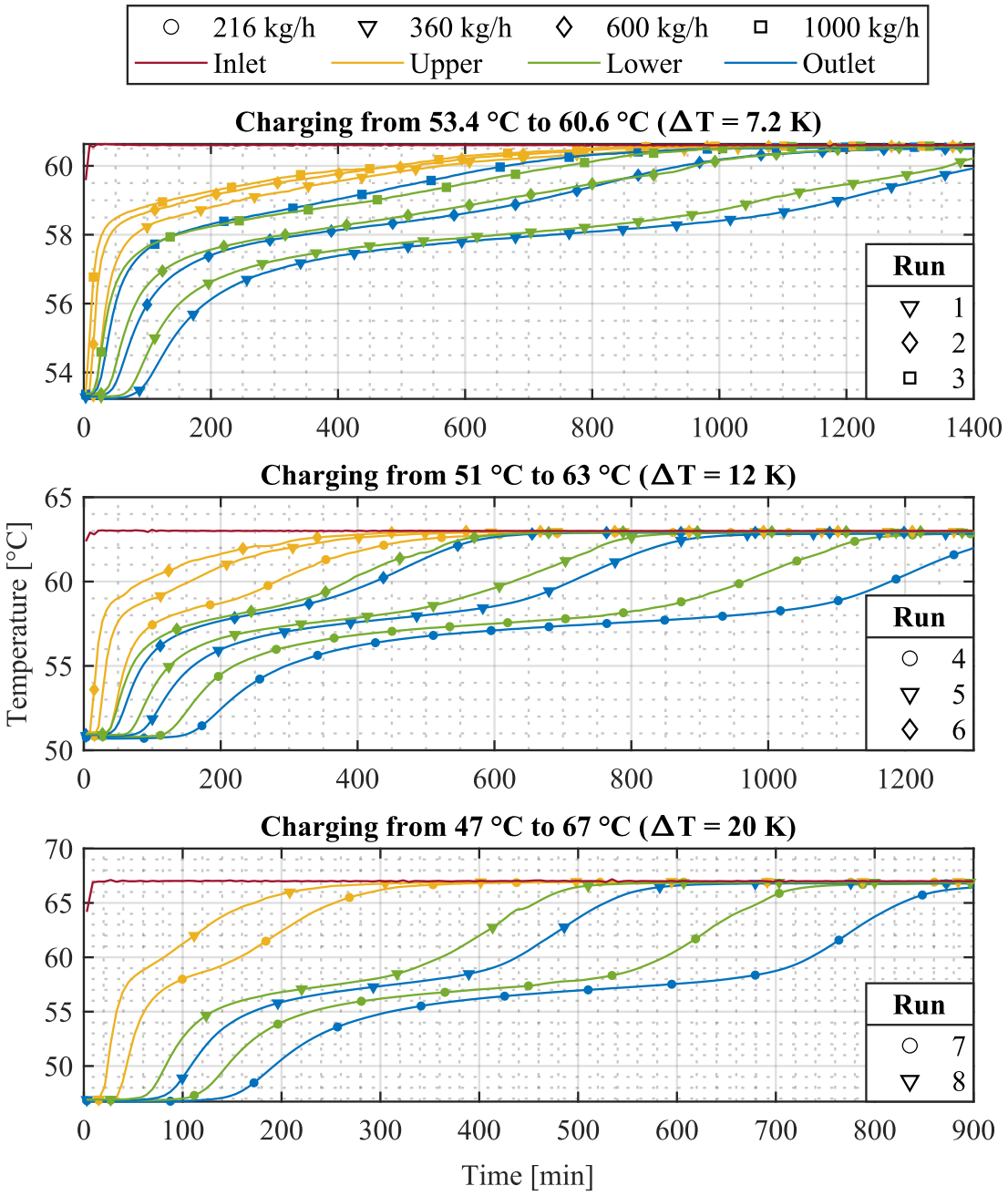

Figure 5-15: Sensor temperatures (indicated by colors) measured during charging experiments (flow direction from top to bottom) at the cuboid storage setup for different inlet temperatures and flow rates (indicated by symbols)

In the discharging curves shown in Figure 5-16, the effect of subcooling is clearly observable for large flow rates and smaller ΔT. This behavior is due to the faster HTF

exchange within the storage, which causes a larger number of PCM capsules to start crystallizing simultaneously. In contrast, at a low flow rate and large ΔT, the capsules located at the bottom of the storage begin crystallizing first, gradually heating up the HTF.

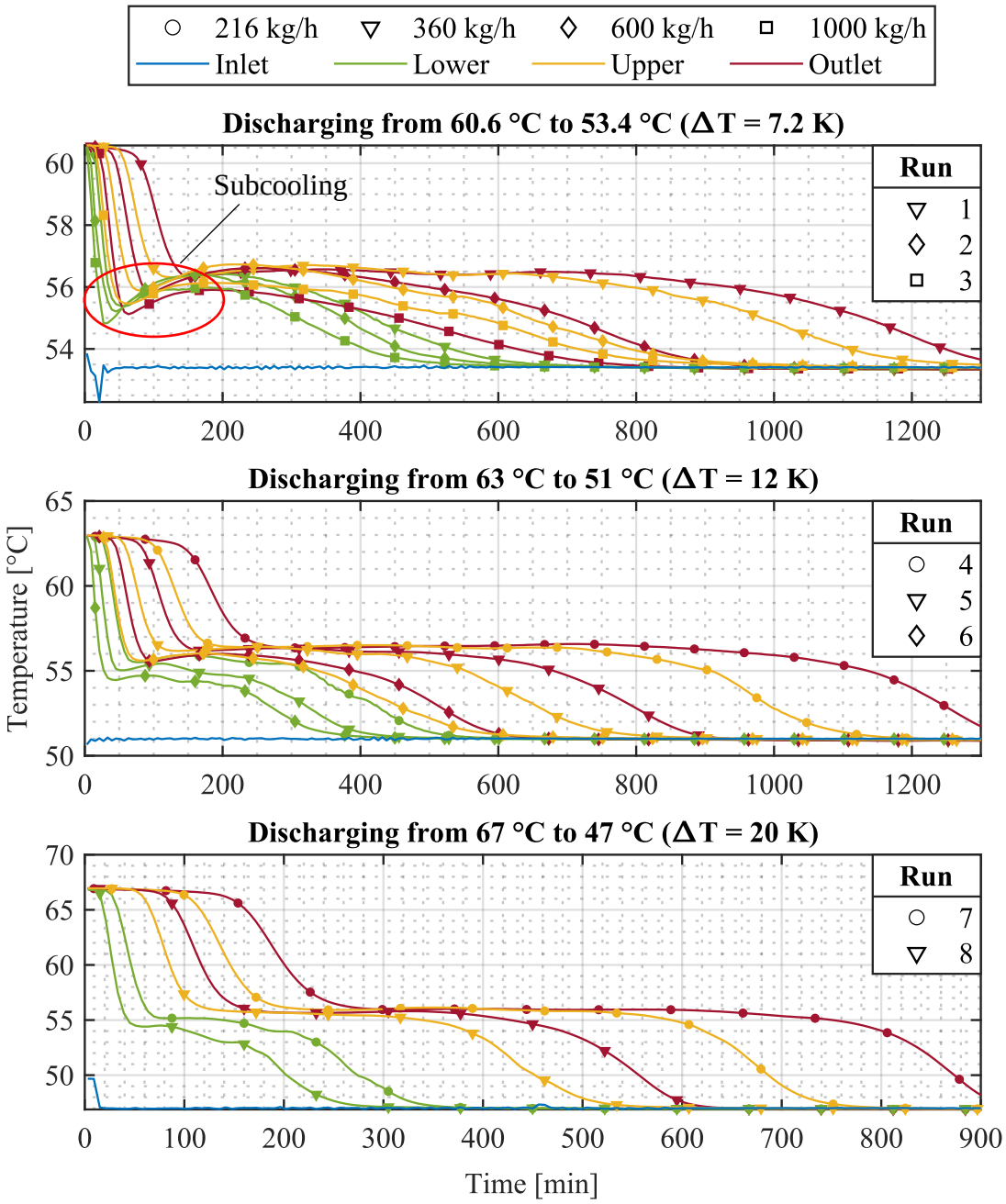

Figure 5-16: Sensor temperatures (indicated by colors) measured during discharging experiments (flow direction from bottom to top) at the cuboid storage setup for different inlet temperatures and flow rates (indicated by symbols)

5.5.1.2 Cylindrical storage system

The parameter combinations, run definitions and charging/discharging durations for the cylindrical storage setup are shown in Table 5-6. The temperature uniformity threshold had to be increased to 0.9 K for charging the cylindrical storage, likely due to poorer thermal insulation.

Table 5-6: Parameter combinations and charging/discharging durations for experimental runs performed at the cylindrical storage setup

Run number	1	2	3	4	5	6	7	8
Flow rate [kg/h]	360	600	1000	216	360	600	216	360
Temperature difference ΔT [K]	7.2	7.2	7.2	12	12	12	20	20
Charging duration [h]	29.5	18.1	11.7	29.0	17.6	11.5	22.2	11.8
Discharging duration [h]	25.7	18.2	13.3	24.5	16.6	11.6	17.3	11.5

The temperature curves for charging and discharging the cylindrical storage system are shown in Figure 5-17 and Figure 5-18. Similarly to the results for the cuboid storage system, the first three runs are shown in the upper diagram (ΔT = 7.2 K), the next three runs in the middle diagram (ΔT = 12 K) and the last two runs in the lower diagram (ΔT = 20 K). The flow rates are indicated by symbols in accordance with the run numbers. The colors represent the location of the temperature sensors as indicated in Figure 5-10. During the charging process, shown in Figure 5-17, hot HTF enters from the inlet at the top (red), then passes the middle sensor (yellow) and then leaves through the outlet at the bottom (blue). During the discharging process shown in Figure 5-18, cold HTF enters from the bottom inlet (blue), then passes the middle sensor (yellow) and then leaves through the outlet at the top (red).

As with the cuboid storage system, the results show that the charging and discharging durations are reduced with larger ΔT and high flow rates. For the experimental runs listed in Table 5-6, the charging durations were generally higher than those determined for the cuboid storage due to a larger storage capacity and varied between 29.5 h (run 1) and 11.5 h (run 6), while the discharge durations varied between 25.7 h (run 1) and 11.5 h (run 8). For low flow rates and small temperature differences, discharging was faster than charging, while for high flow rates and larger temperature differences, the opposite was observed. A subcooling behavior similar to the cuboid storage could be noticed for the cylindrical storage as well, which is less visible for low flow rates.

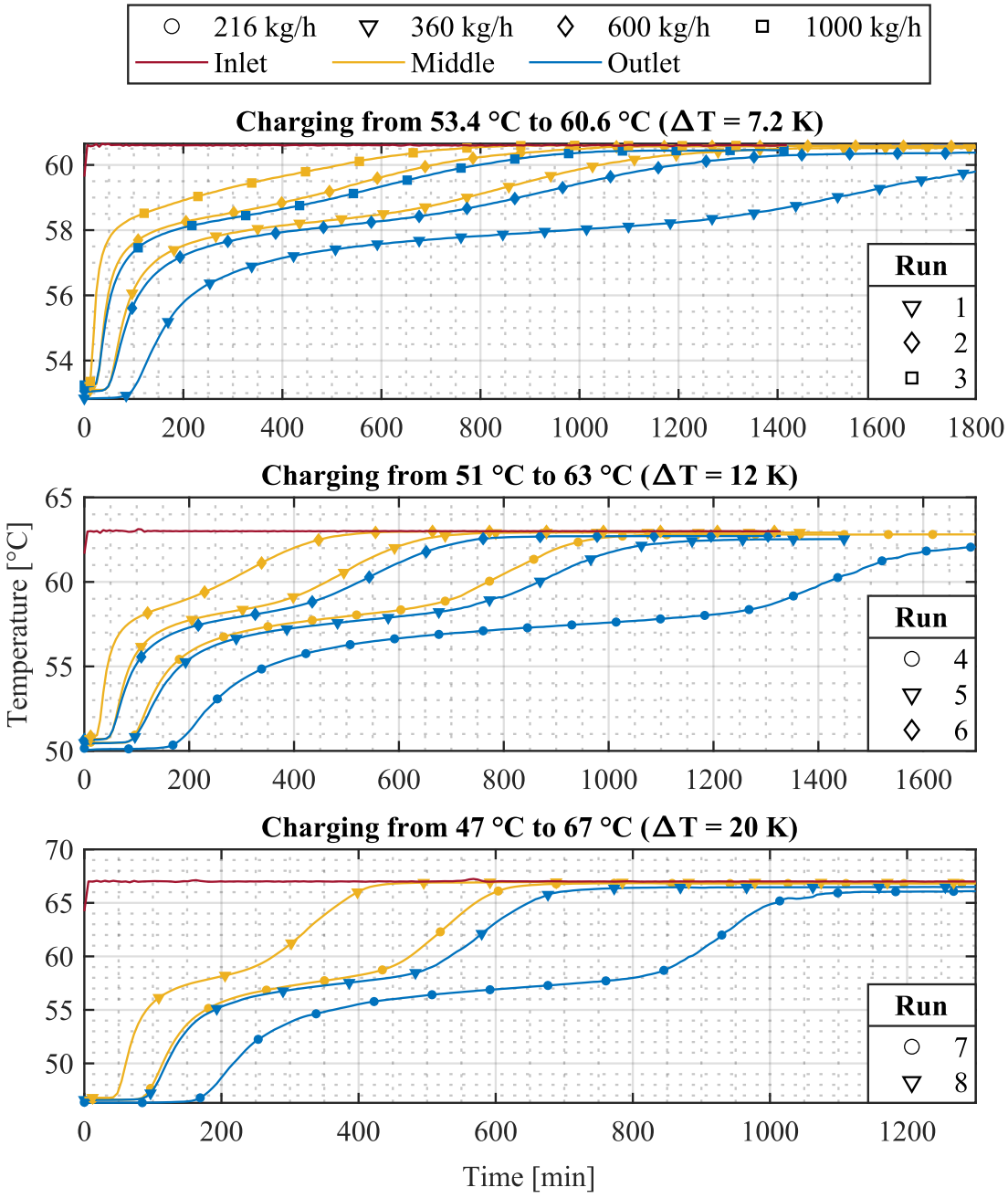

Figure 5-17: Sensor temperatures (indicated by colors) measured during charging experiments (flow direction from top to bottom) at the cylindrical storage setup for different inlet temperatures and flow rates (indicated by symbols)

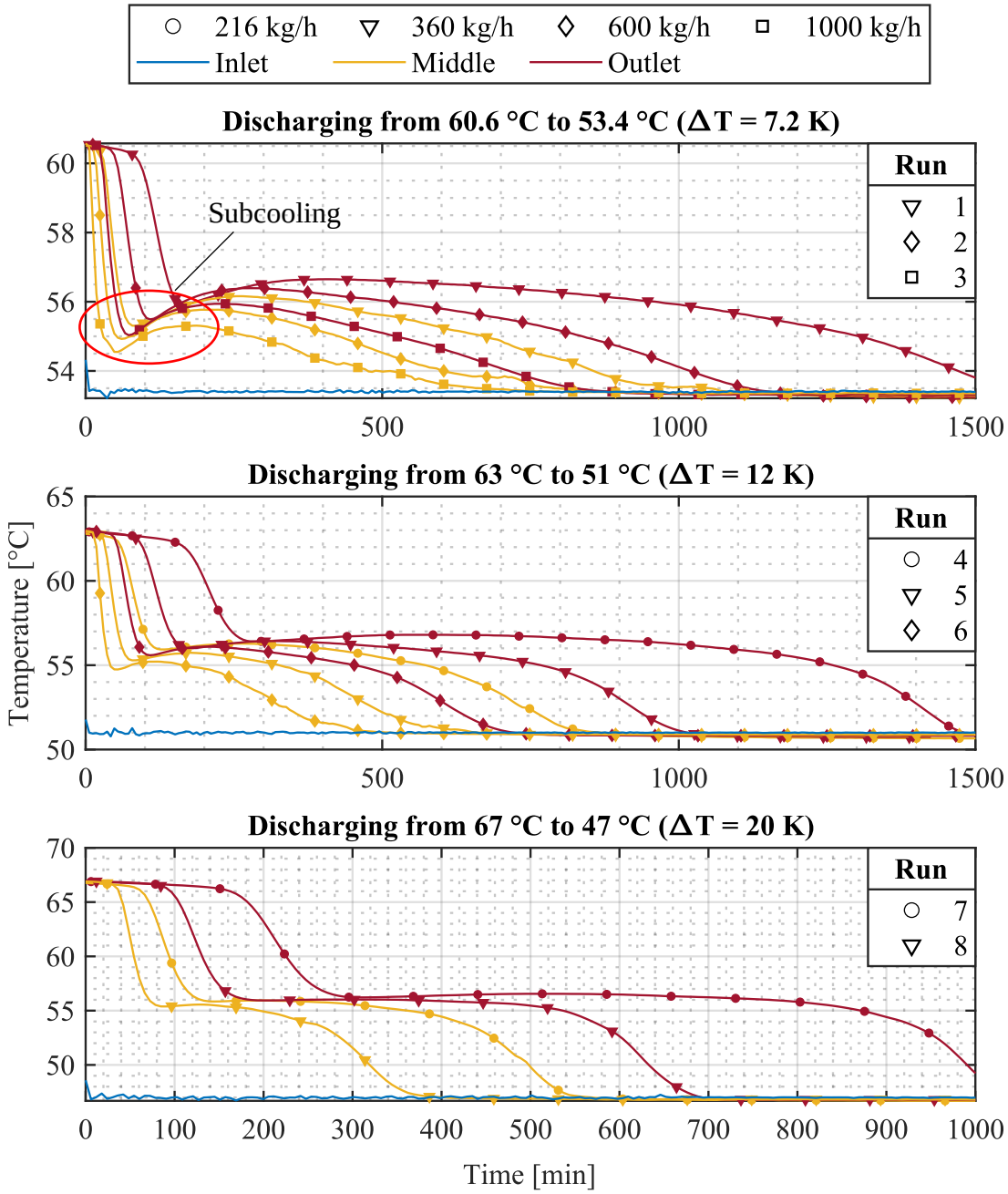

Figure 5-18: Sensor temperatures (indicated by colors) measured during discharging experiments (flow direction from bottom to top) at the cylindrical storage setup for different inlet temperatures and flow rates (indicated by symbols)

5.5.2 Model validation

As in the previous case study, a grid independence analysis was conducted to ensure that the simulation results do not depend on the chosen spatial step size for the HTF and the PCM domain (Δx and Δr). The grid independence study was performed for charging the cuboid storage with a flow rate of 600 kg/h and a temperature interval of 12 K. The initial simulation was performed with a time step of 2.5 s and a Δx and Δr of 59.5 mm and 0.63 mm, respectively. The spatial step size was halved for each consecutive run until the results showed only marginal changes. The spatial step sizes identified by this procedure

were Δx = 3.72 mm and Δr = 0.156 mm, which corresponds to a subdivision of the HTF domain into 400 nodes and of the spherical shell domain into 40 nodes.

The validation was performed using the experimental data presented in the previous section. The simulation results were evaluated based on the MAE, the $RMAE$ (both defined in section 3.3.1) and the maximum error ME, which is the maximum difference between the simulated and measured values:

$$ME = \max\left(\left|\hat{Y}_i - Y_i\right|\right) \tag{5.26}$$

The ME can also be expressed in relation to the overall value range:

$$RME = \frac{\max\left(\left|\hat{Y}_i - Y_i\right|\right)}{\Delta Y} \cdot 100\ \% \tag{5.27}$$

Here, the value range ΔY was taken as the difference between the initial and the inlet temperature.

5.5.2.1 Cuboid storage system

Regarding the cuboid storage system, Table 5-7 shows the MAE values for the upper, the lower and the outlet sensors (located at the bottom during charging and at the top during discharging), as indicated in Figure 5-9. In addition, the $RMAE$ and the RME, both with respect to the outlet temperature, are listed. The focus of the evaluation was on the deviations of the outlet temperature, since it is the most relevant for the operation of the storage system.

The overall agreement between the measured and simulated results for the cuboid system was satisfactory, as the MAE_{out} and $RMAE_{out}$ did not exceed 0.98 K (run 7) and 8.3 % (run 1) during the eight experimental runs. The discharging simulation results seem to agree better with the measured data. It appears that, for charging, the model accuracy decreases with lower flow rates while ΔT is kept at the same value (except for ΔT = 20 K). For similar flow rates, the relative deviation (i.e., the $RMAE_{out}$) increases with smaller temperature differences, even though the absolute temperature deviations (i.e., the MAE_{out}) slightly decrease. For discharging, no such clear trends could be observed for the outlet temperature, and the $RMAE_{out}$ remained relatively unaffected by the flow rate for temperature differences of 12 K and 20 K, while it was highest for a flow rate of 600 kg/h and ΔT = 7.2 K (run 2). The average relative deviation for charging was 5.6 %, while it was 3.8 % for discharging. For all eight runs, the maximum observed RME was 28.7 % (run 4), which seemed to be relatively high. Both these values were obtained for charging the storage.

Table 5-7: Deviations between measured and simulation results for the cuboid storage system in terms of the MAE based on temperature data obtained from the upper, the lower and the outlet sensor, as well as $RMAE$ and RME for the outlet temperature

		Charging					Discharging				
Error type		MAE			$RMAE$	RME	MAE			$RMAE$	RME
	Sensor	upper	lower	outlet	outlet	outlet	upper	lower	outlet	outlet	outlet
ΔT	Run	[K]	[K]	[K]	[%]	[%]	[K]	[K]	[K]	[%]	[%]
7.2 K	1*	0.25	0.67	0.61	8.3	27.3	0.49	0.40	0.35	4.8	19.0
	2’	0.31	0.55	0.47	6.5	26.5	0.55	0.64	0.45	6.3	15.1
	3^	0.58	0.53	0.42	5.8	25.1	0.72	0.74	0.33	4.7	12.2
12 K	4+	0.29	0.75	0.79	6.5	28.7	0.31	0.25	0.32	2.7	15.6
	5*	0.33	0.80	0.58	4.8	25.6	0.33	0.4	0.32	2.7	11.2
	6’	0.39	0.82	0.49	4.1	24.5	0.48	0.74	0.37	3.1	8.8
20 K	7+	0.41	0.99	0.98	4.8	25.1	0.66	0.52	0.60	3.0	10.5
	8*	0.49	1.18	0.79	3.9	22.6	0.72	0.67	0.53	2.7	9.1
	Mean	0.38	0.79	0.64	5.6	25.7	0.53	0.55	0.41	3.8	11.8

+ 216 kg/h; * 360 kg/h; ’ 600 kg/h; ^ 1000 kg/h

Figure 5-19 shows the temperature curves for charging with 360 kg/h, which was the flow rate used in combination with all three ΔT values. It can be seen, that with an increasing ΔT, the qualitative agreement between the simulated and experimental curves becomes better, especially for the outlet temperature. For the lowest ΔT, the simulated curves look quite different from the experimental ones and significantly underestimate the charging duration.

In all three cases, the simulated temperatures increased much faster than the experimental ones right until the beginning of the phase change, which coincides with the time at which the maximum RME_{out} is encountered. The reason may be that the model assumes an ideal porous medium, in which no recirculation and uneven flow distribution exist, which, in reality, slow down the convective heat transport. In contrast, during the phase change, the temperature differences within the storage are lower and the effect of maldistribution is less noticeable resulting in lower deviations.

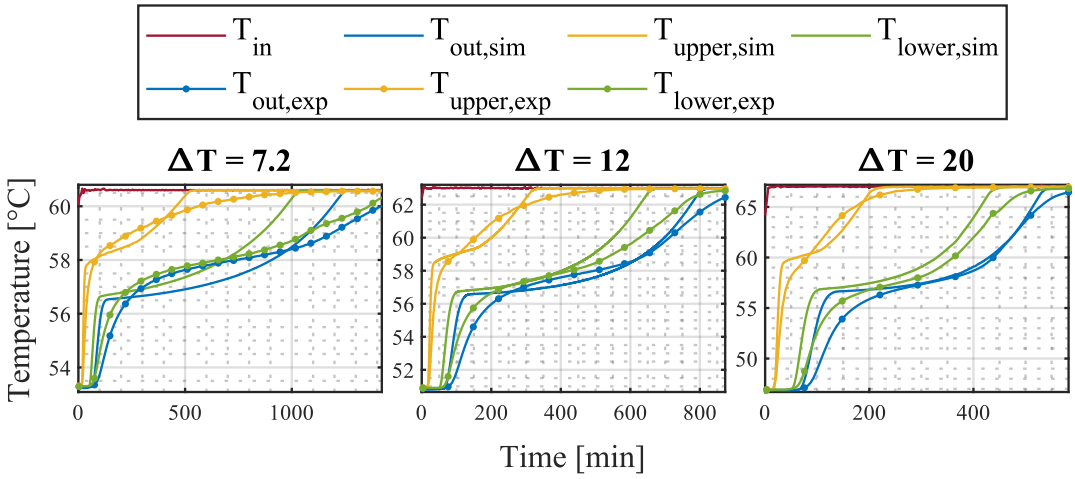

Figure 5-19: Simulated and experimental temperatures for charging the cuboid storage with a flow rate of 360 kg/h and three temperature differences (runs 1, 5 and 8)

Taking a look at the temperature charts for discharging displayed in Figure 5-20, it can be seen that the curves for a ΔT of 7.2 K show a rather large qualitative deviation. For the two higher temperature differences, the simulated and experimental curves show a much better agreement, especially for the outlet temperature. It becomes apparent that the model cannot account for subcooling effects, which cause the temperature to drop below the actual solidification temperature before crystallization is initiated. This effect is especially noticeable for the smallest ΔT.

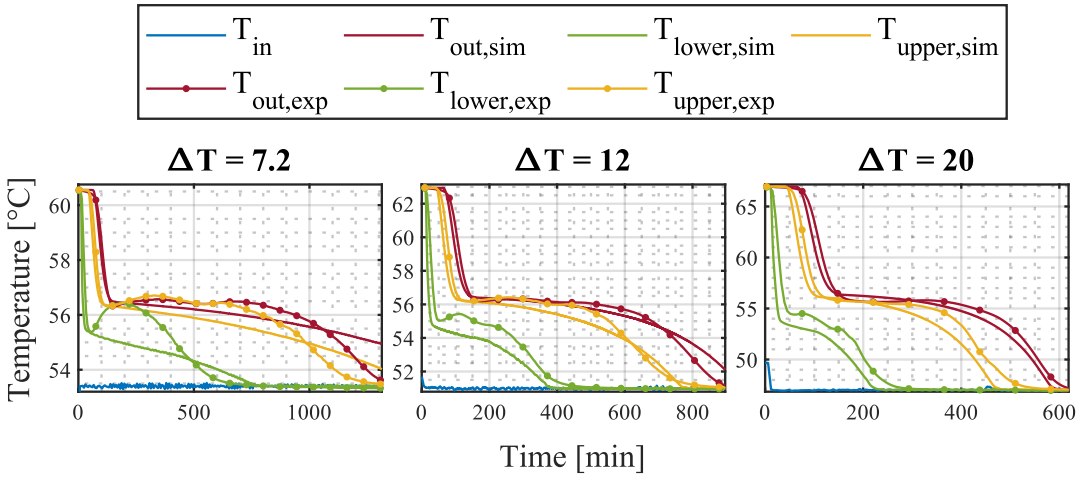

Figure 5-20: Simulated and experimental temperatures for discharging the cuboid storage with a flow rate of 360 kg/h and three temperature differences (runs 1, 5 and 8)

In summary, the average deviation for the outlet temperature across all eight runs was 5.6 % for charging and 3.8 % for discharging. With a value of 25.7 %, the average maximum deviation for charging was quite high, while it was significantly lower for discharging, with an average RME_{out} of 11.8 %. The best simulation results were generated when the driving forces for heat transfer were high, i.e., for high temperature differences and flow rates. In conclusion, the model yields acceptable results for the cuboid storage system, which can be considered a special case due to the structured arrangement of the PCM capsules.

5.5.2.2 Cylindrical storage system

The model deviations for the cylindrical storage system are listed in Table 5-8. The average $RMAE_{out}$ was slightly lower for charging compared to the cuboid system, while it was similar for discharging. Also, as was the case for the cuboid storage, the model accuracy was higher for discharging. A maximum $RMAE_{out}$ of 7.9 % was observed for charging with 360 kg/h and ΔT = 7.2 K (run 1). Again, for charging, the relative accuracy increases with higher flow rates and temperature differences ΔT. For discharging, it appears largely unaffected by the flow rate while it slightly increases for increasing values of ΔT (see runs 1, 5 and 8).

The maximum observed deviation at the outlet was for charging during run 1. With 25.9 %, it is slightly lower than that of the cuboid system. However, the discharging simulations produced less accurate results compared to the cuboid system showing a maximum RME_{out} of 28.4 % (run 4).

Table 5-8: Deviations between measured and simulation results for the cylindrical storage system in terms of the MAE based on temperature data obtained from the middle and the outlet sensor, as well as $RMAE$ and RME for the outlet temperature

		Charging				Discharging			
Error type		MAE		$RMAE$	RME	MAE		$RMAE$	RME
Sensor		middle	outlet	outlet	outlet	middle	outlet	outlet	outlet
ΔT	Run	[K]	[K]	[%]	[%]	[K]	[K]	[%]	[%]
7.2 K	1*	0.33	0.61	7.9	25.9	0.49	0.34	4.8	20.8
	2’	0.28	0.42	5.5	24.9	0.45	0.36	5.0	15.9
	3^	0.28	0.34	4.5	25.0	0.36	0.36	5.1	12.1
12 K	4+	0.50	0.74	5.7	27.1	0.72	0.45	3.7	28.4
	5*	0.34	0.54	4.3	24.9	0.60	0.40	3.3	20.3
	6’	0.41	0.46	3.7	24.5	0.55	0.45	3.7	14.7
20 K	7+	0.80	0.91	4.4	23.0	0.71	0.49	2.5	17.7
	8*	0.72	0.78	3.8	20.8	0.63	0.62	3.1	11.0
	Mean	0.46	0.60	5.0	24.5	0.56	0.43	3.9	17.6

+ 216 kg/h; * 360 kg/h; ’ 600 kg/h; ^ 1000 kg/h

To qualitatively compare the simulation to the experimental results, the temperature curves for the three runs with a flow rate of 360 kg/h are shown in Figure 5-21 and Figure 5-22. As was the case for the cuboid storage, the qualitative agreement between simulation and experimental data is the worst for the lowest temperature difference and the charging duration is significantly underestimated by the model. The curves for the two higher ΔT values show a satisfactory fit after the large deviation right before the phase change temperature plateau, which was also observed for the cuboid storage. The reason is likely the same, i.e., the model does not account for flow disturbances caused by the packed bed.

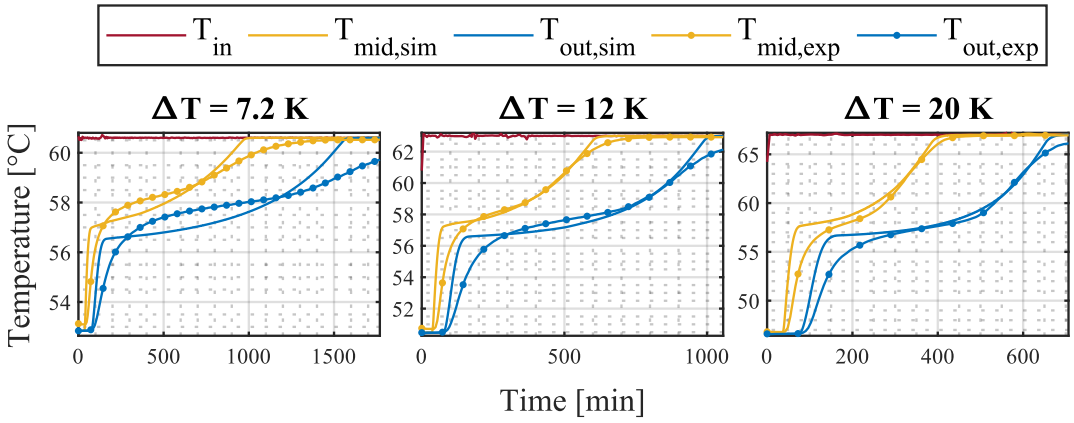

Figure 5-21: Simulated and experimental temperatures for charging the cylindrical storage with a flow rate of 360 kg/h and three temperature differences (runs 1, 5 and 8)

The discharging curves displayed in Figure 5-22 show a behavior similar to that observed for the cuboid storage system. Again, the simulations with the lowest ΔT generate the worst results in terms of model accuracy, mainly due to the neglection of subcooling. The effect is less dominant with larger temperature differences and therefore the model produces better results in such cases.

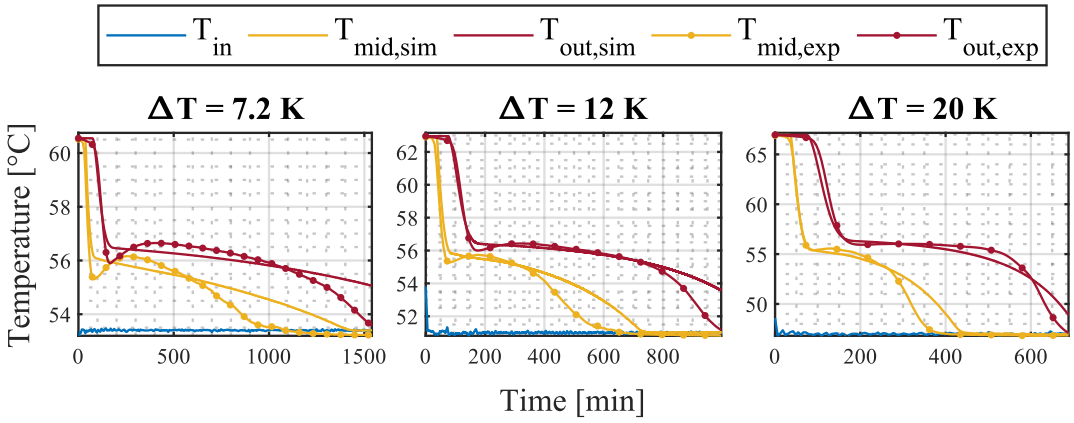

Figure 5-22: Simulated and experimental temperatures for discharging the cylindrical storage with a flow rate of 360 kg/h and three temperature differences (runs 1, 5 and 8)

The model yields satisfactory results for the cylindrical storage system as well, with an average deviation across all eight runs of 5 % for charging and 3.9 % for discharging. The average maximum deviation for charging was 24.5 %, and for discharging it was 17.6 %. Similar to the cuboid storage system, the model produced more accurate results when the temperature difference and flow rate are high.

Altogether, the highest mean deviation between the experimental and the simulated outlet temperatures was 8.3 %, which complies with the goal formulated in section 5.2 of an accuracy of 90 %. For both investigated systems, the accuracy was slightly higher for discharging than for charging and was lower for small temperature differences and flow rates.

The main sources for modeling inaccuracies that could be identified are the assumption of ideal flow through the packed bed (i.e., the assumption of a homogenous porous

medium) and the neglection of subcooling effects. The former causes high deviations during charging right before the PCM starts to melt. The latter causes deviations mainly after the phase change, since the sudden solidification causes the instantaneous release of a large amount of heat once the crystallization temperature is reached. This behavior is currently not captured by the model but is the subject of ongoing research activity.

5.6 Parameter study

After successful validation of the thermal model for PBLHS, the next step in the case study was to develop new, improved capsule geometries. In order to identify such capsule geometries that can achieve both high energy density and thermal power, new designs based on superellipsoids were tested in a parameter study. Superellipsoids are geometrical bodies defined by three parametric equations. These equations depend on only five input parameters, allowing for the creation of a wide range of geometries, which makes superellipsoids particularly useful as a basis for conducting a geometrical parameter study. The achievable packing density of different superellipsoids created based on various parameter combinations was determined by filling simulations. These simulations were performed using a discrete element method (DEM), which is readily implemented in the commercial software toolbox STAR-CCM+. The DEM results were validated through experiments and consequently used to further investigate the thermal performance of selected superellipsoids.

Some of the contents presented in this section, particularly regarding the DEM filling simulations, were taken from a student project report by Kuckuck [89], which was supervised by the author.

5.6.1 Superellipsoids

Superellipsoids are three-dimensional geometrical objects, which are defined by two superelliptic curves. They were first used for design purposes in architecture by Danish mathematician Piet Hein, who aimed to create shapes that are neither circular nor rectangular, but something in between [117]. In 1981, Barr [118] derived the following parametric functions describing the surface of superellipsoid geometries:

$$\begin{aligned} x(v,w) &= a \cdot sgn\big(cos(w)\big) \cdot |cos(w)|^n \cdot sgn\big(cos(v)\big) \cdot |cos(v)|^e \\ y(v,w) &= b \cdot sgn\big(cos(w)\big) \cdot |cos(w)|^n \cdot sgn\big(sin(v)\big) \cdot |sin(v)|^e \\ z(v,w) &= c \cdot sgn\big(sin(w)\big) \cdot |sin(w)|^n \\ \text{for} \quad -\pi \le v < \pi \quad &\& \quad -\pi/2 \le w \le \pi/2 \end{aligned} \tag{5.28}$$

Here, a, b and c are the maximum extension of the superellipsoid in each spatial direction, while e and n are the shape factors that determine the roundness of the resulting geometry, and v and w are the surface parameters. Figure 5-23, left, shows an illustration of a superellipsoid with its specific parameter values. While the axis lengths determine the

overall dimensions of the resulting geometry, the shape factors determine the sharpness of the edges and whether the surfaces are concave or convex, as illustrated in Figure 5-23, right. For shape factors $e = n = 0$, the superellipses shaping the superellipsoid are rectangles and therefore, the surfaces of the body are plane, forming a cuboid. With increasing shape factors, these surfaces become convex until a value of $e = n = 2$ is reached, at which the superellipses form rhombi and the body surfaces become plane again. When the shape factors are increased even further, the surfaces become concave, and the topology of the object star-shaped.

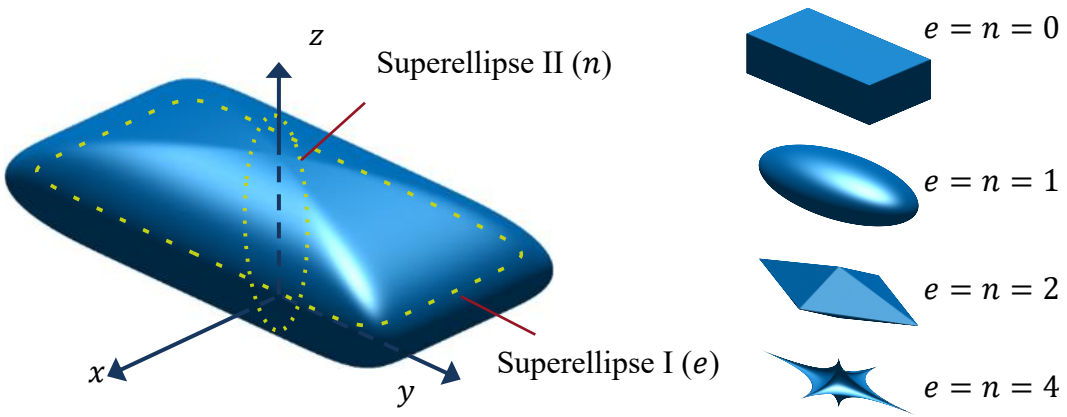

Figure 5-23: Illustration of a superellipsoid with parameters a = 2, b = 4, c = 1, e = 0.2 and n = 1 (left, adapted from [89]) and the influence of the shape factors (right)

The geometrical flexibility of shapes created by Equations (5.28) is very high, with a vast variety of geometrical forms. Another convenient aspect of superellipsoids is the fact that their volume can be determined by a single equation:

$$V_S = \frac{2}{3} abcen\mathrm{B}\left(\frac{e}{2},\frac{e}{2}\right)\mathrm{B}\left(n,\frac{n}{2}\right) \tag{5.29}$$

where B is the beta function, which is included in the MATLAB function library (see, e.g., [119,120] for more details on the beta function).

Two aspect ratios were defined to further reduce the number of variable parameters:

$$\beta_S = \frac{a}{b} \tag{5.30}$$

$$\gamma_S = \frac{a}{c} \tag{5.31}$$

Inserting equations (5.30) and (5.31) into Eq. (5.29) and rearranging for a allows to express the lengths of the superellipsoid semi-axes in terms of the two aspect ratios, the shape factors and the volume:

$$a = \sqrt[3]{\frac{3\beta_S\gamma_S V_S}{2en\mathrm{B}\left(\frac{e}{2},\frac{e}{2}\right)\mathrm{B}\left(n,\frac{n}{2}\right)}} \tag{5.32}$$

With a determined by Eq. (5.32) for a given volume, the remaining axis lengths can in turn be calculated from equations (5.30) and (5.31).

5.6.2 Packing density and SVR

Equations (5.28) were implemented in MATLAB as an executable script that generates the surfaces of the superellipsoids. These surfaces were then exported in STL format, a common standard for CAD data exchange. The STL-files were subsequently imported into STAR-CCM+ to carry out the DEM simulations, through which the packing density of different superellipsoid geometries were determined. The DEM approach that was used for the creation of the packed beds is based on the method proposed by Feng et al. [121], which was developed for convex geometries and is readily implemented in STAR-CCM+.

Before conducting the parameter study, the DEM was validated through simple filling experiments. In those experiments, 3D-printed miniature superellipsoid pellets made of polyamide 12 were used. Each geometry considered for validation had the same volume of approximately 7.7 ml. This volume is based on a 1:5 scale-down of an Axiotherm PCM capsule containing about 1 kg of PCM. The properties of the superellipsoid geometries considered for the validation of the DEM simulations are listed in Table 5-9.

Table 5-9: Geometry parameters of the six 3D-printed superellipsoid pallets used for validating the DEM simulations

Geometry	Parameters				Geometry	Parameters			
	β	γ	m	n		β	γ	m	n
1 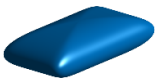	2	3	10	2	4 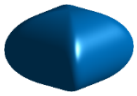	1	1	10	2
2 	2	0.4	10	2	5 	2	3	10	1.2
3 	6	2	10	2	6 	6	2	10	1.2

Of each of the six superellipsoid geometries shown in Table 5-9, 350 pellets were 3D-printed, with which experiments were conducted using the setup shown in Figure 5-24. In the first step, the pellets were filled into the pellet container. Next, the cover at the bottom of the container was removed, allowing the pellets to fall into a tank. Once the pellets settled into a packed bed, the height of the bed was measured. This procedure was performed five times for each geometry, yielding an average bed height determined from the individual measured values. The resulting average was then used to calculate the packing density of each superellipsoid using equations (5.10) and (5.12).

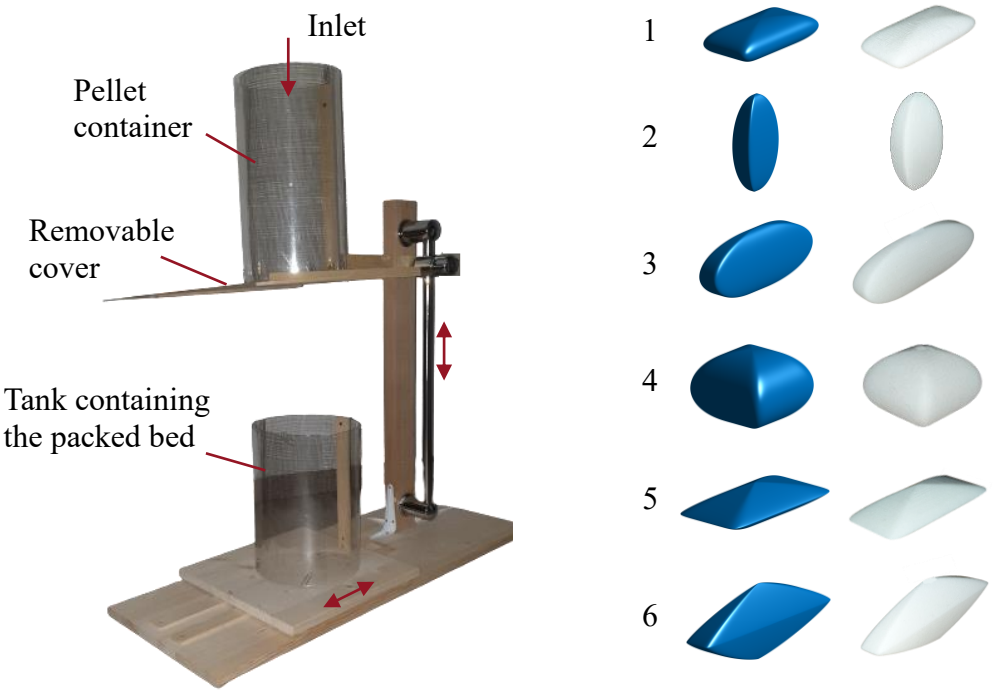

Figure 5-24: Setup for filling experiments (left), and superellipsoid geometries considered for validation in CAD format and as 3D-printed polyamide pellets (right) (both adapted from [89])

The experimental and DEM results are presented in Figure 5-25. As shown there, the measured and simulated packing densities are qualitatively in good agreement. The average deviation between the filling experiments and the simulations was 4.8 %, indicating that the employed DEM was successfully validated.

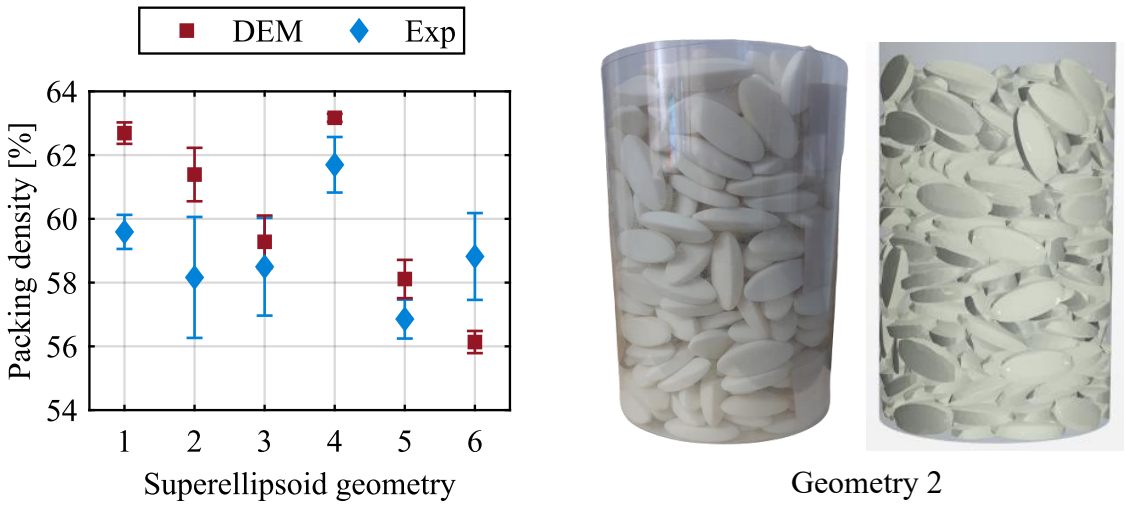

Figure 5-25: Experimental and DEM simulation results for the superellipsoid geometries shown in Table 5-9 (left) and packed beds created by experiment and DEM (right) (both adapted from [89])

The validated DEM approach could now be applied in a parameter study to investigate how the geometrical parameters influence the packing densities of various superellipsoid shapes. In this study, the aspect ratios β and γ were varied in seven steps from 0.4 to 8.0., while the shape factor n was varied in two steps from 1.0 to 1.667. The second shape

factor e was set to a constant value of 0.2. This selection of values was based on a preliminary analysis of the superellipsoid shapes, which indicated that values of e and n near 0 or 2 result in bulky, cubic geometries with large flat surfaces (as seen in Figure 5-23, right). Such shapes hinder the fluid flow in a packed bed. Moreover, when the shape parameters become larger than 2, the resulting superellipsoids become star-shaped, which is undesirable for PCM capsules due to mechanical instability and manufacturing concerns.

The decision to keep one of the shape factors constant was based on studies by Delaney & Cleary [105] and Zhao et al. [106], who investigated packed beds consisting of superellipsoid bodies. While they found that lower values of the shape factors lead to increased packing densities, which is beneficial for the energy density of a PBLHS, the resulting geometries are cubic, with poor heat transfer characteristics. In order to avoid cuboid geometries but still enable relatively high packing densities, one of the shape factors was therefore kept as low as possible.

The values used for the individual geometrical properties are given in Table 5-10. While all possible parameter combinations would result in a total amount 192 superellipsoids, some geometries were discarded due to obvious shortcomings regarding their suitability as PCM capsules (e.g., too flat or too thin). The volume of all superellipsoids considered was the same as in the validation study.

Table 5-10: Aspect ratios and shape factors considered in the parameter study

Property	Values							
Aspect ratio β_S	0.4	0.7	1.0	2.0	3.0	4.0	6.0	8.0
Aspect ratio γ_S	0.4	0.7	1.0	2.0	3.0	4.0	6.0	8.0
Shape factor e	0.2							
Shape factor n	1.0	1.25	1.667					

In total, 116 different superellipsoids (46 for n = 1, 39 for n = 1.25 and 31 for n = 1.667) were considered and the respective packing density resulting from DEM filling simulations performed with each of these geometries was investigated. The results of this investigation are illustrated in Figure 5-26, which shows color plots of the packing densities for the different parameter combinations. It can be seen that the highest packing densities were achieved for aspect ratios between 2 and 0.4, corresponding to bulkier geometries. Furthermore, when β_S and γ_S differ too much from each other, the packing density is quite low, which is the case for, e.g., β_S = 8 and γ_S = 1. Compared to the aspect ratios, the varied shape factor does not appear to have a pronounced effect on the packing density, as the three charts representing the three different values for n show similar trends.

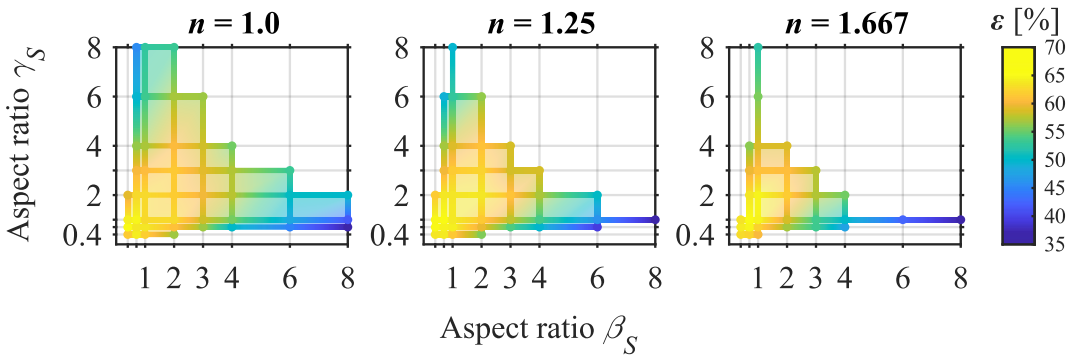

Figure 5-26: Influence of superellipsoid aspect ratios β_S and γ_S and shape factor n on the packing density ε

Regarding the SVR of the superellipsoids considered, the dimensions of each geometry were scaled back up in order to match the original volume corresponding to a 1 kg PCM capsule. This adjustment ensured that the resulting SVR values more accurately reflect those encountered for real PCM capsules that would be used in PBLHS. Figure 5-27 shows the results for the same parameter combinations as above. It can be seen that the color plots appear to be inversed compared to Figure 5-26 – larger aspect ratios create flatter and thinner geometries which, in turn, have larger SVR. Again, the influence of the shape factor does not appear to have a great effect.

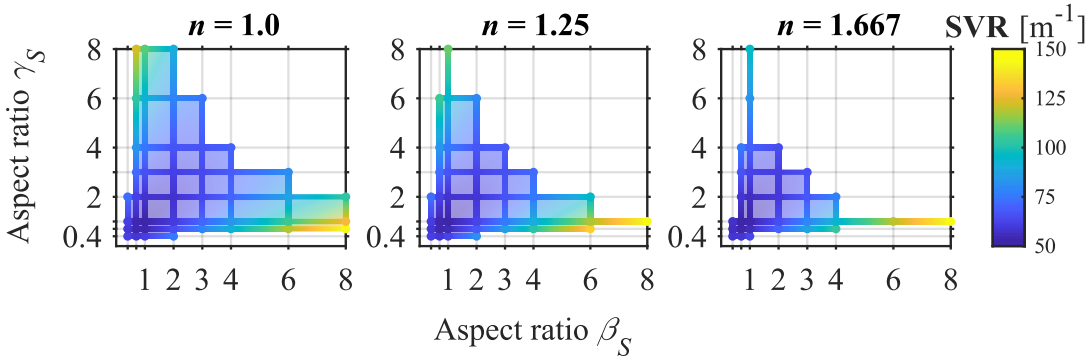

Figure 5-27: Influence of superellipsoid aspect ratios β_S and γ_S and shape factor n on the surface-area-to-volume ratio SVR

Altogether, the highest packing density achieved was 65.22 % resulting from a parameter combination of β_S = 1, γ_S = 0.7, e = 0.2 and n = 1.667. The corresponding SVR was determined as 53.73 m^{-1}, being significantly lower compared to the geometry with the highest SVR of 144.0 m^{-1}, which resulted from the parameter combination β_S = 1, γ_S = 8, e = 0.2 and n = 1.667. However, this geometry achieved a packing density of only 37.23 %, which is quite low and corresponds to roughly half the density of a packed bed consisting of randomly packed spheres, which is approximately 64 % [122]. Both geometries are displayed in Figure 5-28. The superellipsoid achieving the highest packing density is a bulky rhomboid, while the one achieving the highest SVR is a flat rhomboid.

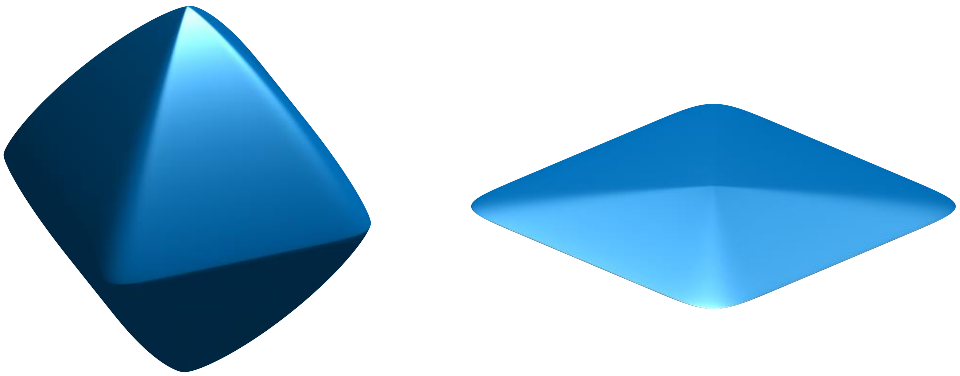

Figure 5-28: The superellipsoid geometries achieving the highest packing density with β_S = 1, γ_S = 0.7, e = 0.2 and n = 1.667 (left) and the highest SVR with β_S = 1, γ_S = 8, e = 0.2 and n = 1.667 (right)

Even though the superellipsoid shown in Figure 5-28, left, achieved the highest ε and the one shown in Figure 5-28, right, achieved the highest SVR encountered in this study, their performance in a PBLHS might not be efficient. The parameter study actually revealed that several geometries achieve packing densities higher than 60 %, which is already a significant improvement over the PCM capsule designs by Axiotherm shown in Figure 5-7, with densities of 53 % and 45 % (see Table 5-3). Consequently, geometries with the highest SVR for packing densities of at least 58 %, 60 %, 62 % and 64 % were further investigated using the PBLHS model presented in section 5.4. Additionally, the two geometries that achieved the highest value for each individual criterion (shown in Figure 5-28), as well as a spherical shape as reference, were considered. All superellipsoids investigated are shown in Table 5-11.

Table 5-11: Geometries considered for PBLHS simulations and their corresponding superellipsoid parameters

Denomination	β_S	γ_S	e	n	A [m²]	SVR [m^{-1}]	ε [%]	Shape
PD58	4	0.7	0.2	1.25	0.0721	75.01	58.22	
PD60	2	0.4	0.2	1.25	0.0644	66.97	61.75	
PD62	0.4	0.4	0.2	1.667	0.0574	59.70	62.84	
PD64	1	0.4	0.2	1	0.0554	57.61	64.32	
PDMax	1	0.7	0.2	1.667	0.0517	53.73	65.22	
SVRMax	1	8	0.2	1.667	0.1385	144.00	37.23	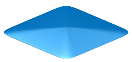
SPH	1	1	0.2	1	0.0471	48.97	64.00	

5.6.3 Performance of selected geometries

To evaluate the performance of the new superellipsoid geometries, the thermal model introduced in section 5.4 was applied to a cylindrical storage tank similar to that described in section 5.3 and filled with packed beds consisting of the PCM capsules shown in Table 5-11. The initialization of the model had to be slightly adapted, since the total number of capsules forming the packed bed was now unknown. Instead, the packing densities that were determined through the DEM simulations were used to calculate the number of capsules:

$$N_C = \varepsilon \frac{V_{PB}}{V_C} \tag{5.33}$$

Here, εV_{PB} represents the total volume that is occupied by the capsules, which have an individual volume of V_C.

The operational parameters chosen for the performance analysis were a flow rate of 600 kg/h and a ΔT of 20 K, as this parameter combination showed a good accuracy during validation. The simulated time was 18 hours, and both charging and discharging simulations were performed. The materials, tank geometry, discretization and other parameters were similar to those in the validation study conducted with the cylindrical storage setup.

The charging simulation results for the seven investigated capsule geometries are shown in Figure 5-29. It can be seen that the capsule geometry with the highest SVR finishes the charging process the fastest, as expected. Then follow the other geometries according to their respective SVR. Not all geometries were able to complete melting in the simulated time but the trajectory of the temperature curves indicates the longest charging duration for the spherical capsule. The thermal power output generally follows the temperature curves. With temperature differences getting smaller, the power output decreases. Since the heat transfer area for the geometries with a high SVR is large, the power output is the highest during the phase change, although only for a short period of time. This is especially the case for the SVRMax variant.

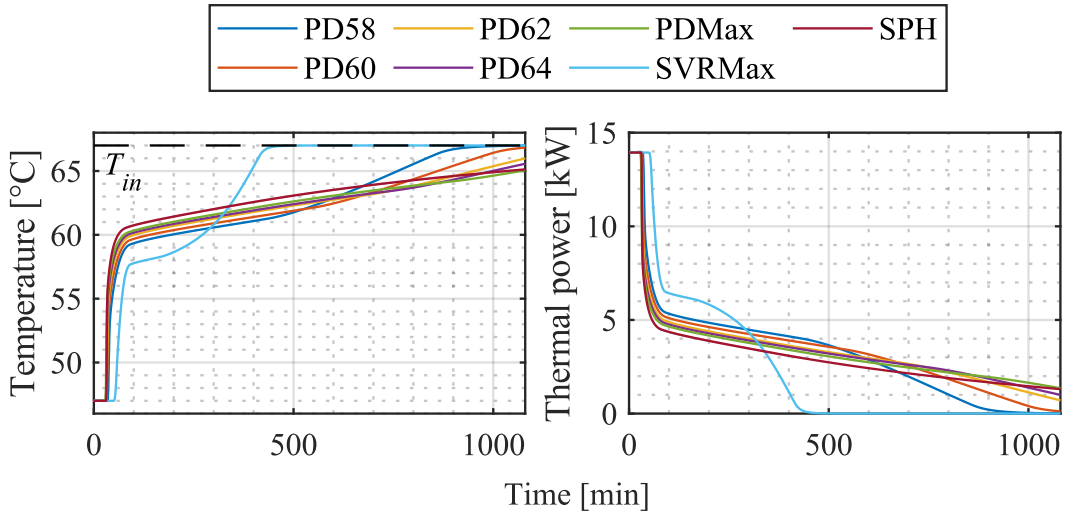

Figure 5-29: Charging simulation results for six different superellipsoid and one spherical PCM capsules: outlet temperature (left) and thermal power (right)

Similar observations can be made when the discharging process shown in Figure 5-30 is considered. The superellipsoids with a high SVR finish earlier than those with high packing densities. Also, the power curves during charging and discharging appear very similar, which was to be expected as effects specific to melting or solidification (here mainly subcooling) are not considered by the model.

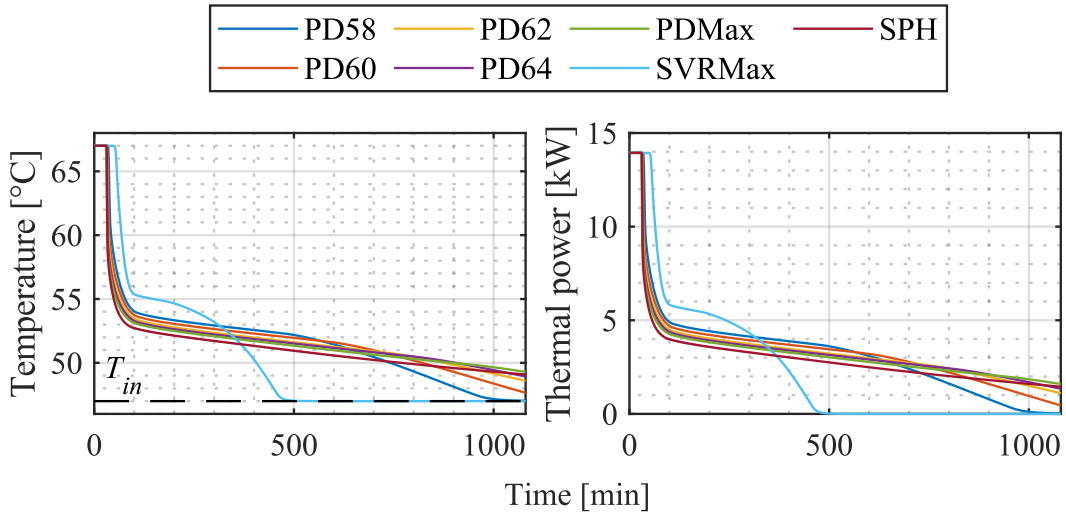

Figure 5-30: Discharging simulation results for six different superellipsoid and one spherical PCM capsules: outlet temperature (left) and thermal power (right)

Additionally, the average liquid fraction across the packed bed was evaluated, since it indicates the charging state of the PBLHS. Figure 5-31 shows the simulated courses of the liquid fraction for the seven capsule variants. The same trends as those observed in the previous two figures can be identified, i.e., the higher the SVR the faster the phase change progresses. It becomes apparent that the spherical capsule requires much more time for the phase change compared to the other geometries. While most other capsule designs finish the phase change after the simulated time of 18 hours, only about half of the total PCM volume in the spherical capsules changed its state. This is due to the low SVR of spheres and the reason why PCM capsules based on a spherical design are rather unsuitable for PBLHS.

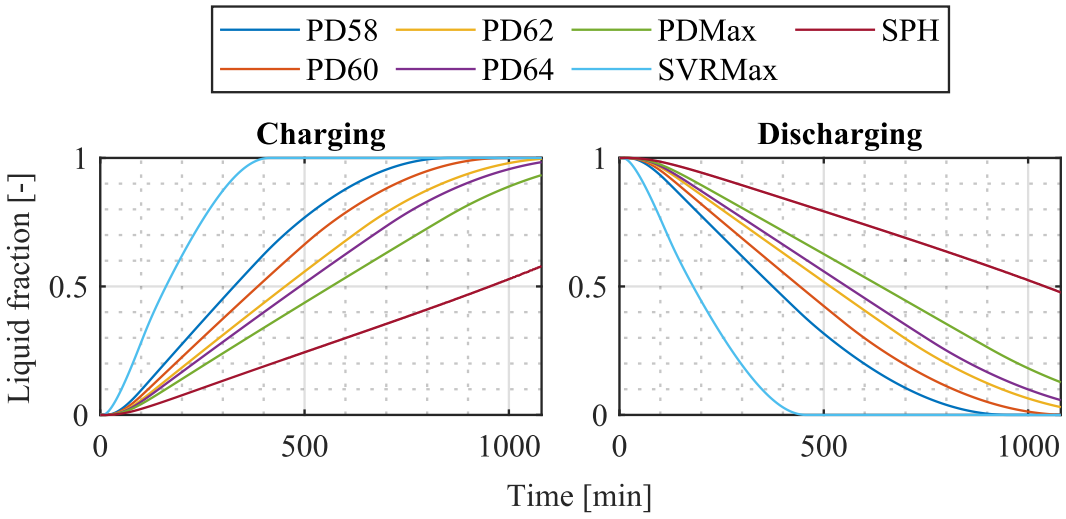

Figure 5-31: Simulated liquid fraction curves for charging and discharging with six different superellipsoid and one spherical PCM capsule geometries

The performance limitations of the spherical capsules become even more obvious when the thermal power is integrated over time, yielding the amount of thermal energy released or stored during charging or discharging. Figure 5-32 shows the thermal energy

stored/released by the PBLHS containing the different capsules during a charging/discharging period of 4, 8, 12 and 18 hours. The spherical design transfers the least energy during those periods, and especially the utilization of the PCM is significantly lower compared to the other designs. Even the capsule variant that achieves the highest packing density with 65.2 % releases/absorbs energy faster than the spherical design with a packing density of just 64 %. Therefore, a major finding of this sensitivity study is that it is possible to design PCM capsules with similar packing density, but significantly better heat transfer capabilities compared to spheres, which are still the state-of-the-art design of PCM capsules for PBLHS.

On the other hand, the capsule variant with maximum SVR performs well during the first four hours and is able to release its stored energy very quickly, which corresponds to the high thermal power output shown in Figure 5-29 and Figure 5-30. Therefore, this design seems suitable for applications where fast charging/discharging rates are required such as backup cooling or heating systems.

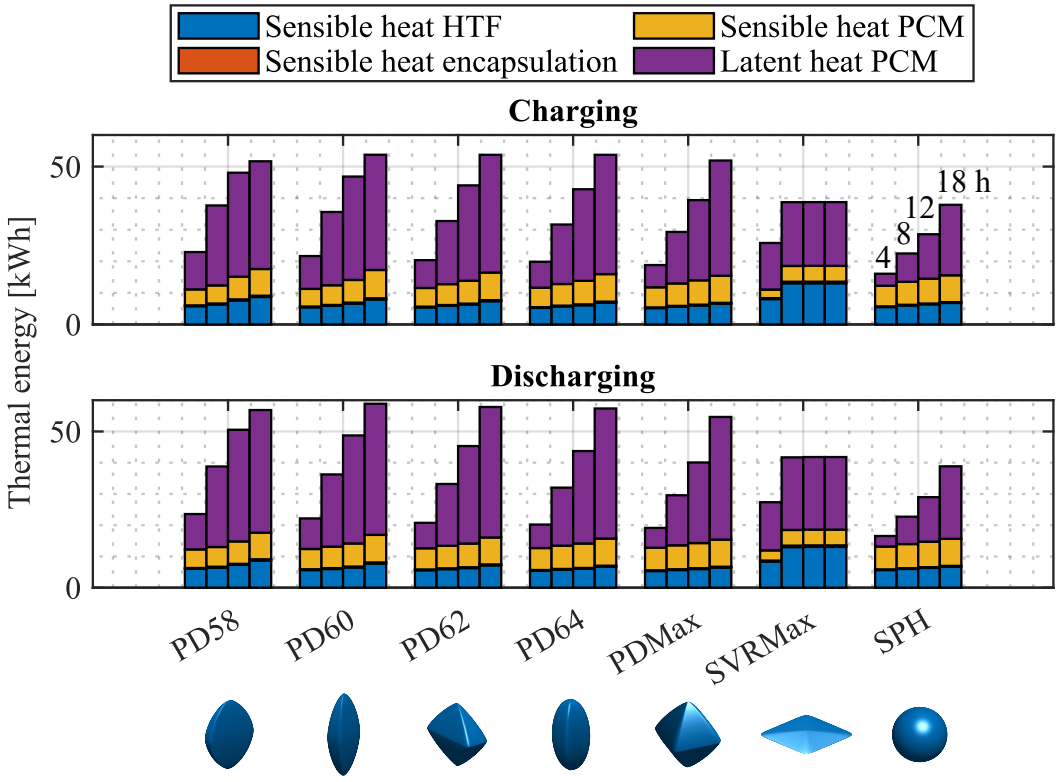

Figure 5-32: Simulated thermal energy absorbed and released during charging and discharging for the seven considered PCM capsule designs after 4 h, 8 h, 12 h and 18 h (indicated by the first, second, third and fourth bar in each bar chart group)

The other capsule geometries (indicated by PD) show rather similar results. It can be seen that the PD58 capsule performs best for durations of up to twelve hours, while over a period of 18 hours, the PD60 variant is able to store/release the most energy. Ultimately, the PDMax geometry contains the highest energy when a complete charging/discharging process is considered.

Generally, the optimal capsule design depends mainly on the application and the operational boundary conditions. If a fast charging and discharging rate, i.e., high thermal

power, is required, the SVRMax design appears to be the most suitable solution. If a high energy density is required, the PDMax design seems to be more appropriate. However, in most cases, both high packing density and high thermal power are necessary. Domestic applications, e.g., a solar thermal collector system combined with a PBLHS, require a compact storage tank that provides a storage capacity high enough to supply a household. This means that the volume-specific energy density has to be sufficiently high, which can be achieved through a dense packing of PCM capsules. At the same time, the charging period is limited to eight to twelve hours due to the day-and-night cycle, which means that sufficient thermal power is required to fully charge the storage during the day. Of course, the operational conditions are not stagnant in most cases, and, to a certain extent, the flow rate and inlet temperature may be used to control the charging process. But if PCM capsules are used that were optimized for this specific application, the utilization of the PCM can be maximized and both the investment and operational cost for the heating system can be reduced.

In case the cylindrical PBLHS considered in the parameter study is used for the mentioned solar thermal collector application, the storage capacity of the system is one of the main technical criteria of the storage and a crucial design parameter for the whole system. Theoretically, it would not be incorrect to specify the total nominal storage capacity, i.e., the energy stored or released throughout a complete charging cycle. This nominal storage capacity would actually be quite high using spherical capsules. However, as Figure 5-31 shows, the storage would only charge to about 30 % during daytime. Therefore, the nominal capacity is not a suitable performance indicator and should always be specified along with the required charging duration. The better capsule alternative for the solar thermal collector would be variant PD58, as it utilizes over 90 % of the PCM during a duration of 12 hours. The stored/released energy for this design is largest compared to all other variants for charging/discharging durations between 8 and 12 hours.

To conclude, the case study revealed that it is possible to create new PCM capsule designs based on superellipsoids that exhibit a similar packing density as spheres yet generate a significantly higher thermal power. As spherical PCM capsules are still very common, this result indicates a large potential for further optimization studies, which could have different goals: a large SVR for high thermal power, a high packing density for a large volume specific storage capacity or a balance of both to achieve a maximum storage capacity for a specific charging/discharging period. Especially in the last case, the optimal design depends on the operational and boundary conditions of the storage system such as the available inlet temperature, mass flow rate, storage volume and charging period. The developed PBLHS model provides a tool to study such different scenarios.

5.7 Summary and conclusion

In this case study, a thermal model of PBLHS was developed, validated against experimental data and subsequently used to evaluate new PCM capsule geometries that improve the performance of such storage systems. The model is based on the concentric dispersion approach, which requires one governing equation for the HTF and one for the PCM

capsules. The solution method is based on the implicit finite difference algorithm presented in Chapter 3. The data used for validation was the temperature response from two different experimental storage setups, installed and operated by the Department of Energy - Building – Environment at Münster University of Applied Sciences. The first setup consisted of a cuboid storage tank filled with PCM capsules arranged in a structured packed bed, while the second setup was based on a cylindrical tank filled with randomly packed capsules. The validation showed that the model is capable of predicting the thermal response of these systems with a maximum mean deviation of 8.3 % or less. The model appeared to work better for higher flow rates and larger differences between inlet and phase change temperature.

A parameter study was carried out, in which different superellipsoid capsule geometries were evaluated regarding their packing density and SVR. Superellipsoids were used because they offer great flexibility and versatility in geometry creation, while requiring only five input parameters. In total, 116 superellipsoids with the same volume were considered in this case study. In order to determine their packing density, DEM-based filling simulations were performed with each geometry. The results showed that several superellipsoids are able to achieve higher packing densities than spheres. These geometries also exhibited higher SVR values than spheres, which made them interesting candidates for further investigation. In total, seven different geometries including a sphere as reference were selected for simulations using the developed PBLHS model. The simulations showed that higher packing densities resulted in longer charging and discharging durations, while for higher SVR values those durations were shorter. Furthermore, the sphere proved inferior to all considered superellipsoid geometries. The variant that was best suited for the scenario considered in the parameter study had a packing density of 58.2 % and an SVR of 75 m^{-1}.

The main objectives of the case study that were outlined in section 5.2 were successfully achieved. The model accuracy is above 90 % and several new PCM capsule geometries were identified that outperform the conventional spherical design in the simulation scenarios considered. Given that the optimal capsule design depends on the particular PBLHS system, the model can be further utilized to test alternative capsule geometries in order to identify the most effective design for a specific application.

Additionally, with only minor modifications, the PBLHS model may also be applied to sensible heat storage systems without PCM, such as sensible liquid and sensible packed bed storages.

Further enhancements in model accuracy could be achieved by considering the subcooling and hysteresis effects of the PCM. Moreover, experimental investigations of additional capsule geometries would help to further explore the range of validity for the spherical shell approximation.

6 Concluding remarks

In this thesis, the application of PCM in combination with two different energy system components is addressed. After establishing the theoretical background relevant to the processes investigated, a model for phase change processes based on the source term method is introduced. The according numerical solution approach relies on an implicit finite difference method by Voller & Swaminathan [30], developed specifically for non-isothermal phase change processes, which are commonly encountered with PCM. The source term method and the associated solution approach were validated against the analytical solution to the Stefan problem and an approximate solution for spherical geometries with good accuracy, which enabled the application of these methods in two case studies. The first of these case studies addressed PCM-enhanced solar PV modules, the second packed bed latent heat storage systems.

6.1 PCM-enhanced solar PV modules

The aim of the first case study was to develop a thermal model of PV-PCM modules that accurately predicts the temperature of the solar cell. The purpose of this model was to assess the impact of different PCM heat sinks attached to the backside of the PV modules on electrical energy output and mechanical degradation. The PCM heat sinks, designed as foils, were intended to reduce cell temperature fluctuations, aiming to increase the PV conversion efficiency and to reduce thermal fatigue.

Experimental data collected by the Electrical Energy Technology department from the Paderborn University PV lab showed that the temperature difference due to the PCM heat sink was small (less than ± 1 K), resulting in an average increase in power output of only 0.5 % compared to a referenc e module without PCM. This experimental data was then used as a validation basis for the developed thermal model of PV-PCM systems.

This model is based on the source term method. The boundary conditions for the top and bottom side of the module account for the heat exchange with the ambient due to radiation and convection. The source term incorporates the phase change dynamic in the PCM and thermal effects resulting from incoming solar irradiance impacting the upper three layers

of the PV module. Different combinations of correlations for the convective and radiative heat transfer coefficients were tested. An optimal combination could be identified, giving an average deviation of less than 2 K (6.25 %) when validated against the experimental data collected from the PV lab on four different days in July 2019 and for three different module configurations (smooth PCM foil, bubble wrap PCM foil and reference without PCM). Such a level of accuracy is notably higher compared to results reported in other studies.

With the validated PV-PCM model, the solar cell temperatures were determined, which were then used to estimate the degradation effect caused by temperature fluctuations through an RFCA and the Coffin-Manson model. The comparison between all three module configurations revealed that the PCM heat sink reduced the received damage by up to 45 %, however, only on days with unsteady weather conditions causing many temperature fluctuations. For very sunny or very cloudy days, this reduction potential was much lower and amounted to only 3 %.

In the last step, the PV-PCM model was used for a parameter study of different PCM heat sink configurations. Three different PCM parameters were varied – the thermal conductivity, the layer thickness and the phase change temperature – and their effect on the electrical energy generation and degradation was studied. The results of the analysis showed that it is possible to design a PCM heat sink that can both increase the power output and reduce degradation due to thermal fatigue if the heat sink thickness and the thermal conductivity of the PCM are sufficiently large. Whether such heat sinks are economically feasible needs to be further investigated in future studies.

6.2 Packed bed latent heat storages

The purpose of the thermal model for PBLHS was to predict the thermal response of different thermal storage systems based on packed beds consisting of PCM capsules. It was mainly developed to simulate the charging and discharging processes of such storage systems. The goal of the case study was to identify new PCM capsule geometries that achieve both a higher packing density and thermal power output than conventional spherical capsules.

The developed model is based on the concentric dispersion approach, which treats the PCM capsules forming the packed bed as individual elements, enabling the temperature gradients within them to be captured. This was necessary to properly describe the melting and solidification processes when charging and discharging the storage. The model uses two equations – one for the HTF and one for the capsules. The governing equation for the HTF considers advective and conductive heat transport and is coupled with the governing equation for the capsules via a source term. This source term models the heat transfer between the packed bed and the HTF using a convective heat transfer coefficient that accounts for both natural and forced convection. The governing equation for the capsules is based on the source term method formulated in spherical coordinates, accounting for thermal conduction and the phase change. It is coupled with the HTF equation by a Robin

boundary condition. Since the PBLHS investigated in this case study contained non-spherical PCM capsules, their geometry was approximated using a spherical shell approach. In this approach, the original capsule surface area is used to determine the outer diameter of a surface-area-equivalent spherical shell. This shell is composed of both encapsulation material and PCM, with a thickness corresponding to the PCM volume of the original capsule. The solution approach for the HTF domain is based on the explicit finite difference method, while the method employed for the capsule domain is based on the implicit finite difference scheme proposed by Voller & Swaminathan [30].

The model was validated against experimental data from two different PBLHS systems. The first system comprised a cuboid storage tank containing a structured packed bed of HeatSels (lentil shape), while the second system comprised a cylindrical storage tank filled with a packed bed of HeatStixx (cylindrical shape). While the model showed a good accuracy with the highest average deviation well below 9 %, it appeared to work better for higher flow rates and larger differences between the phase change and the inlet temperature (i.e., for cases in which the thermal driving forces are larger).

Subsequently, the validated model was used in a geometrical parameter study aiming to identify PCM capsule geometries that achieve both high packing densities and SVR, as these criteria determine the volume-specific energy capacity and thermal power of PBLHS. Conventional PCM capsules are often spherical, creating sufficiently high packing densities but exhibiting a very low SVR. For this reason, the geometries considered for new capsule designs were based on superellipsoids, which can be described by three parametric equations containing five parameters. The shapes that could be created with these equations range from cubes over spheres to rhomboids and concave star-shaped geometries. This versatility allowed for an extensive parameter study. For this parameter study, the set of parameters was further reduced by introducing two aspect ratios and holding one of the five parameters constant. This allowed defining the superellipsoid geometries based on these ratios and their volume, eliminating the need to specify explicit side lengths.

A total number of 116 superellipsoid geometries that had the same volume were generated and their SVR was calculated. These geometries were used in DEM filling simulations in order to determine their achievable packing densities. The results showed that it is possible to create superellipsoids that form densely packed beds while also achieving an SVR greater than that of spheres. In fact, the superellipsoid achieving the highest packing density with 65.22 % had an SVR of 53.73 m^{-1}. Both values are greater than those determined for spheres with the same volume.

In the last step, based on their SVR and packing density, six superellipsoids and a spherical PCM capsule as reference were chosen for further investigation using the PBLHS model. Charging and discharging simulations were performed based on the parameters of the cylindrical storage setup that was previously used for validation. The results showed that all superellipsoid PCM capsules performed better than the spherical reference geometry for the considered charging/discharging duration of 18 hours.

Further improvements in model accuracy could be achieved by accounting for subcooling and hysteresis effects of the PCM. Moreover, experimental investigations of additional capsule geometries would help to further explore the validity range of the spherical shell approximation.

The two case studies presented in this thesis demonstrated that proper modeling and simulation can effectively identify potential improvements in energy system components incorporating PCM. Through two distinct applications, the solution methods employed (the source term method and the implicit finite difference scheme) proved to be versatile, accurate, and adaptable by integrating relevant sub-models and correlations. Also, an extension to two- or three-dimensional problems should be possible allowing for the consideration of geometrically more complex phase change situations.

Appendix

A1: Formulation and discretization of the heat conduction equation in spherical coordinates

The equivalent to Eq. (2.12) in spherical coordinates is:

$$\rho c_p \frac{\partial T}{\partial t} = \frac{1}{r^2}\frac{\partial}{\partial r}\left(kr^2 \frac{\partial T}{\partial r}\right) \tag{A1.1}$$

The conditions that can be encountered at the inner boundary $r = 0$ and the outer boundary $r = R$ of a spherical geometry (e.g., a spherical shell) are as follows:

- Dirichlet boundary conditions:

$$T(r = 0, t > 0) = T_{w,r=0} \tag{A1.2}$$

$$T(r = R, t > 0) = T_{w,r=R} \tag{A1.3}$$

- Neumann boundary conditions:

$$-k \frac{\partial T}{\partial r}\bigg|_{r=0} = \dot{q}_{w,r=0} \tag{A1.4}$$

$$k \frac{\partial T}{\partial r}\bigg|_{r=R} = \dot{q}_{w,r=R} \tag{A1.5}$$

- Robin boundary conditions:

$$-k \frac{\partial T}{\partial r}\bigg|_{r=0} = \dot{q}_{c,r=0} = h\left(T_{amb,r=0} - T(r = 0, t > 0)\right) \tag{A1.6}$$

$$k \frac{\partial T}{\partial r}\bigg|_{r=R} = \dot{q}_{c,r=R} = h\left(T_{amb,r=R} - T(r = R, t > 0)\right) \tag{A1.7}$$

- Radiative boundary conditions:

$$-k\left.\frac{\partial T}{\partial r}\right|_{r=0} = \dot{q}_{r,r=0} = \sigma\varepsilon\left(T_{ab,r=0}^4 - T(r=0,t>0)^4\right) \tag{A1.8}$$

$$k\left.\frac{\partial T}{\partial r}\right|_{r=R} = \dot{q}_{r,r=X} = \sigma\varepsilon\left(T_{ab,r=R}^4 - T(r=R,t>0)^4\right) \tag{A1.9}$$

- Interfacial condition:

$$k_A\left.\frac{\partial T_A}{\partial r}\right|_{r=r_{Int}} = k_B\left.\frac{\partial T_B}{\partial r}\right|_{r=r_{Int}} \tag{A1.10}$$

Using the implicit finite difference method, the discretization of Eq. (A1.1) yields:

$$\begin{aligned}
&\rho c_p \frac{T_n^{j+1} - T_n^j}{\Delta t} \\
&= \frac{(k_{n+1}+k_n)(r_{n+1}+r_n)^2}{8\Delta r^2 r_n^2} T_{n+1}^{j+1} \\
&- \frac{(k_{n+1}+k_n)(r_{n+1}+r_n)^2 + (k_n+k_{n-1})(r_n+r_{n-1})^2}{8\Delta r^2 r_n^2} T_n^{j+1} \\
&+ \frac{(k_n+k_{n-1})(r_n+r_{n-1})^2}{8\Delta r^2 r_n^2} T_{n-1}^{j+1}
\end{aligned} \tag{A1.11}$$

The discretized boundary conditions are (here $N = R/\Delta r$):

- Dirichlet boundary conditions:

$$T_{n=1} = T_{w,n=1} \quad \& \quad k_{n=1} = k_{w,n=1} \tag{A1.12}$$

$$T_{n=N} = T_{w,n=N} \quad \& \quad k_{n=N} = k_{w,n=N} \tag{A1.13}$$

- Neumann boundary conditions:

$$\left.\frac{1}{r^2}\frac{\partial}{\partial r}\left(r^2 k\frac{\partial T}{\partial r}\right)\right|_{n=1} \approx \frac{(k_2+k_1)(r_2+r_1)^2}{4\Delta r^2 r_1^2}(T_2 - T_1) + \frac{2}{\Delta r}\dot{q}_{w,n=1} \tag{A1.14}$$

$$\begin{aligned}
&\left.\frac{1}{r^2}\frac{\partial}{\partial r}\left(r^2 k\frac{\partial T}{\partial r}\right)\right|_{n=N} \\
&\qquad \approx \frac{(k_N+k_{N-1})(r_N+r_{N-1})^2}{4\Delta r^2 r_N^2}(T_N - T_{N-1}) + \frac{2}{\Delta r}\dot{q}_{w,n=N}
\end{aligned} \tag{A1.15}$$

- Robin and radiative boundary conditions:

$$\begin{aligned}
&\left.\frac{1}{r^2}\frac{\partial}{\partial r}\left(r^2 k\frac{\partial T}{\partial r}\right)\right|_{n=1} \\
&\qquad \approx \frac{(k_2+k_1)(r_2+r_1)^2}{4\Delta r^2 r_1^2}(T_2 - T_1) + \frac{2}{\Delta r}h_{n=1}\left(T_{amb,n=1} - T_1\right)
\end{aligned} \tag{A1.16}$$

$$\frac{1}{r^2}\frac{\partial}{\partial r}\left(r^2 k\frac{\partial T}{\partial r}\right)\Big|_{n=N} \approx \frac{(k_N + k_{N-1})(r_N + r_{N-1})^2}{4\Delta r^2 r_N^2}(T_N - T_{N-1}) + \frac{2}{\Delta r}h_{n=N}\left(T_{amb,n=N} - T_N\right) \tag{A1.17}$$

In case of a full sphere, $r_{n=1} = 0$, which causes a singularity at its center. To address this problem, Thibault et al. [123] applied L'Hôpital's rule, assuming symmetry around the center, and derived the following discretization for the boundary condition at $r_{n=1} = 0$:

$$\frac{1}{r^2}\frac{\partial}{\partial r}\left(r^2 k\frac{\partial T}{\partial r}\right)\Big|_{n=1} \approx \frac{(5k_1 + k_2)}{\Delta r^2}(T_2 - T_1) \tag{A1.18}$$

References

[1] European Environment Agency, Share of energy consumption from renewable sources in Europe, 2024. https://www.eea.europa.eu/en/analysis/indicators/share-of-energy-consumption-from, accessed 11 Jul 2024

[2] Y. Yener, S. Kakaç, Heat Conduction, 4th ed., Taylor & Francis, New York, NY, 2008.

[3] F.P. Incropera, D.P. DeWitt, T.L. Bergman, A.S. Lavine, Fundamentals of Heat and Mass Transfer, 6th ed., Wiley, Hoboken, NJ, 2007.

[4] H.D. Baehr, K. Stephan, Wärme- und Stoffübertragung, 10th ed., Springer Berlin Heidelberg, Berlin, Heidelberg, 2016.

[5] P. Stephan, S. Kabelac, M. Kind, D. Mewes, K. Schaber, T. Wetzel (Eds.), VDI-Wärmeatlas, 12th ed., Springer Berlin Heidelberg, Berlin, Heidelberg, 2019.

[6] R. Marek, K. Nitsche, Praxis der Wärmeübertragung - Grundlagen - Anwendungen - Übungsaufgaben, 2nd ed., Fachbuchverl. Leipzig im Carl-Hanser-Verl., München, 2010.

[7] A. Bejan, Convection Heat Transfer, 4th ed., John Wiley & Sons, Inc.in, 2013.

[8] H.K. Versteeg, W. Malalasekera, An Introduction to Computational Fluid Dynamics - The Finite Volume Method, 2nd ed., Pearson Education Ltd, Harlow, England, New York, 2007.

[9] L.J. Fischer, N7 Phasenwechselmaterialien (PCM) für Latent-Wärmespeicher, in: P. Stephan, et al. (Eds.), VDI-Wärmeatlas, 12th ed., Springer Berlin Heidelberg, Berlin, Heidelberg, 2019, 1989–2008. doi:10.1007/978-3-662-52989-8_116

[10] H. Mehling, L.F. Cabeza, Heat and Cold Storage With PCM - An Up to Date Introduction Into Basics and Applications, Springer, Berlin, Heidelberg, 2008.

[11] L.F. Cabeza, Advances in Thermal Energy Storage Systems - Methods and Applications, Elsevier Science & Technology, Cambridge, 2015.

[12] J. Goeke, Thermische Energiespeicher in der Gebäudetechnik, Springer Fachmedien Wiesbaden, Wiesbaden, 2021.

[13] M. Sterner, I. Stadler, Handbook of Energy Storage, Springer Berlin Heidelberg, Berlin, Heidelberg, 2019.

[14] Axiotherm GmbH, Axiotherm PCM. https://www.axiotherm.de/de/produkte/axiotherm-pcm/, accessed 20 Oct 2023

[15] V. Alexiades, A.D. Solomon, Mathematical Modeling of Melting and Freezing Processes, Hemisphere Publishing Corporation, Washington, Philadelphia, London, 1993.

[16] S.C. Gupta, The Classical Stefan Problem - Basic Concepts, Modelling and Analysis with Quasi-Analytical Solutions and Methods, 2nd ed., Elsevier Science, Saint Louis, 2017.

[17] H. Weber (Ed.), Die partiellen Differentialgleichungen der mathematischen Physik - Nach Riemann's Vorlesungen, 5th ed., Friedr. Vieweg & Sohn, Braunschweig, 1912.

[18] H.D. Baehr, K. Stephan, Heat and Mass Transfer, 3rd ed., Springer, Berlin, New York, 2011.

[19] K.W. Morton, D.F. Mayers, Numerical Solution of Partial Differential Equations - An introduction, 2nd ed., Cambridge Univ. Press, Cambridge, 2005.

[20] S.V. Patankar, Numerical Heat Transfer and Fluid Flow, Hemisphere Pub. Corp; New York McGraw-Hill, Washington, 1980.

[21] B. Furenes, B. Lie, Using event location in finite-difference methods for phase-change problems, Numerical Heat Transfer, Part B: Fundamentals 50 (2006) 143–155. doi:10.1080/10407790500459338

[22] J.J. Douglas, J.T.M. Gallie, On the numerical integration of a parabolic differential equation subject to a moving boundary condition, Duke Math. J. 22 (1955). doi:10.1215/S0012-7094-55-02262-6

[23] W.D. Murray, F. Landis, Numerical and machine solutions of transient heat-conduction problems involving melting or freezing: Part I - Method of analysis and sample solutions, Journal of Heat Transfer 81 (1959) 106–112. doi:10.1115/1.4008149

[24] W.L. Heitz, J.W. Westwater, Extension of the numerical method for melting and freezing problems, International Journal of Heat and Mass Transfer 13 (1970) 1371–1375. doi:10.1016/0017-9310(70)90079-7

[25] J.H. Nazzi Ehms, R. de Césaro Oliveski, L.A. Oliveira Rocha, C. Biserni, M. Garai, Fixed grid numerical models for solidification and melting of phase change materials (PCMs), Applied Sciences 9 (2019) 4334. doi:10.3390/app9204334

[26] V.R. Voller, C.R. Swaminathan, B.G. Thomas, Fixed grid techniques for phase change problems: A review, Numerical Meth Engineering 30 (1990) 875–898. doi:10.1002/nme.1620300419

[27] H. Hu, S.A. Argyropoulos, Mathematical modelling of solidification and melting: a review, Modelling Simul. Mater. Sci. Eng. 4 (1996) 371–396. doi:10.1088/0965-0393/4/4/004

[28] K.R. Sultana, S.R. Dehghani, K. Pope, Y.S. Muzychka, Numerical techniques for solving solidification and melting phase change problems, Numerical Heat Transfer, Part B: Fundamentals 73 (2018) 129–145. doi:10.1080/10407790.2017.1422629

[29] C.R. Swaminathan, V.R. Voller, On the enthalpy method, International Journal of Numerical Methods for Heat & Fluid Flow 3 (1993) 233–244. doi:10.1108/eb017528

[30] V.R. Voller, C.R. Swaminathan, General source-based method for solidification phase change, Numerical Heat Transfer, Part B: Fundamentals 19 (1991) 175–189. doi:10.1080/10407799108944962

[31] F. Rösler, Modellierung und Simulation der Phasenwechselvorgänge in makroverkapselten latenten thermischen Speichern, Logos Verlag, Berlin, 2014.

[32] V.R. Voller, C. Prakash, A fixed grid numerical modelling methodology for convection-diffusion mushy region phase-change problems, International Journal of Heat and Mass Transfer 30 (1987) 1709–1719. doi:10.1016/0017-9310(87)90317-6

[33] C.R. Swaminathan, V.R. Voller, Towards a general numerical scheme for solidification systems, International Journal of Heat and Mass Transfer 40 (1997) 2859–2868. doi:10.1016/S0017-9310(96)00329-8

[34] P. Bojek, Solar PV - Energy, 2023. https://www.iea.org/energy-system/renewables/solar-pv, accessed 29 Jul 2024

[35] X.Y. Chin, D. Turkay, J.A. Steele, S. Tabean, S. Eswara, M. Mensi, P. Fiala, C.M. Wolff, A. Paracchino, K. Artuk, D. Jacobs, Q. Guesnay, F. Sahli, G. Andreatta, M. Boccard, Q. Jeangros, C. Ballif, Interface passivation for 31.25%-efficient perovskite/silicon tandem solar cells, Science (New York, N.Y.) 381 (2023) 59–63. doi:10.1126/science.adg0091

[36] S. de Wolf, E. Aydin, Tandems have the power, Science (New York, N.Y.) 381 (2023) 30–31. doi:10.1126/science.adi6278

[37] M. Sharaf, M.S. Yousef, A.S. Huzayyin, Review of cooling techniques used to enhance the efficiency of photovoltaic power systems, Environmental science and pollution research international 29 (2022) 26131–26159. doi:10.1007/s11356-022-18719-9

[38] A. Shah, Solar Cells and Modules, Springer International Publishing, Cham, 2020.

[39] K.-A. Weiß, Photovoltaic Modules, 2nd ed., De Gruyter, Berlin, Boston, 2021.

[40] M.J. Huang, P.C. Eames, B. Norton, Thermal regulation of building-integrated photovoltaics using phase change materials, International Journal of Heat and Mass Transfer 47 (2004) 2715–2733. doi:10.1016/j.ijheatmasstransfer.2003.11.015

[41] E. Japs, G. Sonnenrein, S. Krauter, J. Vrabec, Experimental study of phase change materials for photovoltaic modules: Energy performance and economic yield for the EPEX spot market, Solar Energy 140 (2016) 51–59. doi:10.1016/j.solener.2016.10.048

[42] S. Nižetić, A.M. Papadopoulos, E. Giama, Comprehensive analysis and general economic-environmental evaluation of cooling techniques for photovoltaic panels, Part I: Passive cooling techniques, Energy Conversion and Management 149 (2017) 334–354. doi:10.1016/j.enconman.2017.07.022

[43] H.M. Ali, Recent advancements in PV cooling and efficiency enhancement integrating phase change materials based systems – A comprehensive review, Solar Energy 197 (2020) 163–198. doi:10.1016/j.solener.2019.11.075

[44] J.H. Wohlgemuth, Reliability of PV systems, in: N.G. Dhere (Ed.), Reliability of photovoltaic cells, modules, components, and systems, SPIE, 2008 704802. doi:10.1117/12.795248

[45] D. Weber, M.I.R. Jani, M. Grabo, O. Wallscheid, J. Bocker, T. Klaus, S. Krauter, Lifetime Extension of Photovoltaic Modules by Influencing the Module Temperature Using Phase Change Material, in: 2018 IEEE 7th World Conference on Photovoltaic Energy Conversion (WCPEC) (A Joint Conference of 45th IEEE PVSC, 28th PVSEC & 34th EU PVSEC), IEEE, 2018 784–789. doi:10.1109/PVSC.2018.8548115

[46] E. Skoplaki, J.A. Palyvos, Operating temperature of photovoltaic modules: A survey of pertinent correlations, Renewable Energy 34 (2009) 23–29. doi:10.1016/j.renene.2008.04.009

[47] M. Mattei, G. Notton, C. Cristofari, M. Muselli, P. Poggi, Calculation of the polycrystalline PV module temperature using a simple method of energy balance, Renewable Energy 31 (2006) 553–567. doi:10.1016/j.renene.2005.03.010

[48] M. Jaszczur, J. Teneta, Q. Hassan, E. Majewska, R. Hanus, An experimental and numerical investigation of photovoltaic module temperature under varying environmental conditions, Heat Transfer Engineering 42 (2021) 354–367. doi:10.1080/01457632.2019.1699306

[49] A.D. Jones, C.P. Underwood, A thermal model for photovoltaic systems, Solar Energy 70 (2001) 349–359. doi:10.1016/S0038-092X(00)00149-3

[50] A.K. Abdulrazzaq, B. Plesz, G. Bognár, A Novel Method for Thermal Modelling of Photovoltaic Modules/Cells under Varying Environmental Conditions, Energies 13 (2020) 3318. doi:10.3390/en13133318

[51] G. Notton, C. Cristofari, M. Mattei, P. Poggi, Modelling of a double-glass photovoltaic module using finite differences, Applied Thermal Engineering 25 (2005) 2854–2877. doi:10.1016/j.applthermaleng.2005.02.008

[52] P. Bevilacqua, S. Perrella, R. Bruno, N. Arcuri, An accurate thermal model for the PV electric generation prediction: long-term validation in different climatic conditions, Renewable Energy 163 (2021) 1092–1112. doi:10.1016/j.renene.2020.07.115

[53] V. Lo Brano, G. Ciulla, A. Piacentino, F. Cardona, Finite difference thermal model of a latent heat storage system coupled with a photovoltaic device: Description and experimental validation, Renewable Energy 68 (2014) 181–193. doi:10.1016/j.renene.2014.01.043

[54] M. Arıcı, F. Bilgin, S. Nižetić, A.M. Papadopoulos, Phase change material based cooling of photovoltaic panel: A simplified numerical model for the optimization of the phase change material layer and general economic evaluation, Journal of Cleaner Production 189 (2018) 738–745. doi:10.1016/j.jclepro.2018.04.057

[55] F.A. Díaz, N.O. Moraga, R.C. Cabrales, Computational modeling of a PV-PCM passive cooling system during a day–night cycle at arid and semi-arid climate zones, Energy Conversion and Management 270 (2022) 116202. doi:10.1016/j.enconman.2022.116202

[56] N. Savvakis, T. Tsoutsos, Theoretical design and experimental evaluation of a PV+PCM system in the mediterranean climate, Energy 220 (2021) 119690. doi:10.1016/j.energy.2020.119690

[57] VDE Verband der Elektrotechnik Elektronik Informationstechnik e.V. und VDI Verein Deutscher Ingenieure e.V., Photovoltaische Einrichtungen - Teil 3: Messgrundsätze für terrestrische photovoltaische (PV)-Einrichtungen mit Angaben über die spektrale Strahlungsverteilung, DIN EN IEC 60904-3:2020-01, Berlin, Offenbach, 2020.

[58] G. Sonnenrein, A. Elsner, E. Baumhögger, A. Morbach, K. Fieback, J. Vrabec, Reducing the power consumption of household refrigerators through the integration of latent heat storage elements in wire-and-tube condensers, International Journal of Refrigeration 51 (2015) 154–160. doi:10.1016/j.ijrefrig.2014.12.011

[59] E. Skoplaki, J.A. Palyvos, On the temperature dependence of photovoltaic module electrical performance: A review of efficiency/power correlations, Solar Energy 83 (2009) 614–624. doi:10.1016/j.solener.2008.10.008

[60] D.L. Evans, L.W. Florschuetz, Cost studies on terrestrial photovoltaic power systems with sunlight concentration, Solar Energy 19 (1977) 255–262. doi:10.1016/0038-092X(77)90068-8

[61] J.A. Palyvos, A survey of wind convection coefficient correlations for building envelope energy systems' modeling, Applied Thermal Engineering 28 (2008) 801–808. doi:10.1016/j.applthermaleng.2007.12.005

[62] S. Sharples, P.S. Charlesworth, Full-scale measurements of wind-induced convective heat transfer from a roof-mounted flat plate solar collector, Solar Energy 62 (1998) 69–77. doi:10.1016/S0038-092X(97)00119-9

[63] E. Sartori, Convection coefficient equations for forced air flow over flat surfaces, Solar Energy 80 (2006) 1063–1071. doi:10.1016/j.solener.2005.11.001

[64] E. Kaplani, S. Kaplanis, Thermal modelling and experimental assessment of the dependence of PV module temperature on wind velocity and direction, module orientation and inclination, Solar Energy 107 (2014) 443–460. doi:10.1016/j.solener.2014.05.037

[65] U. Eicker, Solar Technologies for Buildings, Wiley, New York, Chichester, 2003.

[66] S.W. Churchill, A comprehensive correlating equation for laminar, assisting, forced and free convection, AIChE Journal 23 (1977) 10–16. doi:10.1002/aic.690230103

[67] H. Klan, A. Thess, F2 Wärmeübertragung durch freie Konvektion: Außenströmung, in: P. Stephan, et al. (Eds.), VDI-Wärmeatlas, 11th ed., Springer Berlin Heidelberg, Berlin, Heidelberg, 2013, 757–764. doi:10.1007/978-3-642-19981-3_38

[68] T. Fujii, H. Imura, Natural-convection heat transfer from a plate with arbitrary inclination, International Journal of Heat and Mass Transfer 15 (1972) 755–767. doi:10.1016/0017-9310(72)90118-4

[69] S.W. Churchill, H.H. Chu, Correlating equations for laminar and turbulent free convection from a vertical plate, International Journal of Heat and Mass Transfer 18 (1975) 1323–1329. doi:10.1016/0017-9310(75)90243-4

[70] M. Hammami, S. Torretti, F. Grimaccia, G. Grandi, Thermal and performance analysis of a photovoltaic module with an integrated energy storage system, Applied Sciences 7 (2017) 1107. doi:10.3390/app7111107

[71] S. Algarni, D. Nutter, Survey of sky effective temperature models applicable to building envelope radiant heat transfer, 2015. doi:10.13140/RG.2.1.4212.5526

[72] H.P. Garg, Treatise on Solar Energy - Vol. 1: Fundamentals of Solar Energy, John Wiley, Chichester, 1982.

[73] A. Whillier, Design factors influencing solar collectors, in: Low temperature engineering applications of solar energy, 254262

[74] W.C. Swinbank, Long-wave radiation from clear skies, Quart J Royal Meteoro Soc 89 (1963) 339–348. doi:10.1002/qj.49708938105

[75] M.K. Fuentes, A simplified thermal model for Flat-Plate photovoltaic arrays, Albuquerque, NM (USA), 1987. https://www.osti.gov/biblio/6802914

[76] M. Musallam, C.M. Johnson, An efficient implementation of the Rainflow Counting Algorithm for life consumption estimation, IEEE Trans. Rel. 61 (2012) 978–986. doi:10.1109/TR.2012.2221040

[77] L.F. Coffin, A study of the effects of cyclic thermal stresses on a ductile metal, Journal of Fluids Engineering 76 (1954) 931–949. doi:10.1115/1.4015020

[78] H. Cui, Accelerated temperature cycle test and Coffin-Manson model for electronic packaging, in: Annual Reliability and Maintainability Symposium, 2005. Proceedings, IEEE, 2005 556–560. doi:10.1109/RAMS.2005.1408421

[79] N. Bosco, T.J. Silverman, S. Kurtz, Modeling thermal fatigue in CPV cell assemblies, IEEE J. Photovoltaics 1 (2011) 242–247. doi:10.1109/JPHOTOV.2011.2172575

[80] M.A. Miner, Cumulative damage in fatigue, Journal of Applied Mechanics 12 (1945) A159-A164. doi:10.1115/1.4009458

[81] IEA, Renewables 2022, Paris, 2022. https://www.iea.org/reports/renewables-2022

[82] F. Scheffler, Thermische Energiespeicher – Trends, Entwicklungen und Herausforderungen, Chemie Ingenieur Technik 91 (2019) 1219–1228. doi:10.1002/cite.201800156

[83] I. Sarbu, C. Sebarchievici, A comprehensive review of thermal energy storage, Sustainability 10 (2018) 191. doi:10.3390/su10010191

[84] Spirax Sarco Limited, Steam accumulators, 2024. https://www.spirax-sarco.com/learn-about-steam/the-boiler-house/steam-accumulators, accessed 30 Jul 2024

[85] J. Gasia, L. Miró, L.F. Cabeza, Review on system and materials requirements for high temperature thermal energy storage. Part 1: General requirements, Renewable and Sustainable Energy Reviews 75 (2017) 1320–1338. doi:10.1016/j.rser.2016.11.119

[86] G. Santori, A. Frazzica, A. Freni, M. Galieni, L. Bonaccorsi, F. Polonara, G. Restuccia, Optimization and testing on an adsorption dishwasher, Energy 50 (2013) 170–176. doi:10.1016/j.energy.2012.11.031

[87] E. Lävemann, Mobile Sorptionsspeicher zur industriellen Abwärmenutzung - Grundlagen und Demonstrationsanlage

[88] R. Weber, V. Dorer, Long-term heat storage with NaOH, Vacuum 82 (2008) 708–716. doi:10.1016/j.vacuum.2007.10.018

[89] L. Kuckuck, Entwicklung eines Modells zur Erzeugung stochastischer Schüttungen superellipsoider Körper, Unpublished student project report (supervisor: M. Grabo), Paderborn University, Paderborn, 2020.

[90] A. de Gracia, L.F. Cabeza, Numerical simulation of a PCM packed bed system: A review, Renewable and Sustainable Energy Reviews 69 (2017) 1055–1063. doi:10.1016/j.rser.2016.09.092

[91] K. Ismail, R. Stuginsky Jr, A parametric study on possible fixed bed models for pcm and sensible heat storage, Applied Thermal Engineering 19 (1999) 757–788. doi:10.1016/S1359-4311(98)00081-7

[92] X. He, J. Qiu, W. Wang, Y. Hou, M. Ayyub, Y. Shuai, A review on numerical simulation, optimization design and applications of packed-bed latent thermal energy storage system with spherical capsules, Journal of Energy Storage 51 (2022) 104555. doi:10.1016/j.est.2022.104555

[93] T. Schumann, Heat transfer: A liquid flowing through a porous prism, Journal of the Franklin Institute 208 (1929) 405–416. doi:10.1016/S0016-0032(29)91186-8

[94] A. Felix Regin, S.C. Solanki, J.S. Saini, An analysis of a packed bed latent heat thermal energy storage system using PCM capsules: Numerical investigation, Renewable Energy 34 (2009) 1765–1773. doi:10.1016/j.renene.2008.12.012

[95] D.A. Nield, A. Bejan, Convection in Porous Media, 5th ed., Springer International Publishing, Cham, 2017.

[96] S. Bellan, J. Gonzalez-Aguilar, A.R. Archibold, M. Romero, M.M. Rahman, D.Y. Goswami, E.K. Stefanakos, Transient numerical analysis of storage tanks based on encapsulated PCMs for heat storage in concentrating solar power plants, Energy Procedia 57 (2014) 672–681. doi:10.1016/j.egypro.2014.10.222

[97] S. Bellan, J. Gonzalez-Aguilar, M. Romero, M.M. Rahman, D.Y. Goswami, E.K. Stefanakos, D. Couling, Numerical analysis of charging and discharging performance of a thermal energy storage system with encapsulated phase change material, Applied Thermal Engineering 71 (2014) 481–500. doi:10.1016/j.applthermaleng.2014.07.009

[98] S. Bellan, T.E. Alam, J. González-Aguilar, M. Romero, M.M. Rahman, D. Goswami, E.K. Stefanakos, Numerical and experimental studies on heat transfer characteristics of thermal energy storage system packed with molten salt PCM capsules, Applied Thermal Engineering 90 (2015) 970–979. doi:10.1016/j.applthermaleng.2015.07.056

[99] M. Wu, C. Xu, Y.-L. He, Dynamic thermal performance analysis of a molten-salt packed-bed thermal energy storage system using PCM capsules, Applied Energy 121 (2014) 184–195. doi:10.1016/j.apenergy.2014.01.085

[100] K. Ismail, J.R. Henríquez, Numerical and experimental study of spherical capsules packed bed latent heat storage system, Applied Thermal Engineering 22 (2002) 1705–1716. doi:10.1016/S1359-4311(02)00080-7

[101] W. Foudhil, B. Dhifaoui, S.B. Jabrallah, Y. Dutil, D.R. Rousse, Numerical simulation of thermal storage by latent and sensible heat in a porous vertical channel: Performance analysis and comparison, Numerical Heat Transfer, Part A: Applications 62 (2012) 948–972. doi:10.1080/10407782.2012.715982

[102] L. Xia, P. Zhang, R.Z. Wang, Numerical heat transfer analysis of the packed bed latent heat storage system based on an effective packed bed model, Energy 35 (2010) 2022–2032. doi:10.1016/j.energy.2010.01.018

[103] S. Karthikeyan, R. Velraj, Numerical investigation of packed bed storage unit filled with PCM encapsulated spherical containers – A comparison between various mathematical models, International Journal of Thermal Sciences 60 (2012) 153–160. doi:10.1016/j.ijthermalsci.2012.05.010

[104] P. Stephan, S. Kabelac, M. Kind, H. Martin, D. Mewes, K. Schaber (Eds.), VDI-Wärmeatlas, 11th ed., Springer Berlin Heidelberg, Berlin, Heidelberg, 2013.

[105] G.W. Delaney, P.W. Cleary, The packing properties of superellipsoids, Europhys. Lett. 89 (2010) 34002. doi:10.1209/0295-5075/89/34002

[106] S. Zhao, N. Zhang, X. Zhou, L. Zhang, Particle shape effects on fabric of granular random packing, Powder Technology 310 (2017) 175–186. doi:10.1016/j.powtec.2016.12.094

[107] V. Linnemann, Konzeptionierung und Bau eines Prüfstandes zur Leistungsmessung von thermischen Energiespeichern auf der Basis von PCM, Unpublished Bachelor thesis (supervisor: B. Boiting), Münster University of Applied Sciences, Münster, 2016.

[108] P. Richter, Inbetriebnahme des Prüfstandes zur messtechnischen Untersuchung eines PCM-Energiespeichers, Unpublished student project report (supervisor: B. Boiting), Münster University of Applied Sciences, Münster, 2018.

[109] P. Richter, Optimierung des Eigenverbrauchs von Photovoltaikanlagen mittels thermischer Latentspeichersysteme, mittels messtechnischer Untersuchung und Simulation, Unpublished Master thesis (supervisor: B. Boiting), Münster University of Applied Sciences, Münster, 2020.

[110] P. Richter, Messtechnische Untersuchung eins PCM-Energiespeichers, Unpublished Bachelor thesis (supervisor: B. Boiting), Münster University of Applied Sciences, Münster, 2018.

[111] Axiotherm GmbH, heatStixx - Die innovative Lösung zur Erhöhung der Speicherkapazität!, Eisenberg, 2018.

[112] M. Grabo, E. Acar, E.Y. Kenig, Modeling and improvement of a packed bed latent heat storage filled with non-spherical encapsulated PCM-Elements, Renewable Energy 173 (2021) 1087–1097. doi:10.1016/j.renene.2021.04.022

[113] V. Gnielinski, Berechnung des Wärme- und Stoffaustauschs in durchströmten ruhenden Schüttungen, Verfahrenstechnik 16 (1982) 36–39.

[114] V. Gnielinski, G9 Wärmeübertragung bei erzwungener Konvektion: Durchströmte Haufwerke, in: P. Stephan, et al. (Eds.), VDI-Wärmeatlas, 12th ed., Springer Berlin Heidelberg, Berlin, Heidelberg, 2019, 889–891. doi:10.1007/978-3-662-52989-8_50

[115] W. Kast, O. Krischer, H. Reinicke, K. Wintermantel, Konvektive Wärme- und Stoffübertragung, Springer Berlin Heidelberg, Berlin, Heidelberg, 1974.

[116] A. Thess, R. Kaiser, F3 Wärmeübertragung bei freier Konvektion: Innenströmungen, in: P. Stephan, et al. (Eds.), VDI-Wärmeatlas, 12th ed., Springer Berlin Heidelberg, Berlin, Heidelberg, 2019, 773–783. doi:10.1007/978-3-662-52989-8_39

[117] M. Gardner, Mathematischer Karneval, 7th ed., Ullstein, Frankfurt a. M., 1979.

[118] A.H. Barr, Superquadrics and angle-preserving transformations, IEEE Comput. Grap. Appl. 1 (1981) 11–23. doi:10.1109/MCG.1981.1673799

[119] G.E. Andrews, R. Askey, R. Roy, Special Functions, Cambridge University Press, 2013.

[120] M. Abramowitz, I.A. Stegun, Handbook of mathematical functions - With formulas, graphs, and mathematical tables, 9th ed., Dover Publications, New York, NY, 2013.

[121] Y.T. Feng, K. Han, D. Owen, Energy-conserving contact interaction models for arbitrarily shaped discrete elements, Computer Methods in Applied Mechanics and Engineering 205-208 (2012) 169–177. doi:10.1016/j.cma.2011.02.010

[122] S. Torquato, T.M. Truskett, P.G. Debenedetti, Is random close packing of spheres well defined?, Physical review letters 84 (2000) 2064–2067. doi:10.1103/PhysRevLett.84.2064

[123] J. Thibault, S. Bergeron, H.W. Bonin, On finite-difference solutions of the heat equation in spherical coordinates, Numerical Heat Transfer 12 (1987) 457–474. doi:10.1080/10407788708913597

Erklärung zur Zitation von Inhalten aus studentischen Arbeiten

In Ergänzung zu meinem Antrag auf Zulassung zur Promotion in der Fakultät für Maschinenbau der Universität Paderborn erkläre ich gemäß §11 der Promotionsordnung und unter Beachtung der Regelung zur Zitation studentischer Arbeiten:

Die von mir vorgelegte Dissertation habe ich selbstständig verfasst, und ich habe keine anderen als die dort angegebenen Quellen und Hilfsmittel benutzt. Es sind Inhalte / ~~keine Inhalte~~ studentischen Ursprungs (studentische Arbeiten) in dieser Dissertation enthalten.

Ich habe die verwendeten Arbeiten entsprechend der Regelung „Zitation aus studentischen Arbeiten in Dissertationen“ zitiert.

Paderborn, d. 30.10.2024

Matti Grabo